Aircraft Fuselage Vibration Excitation
by Turbulent Boundary Layer Flow in Cruise

Von der Fakultät für Maschinenbau

der Technischen Universität Carolo-Wilhelmina zu Braunschweig

zur Erlangung der Würde

eines Doktor-Ingenieurs (Dr.-Ing.)

genehmigte Dissertation

von:	Dipl.-Ing. Alexander Klabes
aus:	Münster (Westf.)

eingereicht am:	15.03.2017
mündliche Prüfung am:	28.09.2017
Vorsitz:	Prof. Dr.-Ing. R. Radespiel
Gutachter:	Prof. Dr.-Ing. J. W. Delfs
	Prof. Dr.-Ing. X. Gloerfelt

2017

Vorwort

Diese Dissertation ist innerhalb einer Industriepatenschaft zwischen dem Deutschen Zentrum für Luft- und Raumfahrt e.V. und der Airbus Operations GmbH entstanden. Auf Seiten des DLR war die Abteilung Technische Akustik des Instituts für Aerodynamik und Strömungstechnik in Braunschweig (AS-TEA) und auf Seiten von Airbus war die Abteilung für Kabinenakustik in Hamburg (EPA5) beteiligt.
Zuallererst möchte ich mich herzlich bei meiner Frau Sandra für ihre Unterstützung und ihre Motivation während meiner gesamten Promotion bedanken.
Meinem Doktorvater Professor Jan Delfs danke ich für die Betreuung dieser Arbeit und für seine fachliche Unterstützung.
Dr. Michaela Herr stand mir stets bei meinen Fragen zur Seite, hat mich beraten und unterstützt, hierfür danke ich ihr sehr.
Für eine tolle Zeit in Braunschweig möchte ich mich auch bei all meinen Kollegen und Freunden vom DLR in Braunschweig bedanken sowie bei Johannes Waltermann, der mir immer mit Rat und Tat zur Seite stand.
Mohamed Bouhaj und Dr. Ralf Kemme danke ich für die Idee und die Themenstellung für die Dissertation. Beide haben mich stets unterstützt und sich neben Henning Scheel für die finanzielle Absicherung der Promotion eingesetzt.
Mein fachlicher Betreuer Dr. Sören Callsen stand mir nicht nur bei technischen und inhaltlichen Fragen jederzeit zur Verfügung, er ist mir, wie auch unser Bürokollege Carlos de Matos, zu einem guten Freund geworden. Danke auch für die unvergesslichen Kaffeepausen und Kantinenbesuchen mit allen weiteren Kollegen und Freunden von Airbus und Airbus Group Innovations (AGI).
Nicht zuletzt danke ich all meinen Kollegen und Freunden, die mich über die Jahre fachlich und nicht-fachlich unterstützt haben, sich meine Sorgen angehört haben und nie aufgehört haben, an den Erfolg der Arbeit zu glauben.

Hamburg, 03.10.2017 Alexander Klabes

Abstract

Today, the turbulent boundary layer (TBL) is the major source for aircraft cabin interiour acoustics. Due to the decreasing contribution of aircraft engines to the cabin noise levels, the importance of TBL as source is increasing. Especially aircraft manufacturers are interested in building the quietest and most comfortable aircrafts in the market. To do so, it is of interest to investigate the TBL as a noise source and being able to precisely estimate its contribution to the interiour noise everywhere on the aircraft.
This thesis deals with the prediction of aircraft fuselage vibration excitation by the TBL at typical cruise flight conditions. To characterise the excitation by the TBL, information about the frequency dependent pressure fluctuations, thus the strength of turbulence as a measure for the pressure amplitudes is necessary. Furthermore, the development of turbulence in space and time is important. This information is covered by the auto-spectrum as well as the wavenumber-frequency spectrum.
In a first step, measured auto-spectra during flight tests are postprocessed and analysed as a validation data base. Furthermore, models for auto-spectra and wavenumber-frequency spectra are reviewed from literature and finally, an enhanced auto-spectrum model is developed. To do so, computational fluid dynamics (CFD) is used to solve the Reynolds averaged Navier Stokes (RANS) equations numerically with DLR's TAU code and the respective aerodynamic data is used as input for the development of the new auto-spectrum model. Parallelly to these semi-empirical modelling activities, a full numerical approach is followed to predict the TBL in terms of auto-spectra and wavenumber-frequency spectra. For this purpose, the Fast Random Particle-Mesh Method (FRPM) from DLR is applied to distinct parts of an Airbus A320 at cruise flight conditions. Beside this, the predicted excitation models are numerically applied to aircraft fuselage sections by using the Statistical Energy Analysis (SEA) and the structural response of several subsystems is analysed. Finally, the numerically estimated structural vibrations are compared with analysed measured vibrations from flight tests on the real aircraft structure.
The new developed auto-spectrum model demonstrates a good reliability in the prediction of auto-spectra on an aircrafts fuselage within its aerodynamic limits. Beside this, predicted and measured structural vibration collapse over a large

frequency range for the tested areas. This new method enables a CFD based prediction of auto-spectra everywhere on a fuselage and therefore the calculation of structural excitation.

Zusammenfassung

Die turbulente Grenzschicht (TBL) ist die Hauptlärmquelle der Kabinenakustik bei heutigen Verkehrsflugzeugen. Durch den verringerten Schalleintrag aus modernen Triebwerken steigt die Relevanz der TBL als Lärmquelle für die Flugzeugkabine. Flugzeughersteller haben das Ziel, das leiseste und komfortabelste Flugzeug auf dem Markt zu bauen. Um dieses Ziel zu erreichen, ist es von großer Bedeutung die TBL als Lärmquelle genau zu verstehen und den Schalleintrag in der gesamten Flugzeugkabine berechnen zu können.
Diese Doktorarbeit beschäftigt sich mit der Vorhersage von Rumpfstrukturanregung bei Verkehrsflugzeugen durch die TBL bei typischen Reiseflugbedingungen. Um die Anregung zu charakterisieren, müssen Informationen über die frequenzabhängigen Druckfluktuationen, also die Stärke der Turbulenz vorliegen. Außerdem sind Informationen über die räumliche und zeitliche Entwicklung der Turbulenz unabdingbar. Diese Informationen werden über das Autospektrum sowie das Wellenzahlfrequenzspektrum abgebildet.
Im ersten Schritt werden Flugtestdaten ausgewertet, die zur Validierung herangezogen werden. Nachfolgend werden Modelle für Autospektren und Wellenzahlfrequenzspektren aus der Literatur verglichen und in einem weiteren Schritt wird ein bestehendes Modell zur Vorhersage von Autospektren weiterentwickelt. Für diese Weiterentwicklung werden numerisch die Zustandsgrößen der Strömung berechnet (CFD), wobei der "Reynolds averaged Navier Stokes" (RANS) Löser TAU des DLR genutzt wird. Die Strömungsgrößen werden als Eingangsgrößen für das neue Autospektren Modell genutzt. Parallel zu den semi-empirischen Modellierungen wird ein voll numerischer Ansatz verfolgt, um die Autospektren und Wellenzahlfrequenzspektren der TBL vorherzusagen. Hierzu wird die "Fast Random Particle-Mesh" Methode (FRPM) des DLR in bestimmten Bereichen eines Airbus A320 bei Reiseflugbedingungen angewendet. In einem weiteren Schritt werden die Anregungsmodelle mit Hilfe der Statistischen Energieanalyse (SEA) numerisch an eine Flugzeugstruktur gerechnet und die daraus resultierenden Strukturvibrationen ausgewählter Subsysteme ausgewertet. Abschließend wird die numerische Vorhersage mit den gemessenen Strukturvibrationen des A320 aus Flugtests verglichen.
Das neu entwickelte Autospektrenmodell zeigt eine hohe Vorhersagegenauigkeit innerhalb der definierten aerodynamischen Grenzen. Des Weiteren liegen die

vorhergesagten und gemessenen Strukturvibrationen in einem großen Frequenzbereiche übereinander. Die neue Methode ermöglicht eine CFD basierte Vorhersage der Autospektren überall auf dem Flugzeugrumpf und somit auch die Berechnung der Strukturvibrationsanregung des Rumpfes.

Contents

List of Figures

List of Tables

Nomenclature

Latin nomenclature

$\hat{A}$	Amplitude Function	–
a	Length of Plate	m
A	Area	m^2
$A(\omega)$	Wavenumber Model Function, Smol'yakov & Tkachenko	–
$a_1 - a_{10}$	Wavenumber Model Constants, Efimtsov	–
a-h	TBL Model Empirical Constants, Goody	–
b	Width of Plate	m
B	Bending Stiffness	Nm
$B(\omega)$	Damping Decrement, Smol'yakov	–
B_r	Bending Stiffness (Restoring Force Term)	Nm
$b_{C,T}$	TBL Model Constant, Chase	–
c_f	Friction Coefficient	–
c_p	Pressure Coefficient	–
$C_{M,T}$	TBL Model Empirical Constants, Chase	–
C_1	TBL Model Empirical Constant, Rackl & Weston	–
d_{mn}	Dimensionless Impedance	–
d	Diameter	m
E	Young's Modulus	N/m^2
$\Delta F(k_x, k_y, \omega)$	Wavenumber Correction Function, Smol'yakov & Tkachenko	–
$F(k_x, k_y, \omega)$	Wavenumber Model Function, Smol'yakov & Tkachenko	–
$F_{M,T}$	Wavenumber Model Coefficients, Chase	–
f	Frequency	Hz
FL	Flight Level	100 ft
$\mathcal{G}$	Spatial Gaussian Filter Kernel	–
g	Alternative Specific Dissipation Rate	$s^{1/2}$
G	Green Function	–

G	Wavenumber Model Variable, Smol'yakov & Tkachenko	–
$G(\xi,\ \eta,\ \tau)$	Space-Time Correlation Function	–
h	Energy Balance Function, Smol'yakov & Tkachenko	–
$[k]$	Modal Stiffness Diagonal Matrix	Nm
$[K]$	Stiffness Matrix	Nm
$\mathbf{k}$	Wavenumber Vector	$^1/_\mathrm{m}$
k	Turbulence Kinetic Energy	$^{\mathrm{m}^2}/_{\mathrm{s}^2}$
$k_m,\ k_n$	Wavenumber of Half-Waves in Long. and Lat. Direction	–
k	Wavenumber	$^1/_\mathrm{m}$
L	Correlation Length	m
l_s	Integral Turbulent Length Scale	m
L_γ	Coherence Length	m
$L_{x,y}$	FRPM Patch Length/Width	m
l	Length	m
$[m]$	Modal Mass Diagonal Matrix	kg
$[M]$	Mass Matrix	kg
m	Mass	kg
M	Mass per Unit Area	$^{\mathrm{kg}}/_{\mathrm{m}^2}$
$m,\ n$	Number of Half-Waves in Long. and Lat. Direction	–
m_0	Wavenumber Model Constant, Smol'yakov & Tkachenko	–
m_1	Wavenumber Model Variable, Smol'yakov & Tkachenko	–
Ma	Mach Number	–
n	Wavenumber Model Constant, Smol'yakov & Tkachenko	–
N	Normal Vector	–
$N_x,\ N_y$	Membrane Tension	$^\mathrm{N}/_\mathrm{m}$
$N_{xr},\ N_{yr}$	Membrane Tension (Restoring Force Term)	$^\mathrm{N}/_\mathrm{m}$
p_t	Total Pressure	$^\mathrm{N}/_{\mathrm{m}^2}$
$p_{dynamic}$	Dynamic Pressure	$^\mathrm{N}/_{\mathrm{m}^2}$
p_{static}	Static Pressure	$^\mathrm{N}/_{\mathrm{m}^2}$
p	Pressure	$^\mathrm{N}/_{\mathrm{m}^2}$
Q	Source Term	–
q	Dynamic Pressure	$^\mathrm{N}/_{\mathrm{m}^2}$
Re_x	Reynolds Number based on Leading Edge Distance x	–

Re_{δ_l}	Reynolds Number based on local Boundary Layer Thickness	–
$R(\xi,\ \eta,\ \omega)$	Cross-Spectral Density Function	–
R_T	Ratio of the Outer- to Inner-Layer Timescale	–
Re_τ	Shear Stress Reynolds Number	–
Re_Θ	Momentum Reynolds Number	–
r	Radius	m
R	Specific Gas Constant	$^{\mathrm{J}}/_{\mathrm{kg\ K}}$
Re	Reynolds Number	–
$S_0(\omega)$	Outwardly Radiated Power	W
$S_1(\omega)$	Inwardly Radiated Power	W
$S_d(\omega)$	Structurally Dissipated Power	W
S_m	Wavenumber Model Viscosity Parameter, Smol'yakov	–
$S_t(\omega)$	Vibrational Power	W
S_{mn}	Mass normalised Mode Shape in Wavenumber Domain	–
S	Area	m^2
Sh	Strouhal Number	–
t	Time	s
t	Thickness	m
T	Temperature	°C
$\mathcal{U}_i$	White Noise	–
$\mathbf{u}'$	Fluctuating Velocity Vector	$^{\mathrm{m}}/_{\mathrm{s}}$
U_1	Mean Flow x-direction	$^{\mathrm{m}}/_{\mathrm{s}}$
$u'_{i,j}$	Velocity Fluctuations	$^{\mathrm{m}}/_{\mathrm{s}}$
U_τ	Friction Velocity	$^{\mathrm{m}}/_{\mathrm{s}}$
U	Flow Velocity	$^{\mathrm{m}}/_{\mathrm{s}}$
V	Volume	m^3
$\mathbf{x}$	Field Coordinate Vector	m
y^+	Dimensionless Wall Distance	–
y_w	Wall Distance	m
$Z_{(mnmn)}$	Modal Acoustic Impedance	$^{\mathrm{kg}}/_{\mathrm{m}^3\mathrm{s}}$

Greek nomenclature

$\alpha,\ \beta$	Inverse Coherence Length, Corcos	$^1/_\mathrm{m}$
$\alpha_x,\ \alpha_y$	Coherence Decay Coefficients	–
α_{AoA}	Angle of Attack	°
α_E	TBL Model Empirical Constant, Efimtsov	–
$\alpha_{M,T,P}$	TBL Model Variables, Chase	–
β_{δ_l}	Clauser Parameter	–
$\beta_{\Delta_{\delta_l}}$	Clauser Parameter, with Rotta-Clauser Length Scale	–
β_E	TBL Model Variable, Efimtsov	–
$\Delta\gamma$	Coherence Correction Function, Smol'yakov	–
γ	Coherence	–
γ_c	TBL Model Variables, Goody	–
γ_M	TBL Model Variables, Chase	–
γ_{DG}	TBL Model Variables, Goody	–
γ_m	TBL Model Variables, Goody	–
δ	Boundary Layer Thickness	m
Δ	Rotta-Clauser Length Scale	m
δ^*	Boundary Layer Displacement Thickness	m
Δ_{δ_l}	Rotta-Clauser Length Scale, based on local Boundary Layer Thickness	m
ε	Dissipation Rate of Kinetic Energy	$^{\mathrm{m}^2}/_{\mathrm{s}^3}$
ε_J	Wavenumber Model Modification Factor, Jolly	–
ε_s	Structural Damping Factor	–
η	Separation Distance y-Direction	m
Θ	Boundary Layer Momentum Loss Thickness	m
κ	Adiabatic or Isentropic Exponent	–
λ	Wavelength	m
λ	Kolmogorov scale	m
$\Lambda_x,\ \Lambda_y$	Coherence Length, Efimtsov and Smol'yakov	m
μ_{Ch}	Wavenumber Model Variable, Chase	–
ν	Kinematic Viscosity	$^{\mathrm{m}^2}/_\mathrm{s}$
ν_p	Poisson's Ratio	–
$\boldsymbol{\xi}$	Field Coordinate Vector	m

ξ	Separation Distance x-Direction	m
τ	Time Lag	s
τ_w	Wall Shear Stress	$^{\mathrm{N}}/_{\mathrm{m}^2}$
$\Phi(\omega)$, $\Phi(f)$	Single Point Wall Pressure Spectrum (Auto-Spectrum)	$^{\mathrm{Pa}^2}/_{\mathrm{Hz}}$
$\Phi(k_x, k_y, \omega)$	Wavenumber-Frequency Spectrum	$^{\mathrm{Pa}^2}/_{\mathrm{Hz}}$
Φ_{mn}	Modal Excitation Term	kgm^2
$\tilde{\Phi}(k_x, k_y, \omega)$	Normalised Wavenumber-Frequency Spectrum	–
Ψ	Eigenvector	$^{1}/_{\mathrm{m}}$
Ψ^M	Mass Normalised Eigenvector	$^{1}/_{\mathrm{mkg}}$
ψ_i'	Fluctuating Potential	–
ω	Angular Frequency	$^{\mathrm{rad}}/_{\mathrm{s}}$
ω_D	Specific Dissipation Rate	$^{1}/_{\mathrm{s}}$
ω_{EV}	Angular Frequency of Eigenvector	$^{\mathrm{rad}}/_{\mathrm{s}}$
ω_{tbl}	Angular Frequency of TBL	$^{\mathrm{rad}}/_{\mathrm{s}}$
$\overline{\omega}$	Dimensionless Angular Frequency	–

List of indices

∞	Far Field Quantities	–
$\langle ... \rangle$	Ensemble Average	–
T	Transposed	–
’	Fluctuating Quantities	–
0	Reference Quantities	–
[...]	Matrix Quantities	–
c	Convective Quantities	–
e	Edge Quantities	–
l	Local Quantities	–
m	Unprocessed Quantities	–
mn	Modal Quantities	–
Re(...)	Real Part	–
w	Wall Quantities	–

General abbreviations

A/C	Aircraft
APG	Adverse Pressure Gradient
ATRA	Advanced Technology Research Aircraft
AWB	Acoustic Wind Tunnel Braunschweig
CAA	Computational Aeroacoustics
CAD	Computer-Aided Design
CENT–LSHX	Comfort and efficiency ENhancing Technologies–Liquid to air Skin Heat Exchanger
CFD	Computational Fluid Dynamics
CPU	Central Processing Unit
DLR	German Aerospace Center
DNS	Direct Numerical Simulation
FEM	Finite Element Methods
FPG	Favorable Pressure Gradient
FRPM	Fast Random Particle-Mesh Method
FT	Flight Test
HPC	High-Performance Computing
HTP	Horizontal Tail Plane
ISA	International Standard Atmosphere
JTI Clean Sky	Joint Technology Initiative Clean Sky (EU Research Project)
LES	Large Eddy Simulation
R&T	Research & Technology
RANS	Reynolds Averaged Navier-Stokes
RSMg	Reynolds Stress Model g
SEA	Statistic Energy Analysis
SPL	Sound Pressure Level
TAS	True Air-Speed
TAU	DLR in-house CFD solver
TBL	Turbulent Boundary Layer
TKE	Turbulence Kinetic Energy
TsAGI	Central Aerohydrodynamic Institute in Moscow, Russia
VTP	Vertical Tail Plane

ZPG	Zero Pressure Gradient

1 Introduction

1.1 Motivation and Background

People will spend more and more time on planes, whether for private or business purposes, and their comfort expectance will successively grow. Among other demands on passenger comfort, aircraft cabin noise should be as low as possible. Many sources of noise contribute to the sound pressure level (SPL) inside an aircraft cabin (cf. Figure 1.1). One of the main cabin noise contributors is the turbulent boundary layer (TBL), causing fluctuating pressures on the fuselage. These pressure fluctuations excite structural vibrations and noise. Via complex transfer paths energy is transmitted through the fuselage structure and is radiated into the cabin.

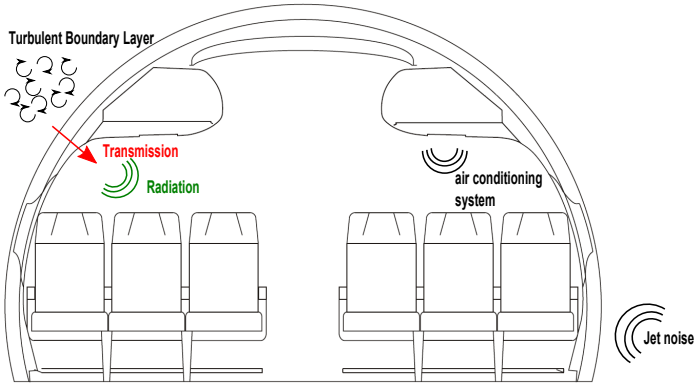

Figure 1.1: Examples of noise sources driving cabin SPL

Aircraft manufacturers, like Airbus, are interested in an exact estimation of cabin SPL at every position inside the cabin. Therefore, detailed knowledge of the structural excitation by TBL is essential, which is addressed in this thesis by using methods like Computational Fluid Dynamics (CFD), Computational Aeroacoustics (CAA) and Statistic Energy Analysis (SEA). This knowledge enables engineers

to implement shape optimisations of the aircraft structure or to improve the insulation concept of todays existing and of future aircraft designs. Finally, this is required to reach the lowest cabin SPL and the highest passenger comfort in the market.
The research objectives of this thesis are presented in detail in Section 1.3 and a brief introductory summary of the state of the art is given below.

1.2 State of the Art

Today, cabin SPL estimations in aircraft are done by using semi-empirical models on the TBL excitation side. According to the work of Miller [66], available prediction methods can be classified into three categories, sorted by complexity of the used field statistics and prediction output, i. e. models which are mainly described by

a) the overall mean square pressure as a direct measure of the energy due to the pressure fluctuations beneath the TBL,
b) the single point wall pressure spectrum (auto-spectrum) sorting this energy into frequencies, or
c) the wavenumber-frequency spectrum, further sorting the energy into wavenumbers, i. e. providing correlation information in time and space.

In this thesis the focus is on the auto-spectra as well as on the wavenumber-frequency spectra prediction, to characterise the TBL excitation. In the last fifty years many semi-empirical models to predict surface pressure fluctuations beneath a TBL have been developed for a large variety of test conditions.

The development of models for auto-spectra prediction begins with the work of Robertson [71] in 1971, which is based on the work of Lowson [63] (1968) and constitutes an improvement at low and high Strouhal numbers. Furthermore, Lowson's work is originally based on work of Speaker and Ailman [81]. Robertson takes flight test and wind tunnel data, in a range of $\mathrm{Ma}_\infty = 0.6...3.0$, for his model into account. In 1974, Cockburn and Robertson [15] conducted tests on a payload shroud at $\mathrm{Ma}_\infty = 0.7,\ 0.8,\ 2.0$. They proposed an enhanced model, based on the work of Robertson. Different other models were developed, like the model by Chase in 1980 [12] or the Efimtsov models in 1982 [20] and 1984 [19]. The Efimtsov 1 model [20] was developed based on flight test data in the Mach number range of $\mathrm{Ma} = 0.41...2.1$. Further wind tunnel measurements ($\mathrm{Ma}_\infty = 0.015...4.0$) at TsAGI (Central Aerohydrodynamic Institute in Moscow,

Russia) enabled Efimtsov to enhance his model to the Efimtsov 2 model [19]. Many more models have been developed in the 80s and 90s by e.g. Howe [51], Smol'yakov [77] and Tkachenko [86]. In the early 2000s, Goody [37] proposed a new model, based on the Chase model. Also, Rackl & Weston [70] proposed an enhancement of the existing Efimtsov 2 model. All mentioned models were developed for different speeds and Reynolds numbers but always for zero pressure gradient flows. In a next stage of development, Rozenberg [73] published a model for auto-spectra prediction under adverse pressure gradients, using the Goody model as a starting point. Catlett [10] did the same in 2014 and Hu [53] in 2016. This gives a rough overview of the models, developed in the last 50 years. Another detailed overview of the last 50 years on the field of development of semi-empirical models, which calculate the turbulent boundary layer wall pressure frequency spectrum (auto-spectrum) has been summarised by Hwang [56], whose work is based on observations from Bull [8], Farabee [31], Blake [4, 5] and others. A more detailed overview of the existing models to estimate auto-spectra is given in chapter 3.1.

Beside the information delivered by the auto-spectrum, it is essential to have knowledge about the space and time development of the turbulence. For this purpose many models for the wavenumber-frequency spectrum are available. Again, the development of these models started in the 60s with the work of Corcos [17]. Corcos' idea was to divide the flow into two parts, the flow direction itself and the cross flow direction. The decay in turbulence for both directions is estimated with exponential-functions. This model does only describe the convective region, where most of the energy of the TBL is positioned and is the major driver of exciting structures on aircraft (cf. Graham [43]). Jolly [14] enhanced the Corcos model in 1968 with the local boundary layer thickness δ_l as this is important at low frequencies. Following the same idea of dividing the flow (flow- and cross flow direction) and taking δ_l into account, Efimtsov [20] developed a model in 1982, as well based on correlation measurements. Smol'yakov and Tkachenko [79] also performed wind tunnel measurements at $U_\infty = 40\,\mathrm{m/s}$. Their model is an approximation of these measurements and the difference to the beforehand mentioned models is a mixture of the flow and cross flow direction to realise an elliptical shape of the convective ridge, instead of a rhombic shape. Smol'yakov extended this model by taking the viscosity of the fluid into account and published it in 2006 [78]. Finally, also Chase proposed two models for the wavenumber-frequency spectrum, the first one in 1980 [12]. A second model [11] was published in 1987, where Chase included terms to describe the acoustic region and relaxed the requirement for a low wavenumber dependence $\sim |\mathbf{k}|^2$ (Kraichnan-Phillips theorem [61, 50]). All these models are in detail presented in chapter 3.2.

In addition to these semi-empirical models, it is possible to estimate the quantities (auto-spectra, wavenumber-frequency spectra) by numerical methods. The development of high-performance computing (HPC) systems enables the computation of the fluctuating pressure field by several methods, like direct numerical simulation (DNS) and large eddy simulation (LES). Publications from Spalart [80] in 1986 and Gloerfelt & Berland [34] in 2009 are worth to be mentioned respectively. A drawback in these methods is still the numerical cost, which is out of range for computations of real aircraft structures at high Reynolds numbers. Therefore, these methods are today limited to smaller applications at low Reynolds numbers. For industrially relevant geometries the Fast Random Particle-Mesh Method (FRPM) of Ewert [25] can be used to reconstruct synthetic turbulence. This stochastic realisation uses time averaged turbulence statistics from Reynolds averaged Navier-Stokes (RANS) calculations and the pressure field can be calculated by solving the Poisson equation.

Beside this, the coupling of TBL to an aircraft structure is of interest for the SPL estimation inside the cabin. Therefore, vibration analysis is of interest within this thesis. Conventional vibration analysis is based upon a mathematical model which precisely represents the geometric forms, interconnections, boundaries and stiffness related properties of the various components of a structure, together with the applied forces or displacements. The solutions represent its vibrational response at different locations in terms of displacements, accelerations, etc., over a predefined range of frequency.
Noise and vibration problems in aircraft involve very complex structures consisting of many different forms of components. In conventional analysis (e.g. finite elements methods (FEM)) this poses different problems for two main reasons. Firstly, the size of the computational model becomes very large and therefore the time to solve the problem severely increases and it becomes impossible to handle the amount of data necessary for full aircraft models of higher frequencies. For higher frequencies more detailed FEM meshes are necessary and the data volume further increases. Secondly, high frequency modes are increasingly sensitive to small variations of the system properties so that a lack of precise knowledge on the model leads to uncertainties in the prediction process [29]. These reasons render a conventional analysis impossible for complex structures at high frequencies. However, SEA provides an alternative approach to analyse complex structures by dividing a complex model into smaller oscillatory subsystems and estimates the power flow between these coupled multimode subsystems. The vibrational energies of these subsystems representing a certain type of wave, are the main output of SEA calculations. Contrary to the conventional analysis, the calculation of

magnitude and phase quantities of a dynamic system at a particular coordinate location is not within the scope of the method. However, the goal is to calculate averaged dynamic vibration levels for rather broad frequency analysis of a larger part (subsystem) of the model. The SEA is most suitable for cases of broadband excitation over a bandwidth encompassing many natural frequencies (eigenmodes) [30]. The energy received by a fuselage structure from pressure fluctuations of the TBL can be calculated by a modal based approach that uses the eigenmodes of the structure. Evaluations of models for TBL induced noise into aircraft were done by Graham in 1993 [38]. Graham developed a method of how to do this calculation for a flat plate, which was published in 1996 [41]. Furthermore, he established a method for a trimmed flat plate in [42] and examined the influence of curvature [40], as well. Today, commercial software like VA One[1] is used for these applications in aircraft development. Further information about SEA can be found in the thesis of Callsen [9] and in a paper of Borello and Nguyen van Lan [6].

For the validation of the calculations, an unique pool of data is available at German Aerospace Center (DLR) and Airbus. The data base is gathered during several flight test campaigns of DLR and Airbus on DLR's Airbus A320 Advanced Technology Research Aircraft (ATRA). More than 100 Brüel & Kjaer aircraft surface microphones (Type 4948-W-003) and Kulite XCL-093 pressure transducers were installed on the outside of the fuselage. Furthermore, vibrational measurements with accelerometers on the primary and secondary structure are available. Finally, a bunch of microphones were installed inside the cabin as well. A good overview of the instrumentation is given in the work of Spehr et al. [82]. Results of correlation analysis are given by Haxter [46–48] and auto-spectra analysis by Klabes [57].

1.3 Scope and Research Objectives

The present work addresses the development of a full tool chain to estimate aircraft fuselage vibration at cruise flight conditions. This work includes two streams, a numerical and a semi-empirical one, to calculate the TBL excitation. Therefore, a new CFD based auto-spectrum model for aircraft in cruise flight conditions with and without moderate local pressure gradients is developed. Beside this, in the second stream, CAA tools are employed to calculate the same quantities. This new model and the pure numerical results are validated with flight test data.

[1] Commercial SEA software of ESI Group (https://www.esi-group.com/de/software-loesungen/virtual-performance/va-one, 07.09.2016)

Furthermore, the structural vibration of a simply supported flat plate test case as well as of a real aircraft structure is calculated by using SEA. Finally, the SEA estimation of structural vibration is validated with measured structural vibrations from the mentioned flight test campaigns.
The working tasks, to achieve these goals are the following:

- Postprocessing and analysis of the mentioned flight test data in terms of auto-spectra, to prepare a reliable validation data base.
- Extensive study of existing semi-empirical models for auto-spectra prediction and comparison with measurement data base.
- Conduct CFD calculations equal to the flight test configurations, to gain detailed knowledge of the aerodynamics all-around the aircraft.
- Development of an enhanced auto-spectra prediction model, based on CFD input data and validation with flight test data.
- Performing CAA computations of auto-spectra and wavenumber-frequency spectra as an input for SEA.
- Coupling TBL excitation with a simply supported flat plate for parameter studies to analyse the influence of different auto-spectra and wavenumber-frequency models and their robustness against parameter variation.
- Coupling TBL excitation from semi-empirical and numerical models to real aircraft structures by making use of SEA.
- Validate the SEA estimations of structural vibration with in-flight measured vibrations.

1.4 Outline

This thesis is structured as follows:
Chapter 2 gives a detailed overview of the existing flight test data, which is used for validation. Furthermore, a data correction as well as a comparison is done within this chapter. In chapter 3, a literature review of the most relevant and most often cited auto-spectra and wavenumber-frequency models is presented. Beside this, Graham's [41] coupling method is briefly reviewed and the way of how it is employed within this thesis is pointed out. Information about the CFD calculations and the analysis is given in chapter 4. Based on the knowledge about the aerodynamics all-around the aircraft and the capabilities of existing auto-spectra models, an enhanced model is developed in chapter 5.1. In chapter 5.2, CAA methods are depicted, which facilitate the prediction of auto-spectra and wavenumber-frequency spectra using CFD input. This method can be seen as

a second stream in parallel with the semi-empirical models to calculate input data for the structural vibration calculation. Afterwards, in chapter 6, all results of the new semi-empirical model and the numerical predictions are presented in comparison with flight test data. Finally, in chapter 7 the conclusion of this thesis and an outlook is given.

2 Experimental Validation Database

This chapter provides an overview of the experimental data base, used for the validation of the developed methods and tools. Flight test data were gathered during three different test campaigns for different flight configurations (cf. Figure 2.1) on the A320 ATRA. During these test campaigns the focus was on different areas of the aircraft, which are marked with different colours in Figure 2.2. Here, blue depicts the front, red the mid and green the aft area, respectively. The data availability for each campaign is in detail shown in Figure 2.1. Here, the grey marked flight level (FL) and Mach number combinations denote the configurations which are mostly focused on, within this thesis. Chapter 2.1 gives a detailed overview of the installed sensors and their positions. Afterwards, in chapter 2.2 results of the auto-spectra analysis and data correction are shown.

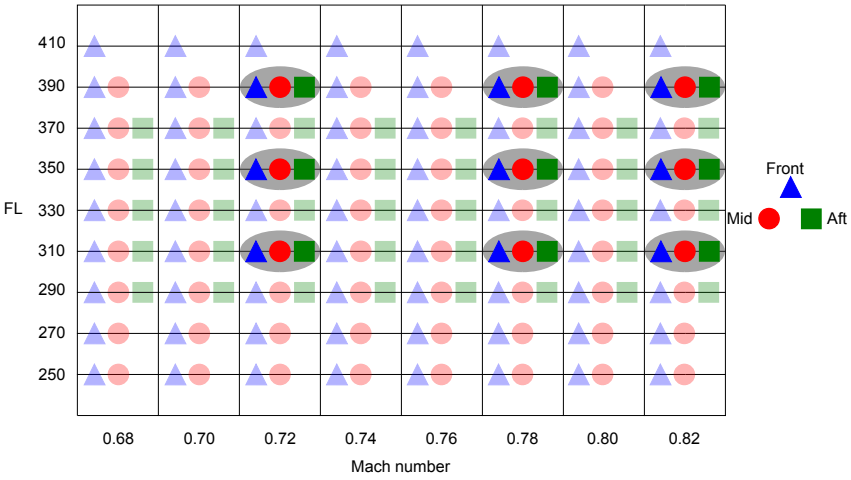

Figure 2.1: Flight test configurations and data availability [57]

2.1 Experimental Setup

The experimental setup, which is of interest within this thesis, consists of surface microphones, piezoresistive pressure transducers and accelerometers. Firstly, the arrangement and installation situation of microphones and pressure transducers on the outer skin is presented in chapter 2.1.1. Secondly, the positioning of accelerometers on the primary structure is illustrated in chapter 2.1.2.

2.1.1 Pressure Measurement Equipment

Kulites

Kulite pressure transducers of type XCL-093 [82] were installed during all three test campaigns and thus in all areas of the aircraft (**front**, **mid**, **aft**). For each configuration, a total of 30 transducers were installed in three dummy windows, which replaced the standard passenger windows. The exact window positions are depicted in Figure 2.2 as coloured windows. For the front area it is, e.g. window 2...4. Figure 2.3 describes the arrangement of these sensors in each window in detail. The sensor arrangement is optimised for correlation analysis and therefore each sensor has one longitudinal and one lateral neighbour. Furthermore, they are arranged in a quasi-randomised way to enhance the possibility of wavenumber-frequency analysis because of an increase in spatial resolution. The Kulite installation setup was developed by the DLR team of Spehr and is described in [82].

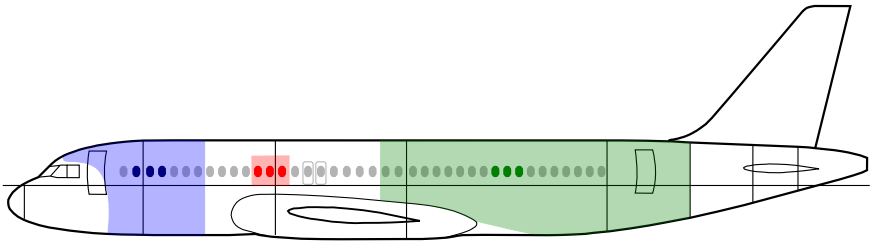

Figure 2.2: Sketch of ATRA with Kulite positions (wing profile changed)

The sensors are not directly exposed to the flow but recessed installed behind a small hole of $d = 0.3 \cdot 10^{-3}$ m diameter, that is drilled into the dummy windows. In detail this is sketched in Figure 2.4. The Kulite sensor itself is shown in red,

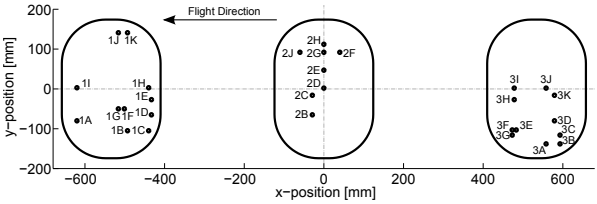

Figure 2.3: Kulite installation details (array-fixed coordinates), compare [57] and [82]

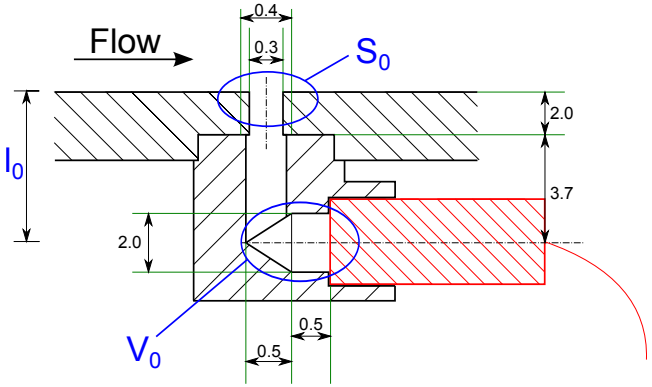

Figure 2.4: Kulite (red) installation situation (dimensions in mm), according to [45]

lying parallel to the surface of the dummy window and therefore parallel to the flow. Different cavities between flow and sensor causes a Helmholtz resonance that limits the usable frequency range for the auto-spectra analysis, which is discussed in detail in chapter 2.2.

Microphones

Beside the Kulite pressure transducers, which are limited to be installed in the passenger window plane, flush mounted microphones were installed. These flush mounted sensors of type Brüel & Kjaer 4948-W-003 (special type of 4948-A) were only installed during two flight test campaigns and only in two regions (**front** and **aft**). The sensor installation and data recording was performed by Airbus during the campaigns. The sensor itself has a membrane diameter of $d = 10.3 \cdot 10^{-3}$ m, especially developed for aircraft applications. A big advantage of these sensors

is the flexibility of the positioning because they can be glued everywhere on the surface of an aircraft. The flush mounted microphones were installed in groups of three or five sensors as well as stand-alone microphones. A group of three sensors is always installed in the form of a so called Triplet and all other arrangements are composed of stand-alone microphones. These two basic types are sketched in Figure 2.5, where the microphones are depicted as black dots. One can see that the microphones are surrounded by a grey area. This denotes the backing material of the microphones, a rubber like mat of t = $4 \cdot 10^{-3}$ m thickness which can be glued on the fuselage surface, triangular in shape for the Triplets and circular for the stand-alone microphones. This mat decreases linearly in thickness to the edges, where it is close to zero.

Figures 2.6 (a) and (b) present the sensor installation of flush mounted micro-

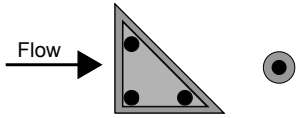

Figure 2.5: Sketch of flush mounted microphones (black dots) with backing material (grey), compare [57]

phones in the front aircraft and cockpit area with the respective naming. In these areas, stand-alone microphones are installed solely. Furthermore, the cockpit area contains antennas, which are not shown in the graphics. However, they influence the auto-spectra and are not under detailed analysis within this thesis. Data of undisturbed sensors, measuring TBL, are shown in chapter 2.2.3 only.

Beside the front area, the aft area was also equipped with flush mounted sensors, which are presented in Figure 2.7. Here, stand-alone microphones are denoted in blue and in an arrangement of five, they are plotted in red on a grey subfont. All other sensors are installed as Triplets, named with the Triplet number (Txx or Trxx) and the respective name of each microphone. Triplets Trxx are rotated by a specific angle, as depicted in Figure 2.7.

2.1.2 Vibration Measurement Equipment

Beside the pressure fluctuation measurements on the outer surface, vibrational measurements on the primary structure were performed as well. Therefore, accelerometers of type PCB M352C65 with an approximate weight of 2.8 g were installed. According to the Kulite window positions, the accelerometers are mainly

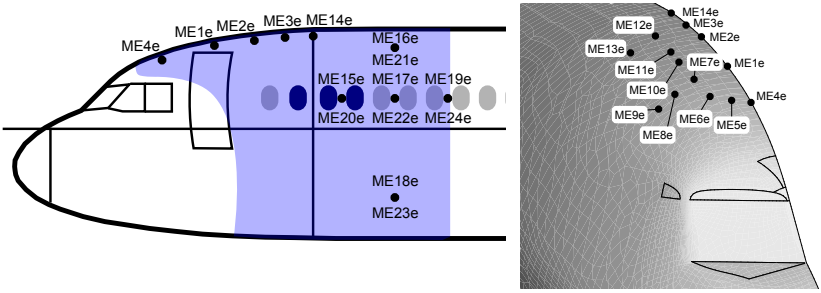

(a) 2D side view

(b) 3D view of a cockpit half model

Figure 2.6: Sketch of ATRA with front and cockpit microphones

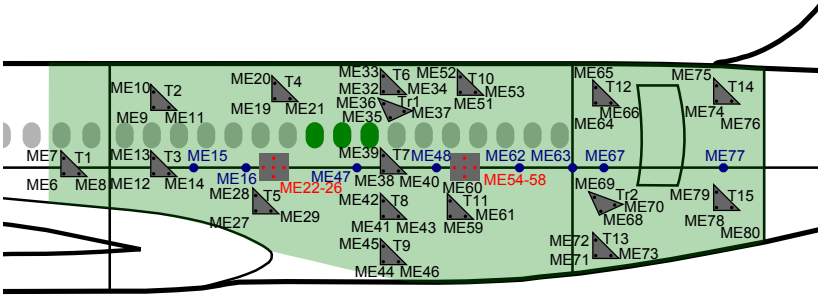

Figure 2.7: Sketch of ATRA with aft sensors

installed in the respective three frame bay areas from floor to roof. Few accelerometers are installed in the adjacent frame bays as well. Figure 2.8 presents the positions for the mid aircraft area, with the Kulite windows included as reference. The red numbers denote radial and the blue numbers longitudinal sensor measurement direction. Furthermore, "f" denotes positioning on a frame, "s" on a stringer, "fs" on a frame at frame/stringer crossing, "sf" on a stringer at stringer/frame crossing, "r" on a window frame and finally "a" on an attachment point. Beside this, the rolled off fuselage is divided into different subsystems, according to the SEA models

- Stringer 1...5: Roof,
- Stringer 5...11: Roof lower,
- Stringer 11...14: Sidewall upper,
- Stringer 14...18: Win/Sidewall,
- Stringer 18...23: Sidewall lower.

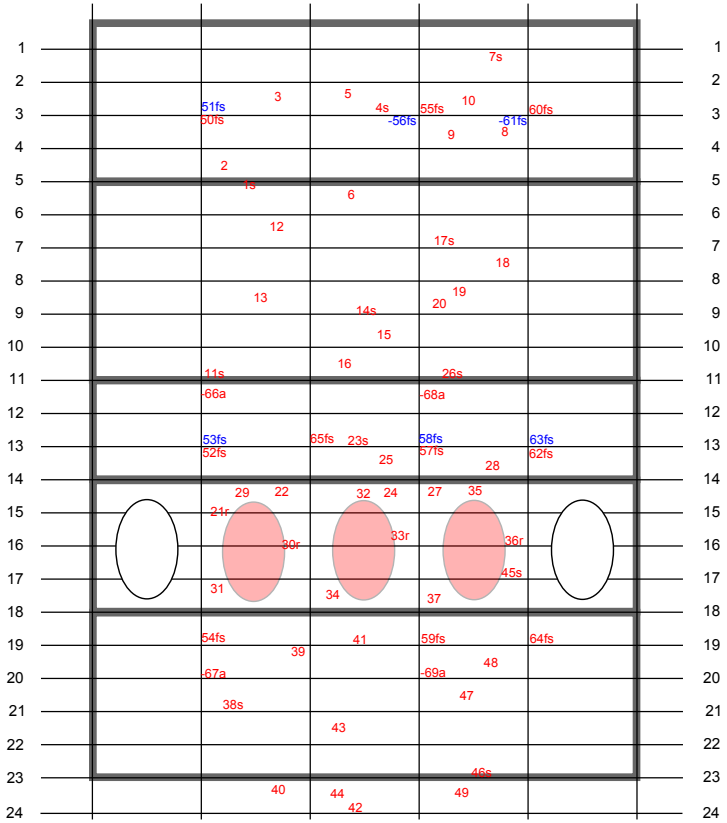

Figure 2.8: Accelerometer positions in mid area

Figure 2.9 presents the accelerometer layout for the aft region of the aircraft, which is a pretty similar layout, compared to the mid area. The accelerometer arrangement for the front region is not shown here, but it is similar to the mid

and aft region for all subsystems. Except for the Roof lower region, where no accelerometers were installed.

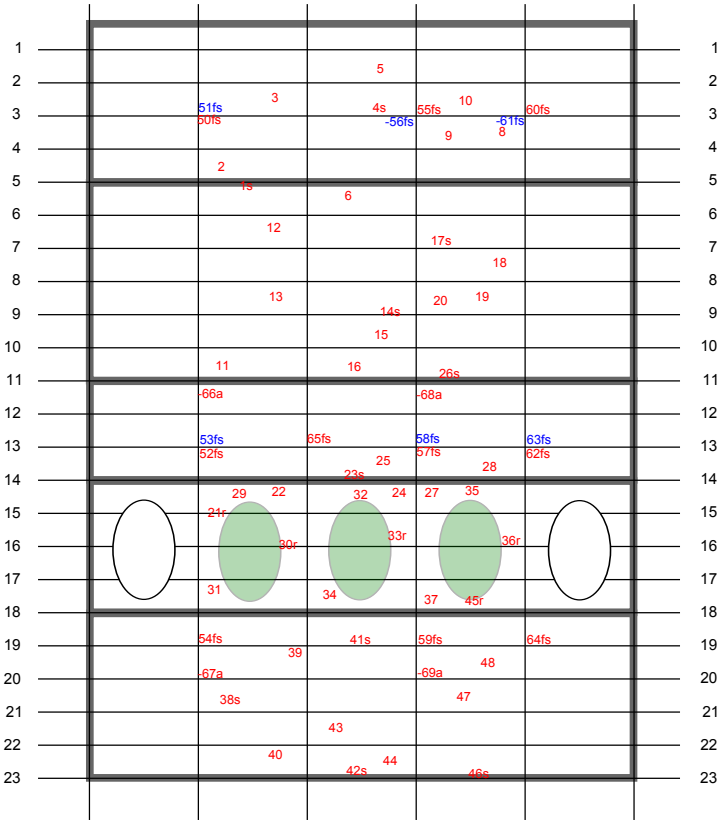

Figure 2.9: Accelerometer positions in aft area

2.2 Auto-Spectra Measurement

In this chapter, an overview of the measured auto-spectra data is given. First of all, a correction for the B&K microphones is performed due to the sensors surface size. Secondly, the sensor installation of these sensors is discussed (cf. chapter 2.2.1). In

a third step, the Kulite installation is surveyed and the impact on the auto-spectra is discussed. Beside that, usable validation auto-spectra for further analysis are shown in chapter 2.2.2 for standard cruise flight condition (Ma = 0.78, FL350). Finally, in chapter 2.2.3, the data variation at different positions on the aircraft is presented and discussed, as well as the influence of different flight levels and airspeeds on the auto-spectra.

2.2.1 Data Correction and Deficiencies

B&K Microphones

The first mentioned phenomenon occurs in the high frequency range, due to the size of the sensor's sensitive surface. Very small structures, relative to the sensor size, are associated with high frequency pressure fluctuations. However, the size of the sensor limits the spatial resolution and therefore attenuates the measured high frequency part in the auto-spectrum. Corcos [16] developed a correction for this spatial resolution problem, which is applied to the data. Corcos investigated the attenuation of the frequency spectral density for square and round transducers. In [16] a table with attenuation factor $\frac{\Phi}{\Phi_m}$ (Φ, corrected auto-spectrum; Φ_m, uncorrected measured auto-spectrum) dependent on the similarity variable $\frac{\omega \mathrm{r}}{\mathrm{U_c}}$ is provided, which is also plotted in Fig. 2.2.1. With $\mathrm{U_c}$ as the convective velocity and r as the radius of the round transducer sensitive face. In general, the convective

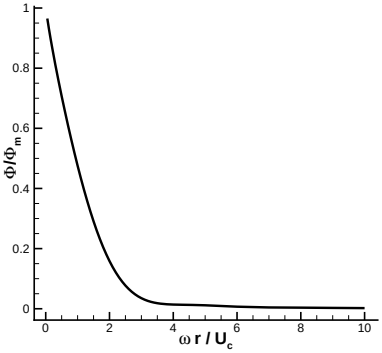

Figure 2.10: Corcos attenuation factor over Strouhal number, according to [16]

velocity is a function of frequency and a fraction of free stream velocity. For

this correction, measured U_c values from the mid flight test campaign are used. Haxter & Spehr [48] found that U_c is nearly a linear function of frequency beginning at 475 Hz with $U_c/U_\infty = 0.9$, decreasing to a value of 0.75 at $f = 5000$ Hz. For higher frequencies, U_c is assumed to be a constant fraction of $U_c = 0.75 \cdot U_\infty$. Instead of U_∞, the local boundary layer edge velocity U_e at every position of analysis is used for the correction, because of varying velocities around the aircraft. U_e is taken from CFD data, whose analysis is in detail described in chapter 4.
The Corcos corrected data, exemplarily for Triplet 7 (cf. Figure 2.7), is presented in Figure 2.11(a). It shows ME38 and ME40 at Ma = 0.78 and FL350, which are representative in their characteristics for all B&K microphones. According to the Corcos correction model, a significant attenuation of the signal begins at $f \approx 1500$ Hz, when calculating the convective velocity based on the edge velocity U_e of the turbulent boundary layer. Therefore $U_e = 231,5\,\mathrm{m/s}$ is taken instead of $U_\infty = 237\,\mathrm{m/s}$. Taking the data from [48] into account, U_c can be calculated as $U_c = 0.83 \cdot U_e$ at 1500 Hz. Figure 2.11(a) presents the raw measurement data for ME38 (black), which is a sensor positioned at the leading edge of the Triplet and for ME40 (red), which is the sensor close to the Triplet's trailing edge. The green curve shows the Corcos corrected data for ME40, it is observable that the correction overshoots in the higher frequency range above $f > 2500$ Hz, compared to the theoretical expected f^{-1} slope. This behaviour was already determined at other measurement campaigns in DLR's Acoustic Wind Tunnel Braunschweig (AWB). As best practice, it is decided to take the energetic mean value between the measured and corrected data. This data is represented by the magenta coloured line and follows perfectly the f^{-1} slope, denoted in black, which is expected from theory in this frequency region. Details about the expected spectral shape are presented in chapter 3. The correction gives a delta of 0.9 dB at $f = 3000$ Hz and 4.9 dB at $f = 10000$ Hz. Compared to the unmodified corrected values, this is a difference of 0.7 dB and 2.2 dB for 3000 Hz and 10000 Hz, respectively.

Beside the high frequency correction, a low frequency phenomenon was observed for some microphones, which is also visible in Figures 2.11(a) and 2.11(b) below $f < 400$ Hz. In Fig. 2.11(b) the red line (ME40) appears trustworthy below $f < 400$ Hz in contrast to ME38 and ME39. All three auto-spectra are measured on Triplet 7 (Fig. 2.7). ME38 and ME39 are positioned close to the Triplet's leading edge (compare Figure 2.5), which are contaminated by a small step induced flow irregularity upstream the microphones. Microphone ME40 is on the bottom right position, ME38 on the bottom left and ME39 on the top left position. For stand-alone microphones an equivalent effect is observed in the spectra (ME47). Therefore, it is important to derive a correction of this effect from Triplet instal-

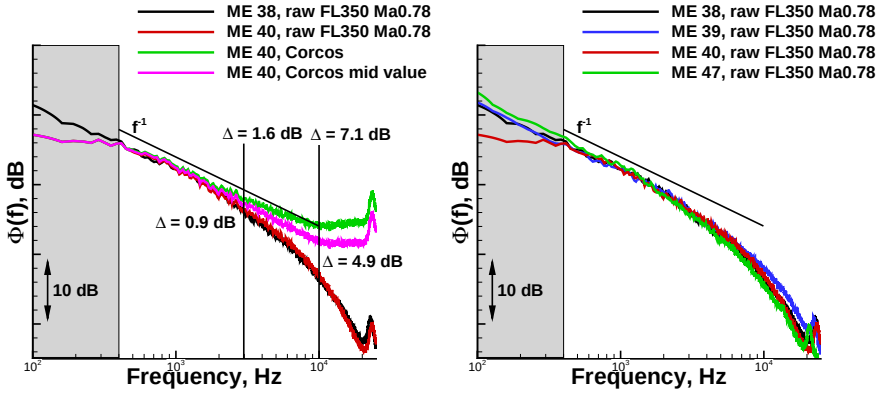

(a) Corcos Correction and low frequency issue at Triplet

(b) Low frequency issue at Triplet and stand-alone sensors

Figure 2.11: B&K Microphone Data Corrections and Deficiencies, similar to [57]

lations, to correct the spectra of stand-alone microphones because in some areas only single microphones are installed. In the mentioned example, only ME40 is assumed to represent correct spectral shape below $f < 400$ Hz. A wind tunnel test was executed in the AWB, to find a correction function for the low frequency behaviour. This aim could not be reached, it was only possible to reproduce the effect with a much bigger step in front of the sensors. Reasons for that are probably the lower velocity in the wind tunnel (max. $U_\infty = 60\,^{m}/_{s}$) and the thin TBL. Furthermore, the effect in the auto-spectra may be provoked by a separation bubble due to the step. This topic was not under further investigation during this thesis and the data from nearly all stand-alone and leading edge Triplet microphones is classified as reliable above $f > 400$ Hz for all B&K microphones. Some exceptional cases are found, where the auto-spectra from B&K microphones are not increasing in level below $f < 400$ Hz and therefore some data is reliable up to a lower frequency. Also a different behaviour is observed for sensors under very thin boundary layers, where the reliable range of the auto-spectrum begins at higher frequencies. Always the change in slope and therefore the increasing behaviour in level with decreasing frequency is taken as a criterion to define the trustworthy frequency range. More about the subject of can be found in [21], [22] or [44].

Kulite Pressure Transducers

In comparison to the presented microphone measurements, Figures 2.12(a) and 2.12(b) depicts Kulite measurements for the front and aft measurement region, respectively. All microphone data in Figure 2.12 is CORCOS corrected (Corr.).

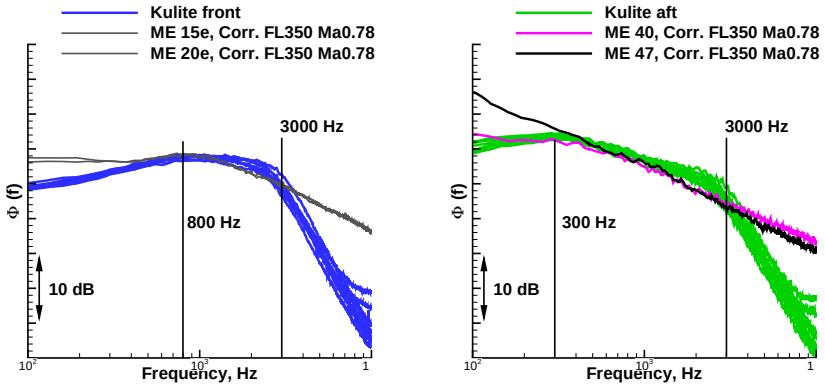

(a) Front area (b) Aft area

Figure 2.12: B&K Microphone compared with Kulite auto-spectra, similar to [57]

For all Kulite data, a steep drop in spectral level is visible above $f \gtrapprox 3000$ Hz, independent from the position on the aircraft. The reason for this seems to be the sensor installation situation, which was presented in Figure 2.4. Based on that drawing, a Helmholtz resonance frequency of $f = 3349$ Hz is calculated by Equation (2.1).

$$f = \frac{c}{2\pi} \cdot \sqrt{\frac{S_0}{V_0(l_0 + \frac{\pi}{2}r)}} \tag{2.1}$$

With c denoting the speed of sound, S_0 as the pinhole area with radius r, V_0 as the volume of the cavity directly in front of the sensor and l_0 as the distance between pinhole and sensor. Due to slightly different installation of each Kulite sensor, this frequency varies somewhat. Beside this, the Kulite pressure transducers do not have a linear frequency-response characteristic. Calibration tests with a loudspeaker set-up showed a contaminated frequency-response, individual for every Kulite. This calibration method is a simplified set-up with a loudspeaker, without any testing under real TBL conditions. Therefore, a retrospectively performed

calibration is not possible and it is decided to trust the data up to $f \approx 1500$ Hz, as long as it follows the CORCOS corrected microphone measurements.

2.2.2 Validation Auto-Spectra

With the limitations of different sensor types and different sensor installation situations, highlighted in chapter 2.2.1, validation auto-spectra can be combined for the whole frequency range ($f = 100$ Hz ... 10000 Hz). This is possible for the front and aft aircraft region, where all different sensor types are installed side by side. For the front area, the validation auto-spectrum is given in Figure 2.13(a),

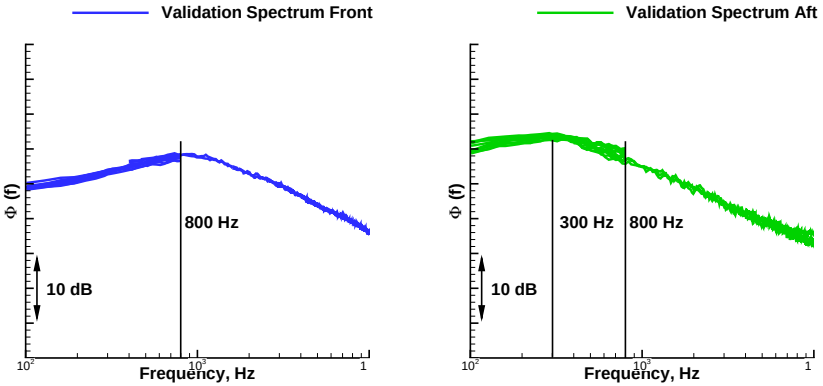

(a) Front area

(b) Aft area

Figure 2.13: Validation auto-spectra, similar to [57]

with a maximum at $f = 800$ Hz. Kulite data from the front region is plotted from $f = 100$ Hz ... 800 Hz and data from B&K microphones ME15e and ME20e from $f = 400$ Hz ... 10000 Hz. Therefore a data overlap of 400 Hz is ensured. Figure 2.13(b) shows the respective validation auto-spectrum for the aft region, with a maximum at $f = 300$ Hz, for orientation, the 800 Hz line from the front spectrum is plotted as well. Kulite data from the aft region is shown from $f = 100$ Hz ... 800 Hz and data from B&K microphones ME38, 39 and ME40 from $f = 400$ Hz ... 10000 Hz. The presented validation auto-spectra are valid for Ma = 0.78 and FL350 and idle engine thrust conditions.

2.2.3 Data Comparison

This chapter gives an overview of the measured data all over the fuselage and an impression of the influence of position variation as well as Mach number and flight level variation.

Varying measurement position

An effect of varying measurement positions and thus varying running length can be studied best by considering data from areas with more or less undisturbed flow. In more specific terms, this means without strong pressure gradients, flow separation or any installation effects. Therefore, data from areas around the Kulite windows are taken. The Kulite window sensors in the front area are installed at x = 9.2 m, the window in the middle is at x = 15.0 m and the most backwards Kulites are located at x = 26.0 m, measured from the aircrafts nose. In Figure 2.14(a) data from FL350 and Ma = 0.78 are presented. It is x = 9.2 m blue, x = 15.0 m red and x = 26.0 m green lines respectively. The trend is as expected, with increasing x-value, the spectra increase in the low frequency region and decrease in the higher frequency region. This reflects the development of the TBL thickness, the larger x, the thicker the TBL and therefore, bigger structures dominate the spectra. An equivalent trend can also be seen in the B&K microphone data, which are plotted in figure 2.14(b) for the front ($x \approx 9.9$ m) and aft ($x \approx 26.5$ m) positions. One can see data from stand-alone microphones for the front region and data from a downstream Triplet microphone for the aft region. The Triplet trailing edge microphone shows trustworthy data in the frequency range between $f = 200$ ... 10000 Hz. Stand-alone microphone data are affected by the step upstream the sensors between $f = 100$ ... 400 Hz. Therefore, data is plotted beginning at $f = 400$ Hz. However, the effect of increasing x is equal for all beforehand mentioned sensor types.

Beside the comparison of data, being a long distance away from each other, data comparison can be done in a small cockpit area as well (cf. Figure 2.6 for sensor positioning). The area beginning close to the cockpit windows (ME5e) and ending at a x-position near the front Kulite windows (ME12e) experiences the highest pressure gradients of the whole measurement campaign, due to the increasing diameter of the cockpit. Furthermore, the effect of sensor installation for the stand-alone microphones is clearly present in the analysis, which is not shown here. The thinner the TBL thickness, the larger the contaminated low frequency area. Therefore, ME5e is trustworthy beginning at $f \approx 1700$ Hz, ME7e/8e at $f \approx 650$ Hz and ME10e/11e/12e at $f = 500$ Hz. The effect of the contamination

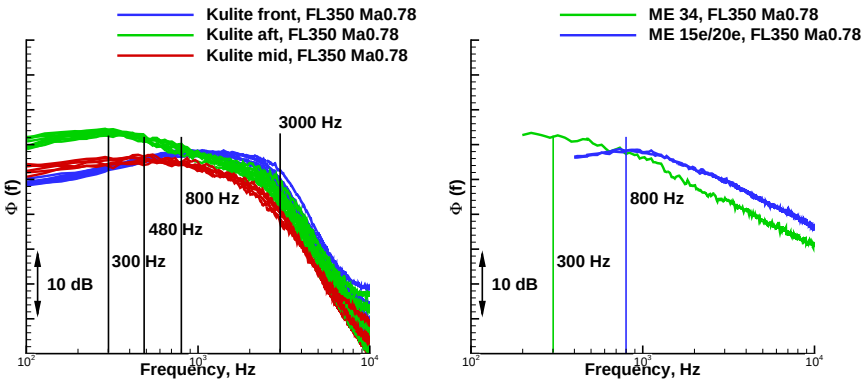

(a) Kulites (b) Microphones

Figure 2.14: Data comparison front, mid, aft, similar to [57]

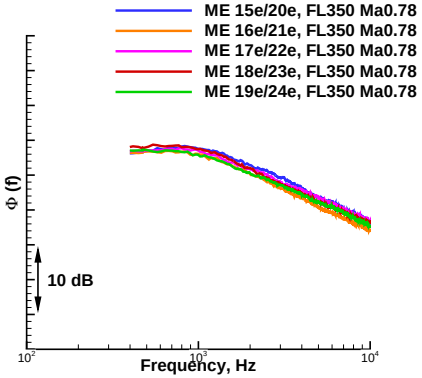

Figure 2.15: Data comparison front fuselage area [58]

and its influence on the plotted frequency range is unclear for sensors under very thin boundary layers and could not be further quantified due to limited data in similar areas. Also a variation in the high frequency slope is present, which results from different pressure gradients on the cockpit. The aerodynamic properties are discussed in more detail in chapter 4. Sensors, close to the front Kulite windows, from the top, mid and bottom fuselage position, are presented in Figure 2.15. Due

to equivalent flow conditions and running length, there is nearly no variation in the spectra visible.
In addition to the data comparison in the front area, further comparison can be made with microphones located between the trailing edge of the wing and the horizontal tail plane (HTP) / vertical tail plane (VTP) zone. This region is shown in Figure 2.7 and the chosen sensors for a first analysis are located in a straight line above and parallel to the passenger windows. In Figure 2.16(a), the measured auto-spectra are compared, beginning at x = 22.1 m (ME21) and ending at x = 30.5 m (ME76). Microphones are distributed equidistantly. At first glance it is striking that there is nearly no change in the spectra with varying x. However, this is an expected result, which can be partly explained with the development of the local boundary layer thickness δ_l. From x = 22.1 ... 30.5 m the thickness of the boundary layer is increasing by roughly 25% (flat plate estimation), corresponding to a level increase of order 1 dB which cannot be resolved by the respective measurements (lies within the data scattering). In contrast, the local boundary layer thickness is always doubled from front to mid and from mid to aft as well, therefore the increase of 3 dB in level at low frequencies can be explained, compare Fig. 2.14(a). Comparison for measured auto-spectra with equal x-position (T6-T9 & Tr1) are depicted in Figure 2.16(b), with varying circumferential position. Even here, no significant change is visible, which means that the influence of the wing has already vanished or the influence is equal for the whole circumferential fuselage. The wing wake influence is visible when comparing data directly behind the wing, which is presented in Figure 2.16(c) (T5, T8, T9, T11) and Figure 2.16(d) (T5, T8, T11, Tr2, T15). Especially in the lower frequency range, below 1000 Hz spectra are varying of more than 5 dB. ME29 shows the highest levels, due to its closest location to the wings trailing edge and the therefore high amount of turbulence. With increasing distance, spectra are decreasing in level because of decreasing turbulence. In Figure 2.16(d) also a little change in the high frequency slope is present, which is caused by the conical shape of the fuselage and hence by changing flow conditions in terms of pressure gradient. Changes in the auto-spectra, affected by the fuselage/wing interaction are constituted in Figures 2.17(a) and 2.17(b). Comparing ME8, ME9/10 and ME14, one would expect the lowest auto-spectrum at ME8 and equal auto-spectra for the remaining microphones. However, the effect is the other way round, ME8 shows the highest level and values are decreasing to ME14 and further decreasing to ME9/10. This effect can be explained by the increase in turbulence, due to the fuselage wing interaction and the wings trailing edge. ME9/10 shows the lowest levels and lower levels than ME14 because of a larger separation to the wing. Also, Figure 2.17(b), where all microphones close to the Belly Fairing are presented, show a huge dependency on the local flow conditions. In summary, it can be stated that there is

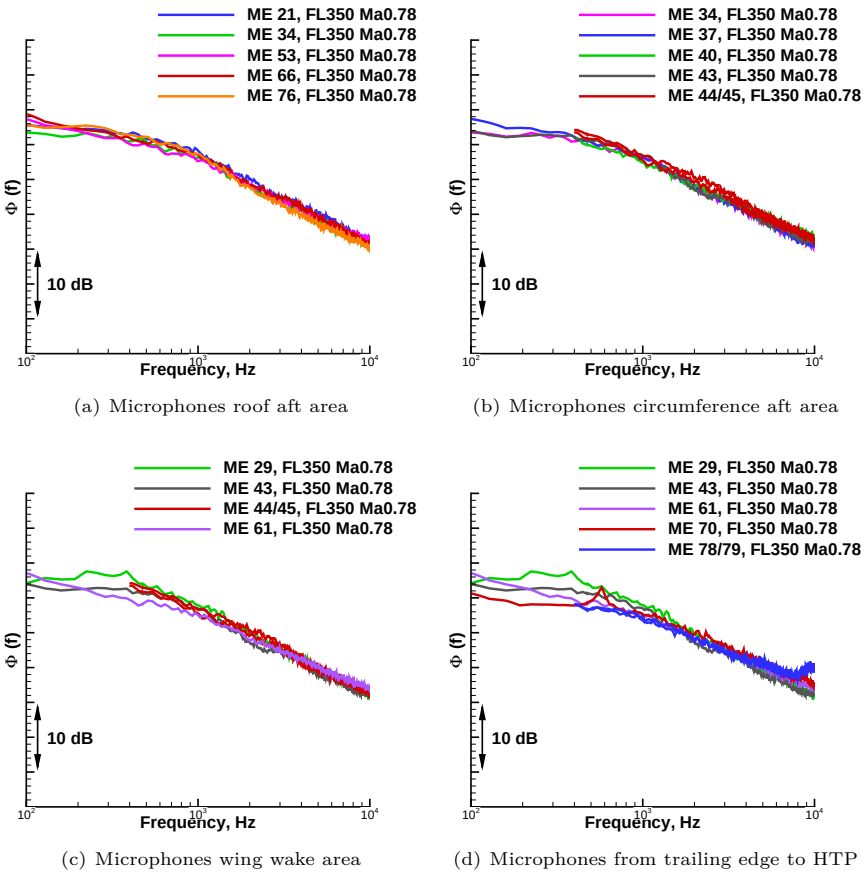

(a) Microphones roof aft area

(b) Microphones circumference aft area

(c) Microphones wing wake area

(d) Microphones from trailing edge to HTP

Figure 2.16: Data comparison aft and wing wake area [58]

a distinct change in the spectra with varying x-value from the nose to the wing's trailing edge (Kulite comparison). However, in the area behind the wing up to the HTP/VTP zone and above the wing wake, no change in spectral shape and level can be seen. Reasons for that were given beforehand on the basis of the development of local boundary layer thickness. Beside this, huge differences in the spectral shape and absolute levels are visible in the area around and directly behind the wing. These differences are mainly triggered by local flow conditions.

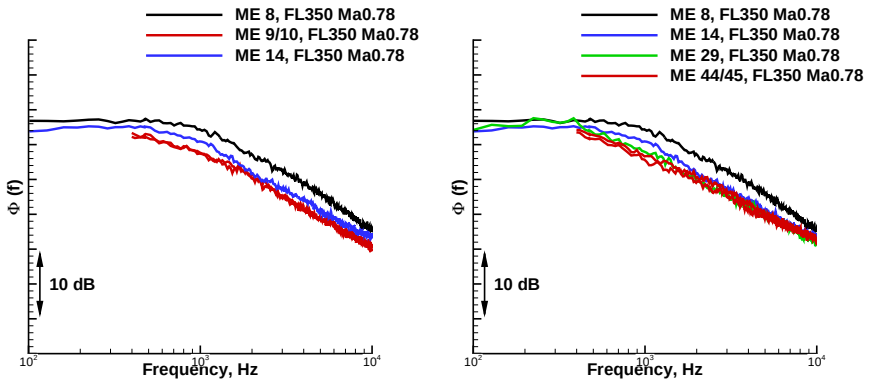

(a) Microphones above trailing edge

(b) Microphones around Belly Fairing

Figure 2.17: Data comparison aft wing area [58]

More details about that are presented in chapter 4.

Varying flight level and Mach number

Figures 2.18 show the influence of Mach number and flight level variation on the auto-spectra using the example of ME15e in the front region. One can see the effect of a varying flight level in Figure 2.18(a) at constant Mach number (Ma = 0.78). The variation in flight level with constant Mach number causes a shift of 2.0 dB and 1.8 dB for the comparison of FL390 with FL350 and FL350 with FL310. Hence, lowering the flight altitude by 4000 ft leads to a broadband noise increase by about 2.0 dB, which can be explained by a higher air density at the lower flight level. These findings correspond to the observed results for measured cabin noise at the same test conditions by Hu [55]. Furthermore, Mach number variation causes a shift in absolute level of 1.8 dB and 1.5 dB for the comparison Ma 0.72 to Ma 0.78 and Ma 0.78 to Ma 0.82, respectively (cf. Figure 2.18(b)).

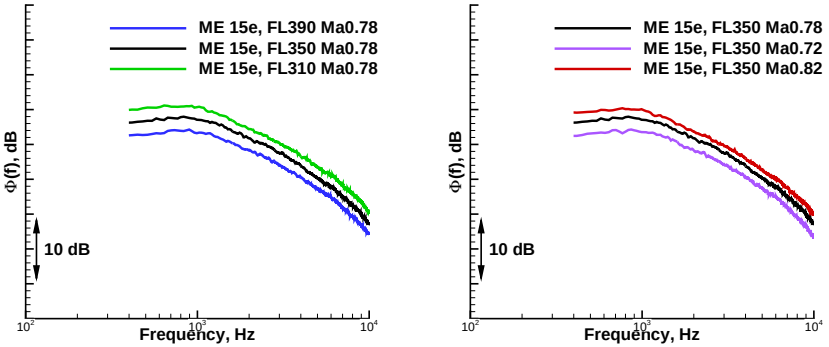

(a) Variation in flight level

(b) Variation in Mach number

Figure 2.18: FL and Mach number variation on the example of front microphone ME15e [58]

3 Fundamentals of Fuselage Excitation by Turbulent Boundary Layer

For the estimation of structural vibration of an aircraft's fuselage, excited by TBL, two types of TBL models are necessary. On the one hand side, the auto-spectrum, that sorts the energy at a single point due to the pressure fluctuations beneath a TBL into frequencies, is required. On the other hand side, a normalised wavenumber-frequency spectrum, that sorts the energy distribution into wavenumbers and gives information about the spacial development of turbulence, is needed.
Chapter 3.1 gives an overview of the multiple development of semi-empirical models, to calculate the TBL wall pressure frequency spectrum. Models, most often found in the last 50 years of literature are provided in a summarised form. Furthermore, chapter 3.2 constitutes this overview for the wavenumber-frequency models. Beside the excitation modelling, a description of the structural coupling is indispensable. The idea of Graham [41] and its application in this thesis is shortly summarised in chapter 3.3.

3.1 Auto-Spectra

Extensive summaries on the field of developing semi-empirical auto-spectra models are prepared by e.g. Hwang [56], whose work is based on observations from Bull [8], Farabee [31], Blake [4, 5] and others. The characterisation of the wall pressure spectra that have formed over the years is summarised and complemented in the following. Figure 3.1 presents the characteristic shape of a TBL wall pressure spectrum (auto-spectrum), which is based on a determination of which scaling variables work best in particular frequency regions. The spectrum is divided into four characteristic regions, with its frequency intervals formulated by dimensionless frequencies:

- Low-frequency region, $\omega\delta/\mathrm{U}_\tau \leq 5$,
- Mid-frequency region, $5 \leq \omega\delta/\mathrm{U}_\tau \leq 100$,
- Overlap region, $100 \leq \omega\delta/\mathrm{U}_\tau \leq 0.3(\mathrm{U}_\tau\delta/\nu)$, exists when Reynolds number $\mathrm{U}_\tau\delta/\nu > 333$,

- High-frequency region, $\omega\nu/\mathrm{U}_\tau^2 \geq 0.3$.

The low- and mid-frequency regions are dominated by structures in the outer layer and either $q = \frac{1}{2}\rho\mathrm{U}_\infty^2$ (dynamic pressure) or τ_w (wall shear stress) may be used as the pressure scale and $\delta^*/\mathrm{U}_\infty$ (δ^* as the boundary layer displacement thickness) as the time scale as well as τ_w as the pressure scale and δ_l/U_τ as the time scale respectively. The distinctive spectral peak occurs roughly at $\omega\delta/\mathrm{U}_\tau \approx 50$ in the mid-frequency region. In the overlap region, both inner- and outer-layer scaling can be used to make the data collapse, which implies a variation of the spectrum as ω^{-1}, but data by Goody [37] and Smol'yakov [77] show variation of the spectrum as $\omega^{-0.7}$ and $\omega^{-1.1}$, respectively. Finally, the high-frequency region is influenced by viscosity and scaled on inner-layer variables, usually with τ_w as the pressure scale and ν/U_τ^2 as the time scale.

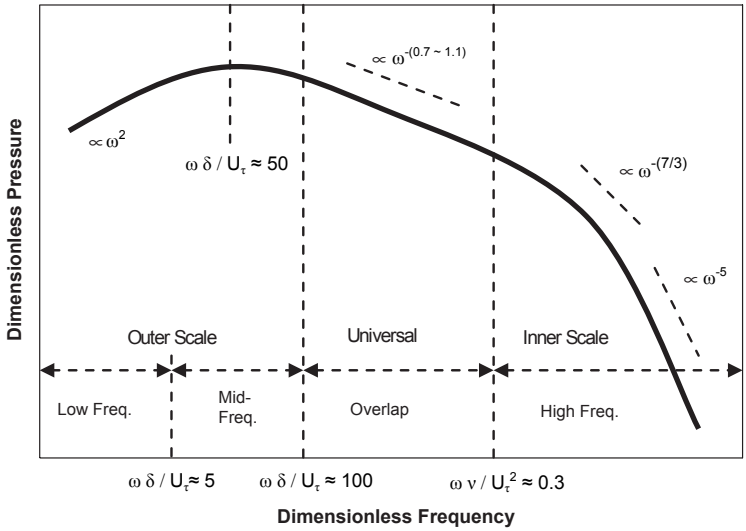

Figure 3.1: General spectral characteristics of a TBL wall pressure spectrum at various frequency regions, according to [56]

The wall pressure spectrum in the low- and mid-frequency regions are composed of pressure fluctuations impressed on the wall by a physical process that occurs largely in the outer layer, away from the wall, while the higher spectral frequencies reflect physical behaviour occurring close to the wall. This duality contributes to

the non-homogeneous nature of the wall pressure [68]. According to HWANG [56], one can conclude the following scaling laws for the respective regions:

- Low: $\Phi(\omega)\frac{U_\infty}{q^2\delta^*} = f(\frac{\omega\delta^*}{U_\infty}) = constant \cdot \left(\frac{\omega\delta^*}{U_\infty}\right)^2$,
- Mid: $\Phi(\omega)\frac{U_\tau}{\tau_w^2\delta} = f(\frac{\omega\delta}{U_\tau})$,
- Overlap: $\omega\Phi(\omega)\tau_w^2 = f = constant$,
- High: $\Phi(\omega)\frac{U_\tau^2}{\tau_w^2\nu} = f(\frac{\omega\nu}{U_\tau^2})$.

These frequency dependent spectral characteristics shows that a suitable model for auto-spectra prediction must be a function of many scaling variables. Solutions for that are presented in the following, based on the work of different researchers.

3.1.1 Robertson (1971)

The model by ROBERTSON [71] is based on the work of LOWSON [63] and constitutes an improvement at low and high Strouhal numbers, published in 1971. ROBERTSON defines the auto-spectrum as follows, by comparing the LOWSON model with other data, and in particular, with measurements at supersonic speeds by NASA-Ames:

$$\Phi(\omega) = \frac{\overline{p'^2}}{\omega_0 \left[1 + \left(\frac{\omega}{\omega_0}\right)^{0.9}\right]^2} \ , \tag{3.1}$$

with the characteristic frequency

$$\omega_0 = 0.5\frac{U_\infty}{\delta^*} \ . \tag{3.2}$$

Where ω is the angular frequency, U_∞ the free stream velocity and δ^* the local boundary layer displacement thickness. Furthermore, the mean square pressure fluctuation is defined as

$$\overline{p'^2} = \left(\frac{0.006\ q}{1.0 + 0.14\mathrm{Ma}_\infty^2}\right)^2 \ . \tag{3.3}$$

This formulation of the mean square pressure fluctuation is introduced by LOWSON [63]. Good agreement of calculated values with experimental results is shown in the Mach number range from Ma = 0.6 up to Ma = 3.0 [71].

3.1.2 Cockburn & Robertson (1974)

For attached turbulent flow, Cockburn & Robertson stated the formula which was previously derived by Robertson (Equ. (3.1)). Cockburn & Robertson conducted tests on a 15° cone-cylinder payload shroud at three Mach numbers ($\mathrm{Ma}_1 = 0.7, \mathrm{Ma}_2 = 0.8, \mathrm{Ma}_3 = 2.0$) [15]. Their presented results were derived for an Atlas-Agena launch vehicle, fitted with a standard payload shroud comprising fiberglass skin and aluminium ring-frame stiffeners. The model is 1.676 m in diameter and 5.791 m long, wherein the cylindrical section has a length of 3.302 m. Rewriting Equ. (3.1) as in the 1974 paper of Cockburn & Robertson yields

$$\Phi(f) = \frac{\overline{p'^2}}{f_0 \left[1 + \left(\frac{f}{f_0}\right)^{0.9}\right]^2} \ . \tag{3.4}$$

At first glance this model seems to be equal to the Robertson model, but Cockburn & Robertson use a modified estimate of the characteristic frequency

$$f_0 = 0.346 \frac{\mathrm{U}_\infty}{\delta_l} \ . \tag{3.5}$$

The estimate of the characteristic frequency used here is based on the local TBL thickness δ_l instead of δ^*. As the mean square pressure fluctuation formulation, Equ. (3.3) is used.

3.1.3 Chase (1980/1987)

According to Hwang [56], the Chase model for the single point wall pressure spectrum is

$$\Phi(\omega) = \frac{\rho^2 \mathrm{U}_\tau^4}{\omega} \left[\frac{\alpha_P \gamma_M}{\alpha_M^3} (1 + \mu_M^2 \alpha_M^2) + \frac{3\pi C_T}{\alpha_T} (1 + \alpha_T^{-2}) \right] \ . \tag{3.6}$$

A first formula for the wavenumber-frequency spectrum was published by Chase in 1980 [12]. Chase improved his model further and published the latest version of the wavenumber-frequency spectrum in 1987 [11], which is the starting point for Equ. (3.6). Equation (3.6) is obtained by integrating the wavenumber-frequency spectrum over the wave vector plane. The constants and variables in Equ. (3.6) are defined as $\alpha_M = \sqrt{1 + \left(\frac{b_C \omega \delta_l}{\mathrm{U_c}}\right)^{-2}}$, $\alpha_T = \sqrt{1 + \left(\frac{b_C \omega \delta_l}{\mathrm{U_c}}\right)^{-2}}$, $C_M = 0.1553$, $C_T = 0.00476$, $b_C = 0.75$, $\mu_M = 0.176$, $\alpha_P = 2\pi(C_M + C_T)$, $\gamma_M = \frac{C_M}{C_M + C_T}$. Furthermore, Chase [11] defined the friction velocity as $\mathrm{U}_\tau = \sqrt{\tau_w / \rho}$. In the

equations for α_M and α_T one parameter is the convective velocity (U_c) of the turbulence in the turbulent boundary layer. According to CHASE [12, 11], it is between $U_c = 0.65 \cdot U_\infty$ and $U_c = 0.75 \cdot U_\infty$. This value can be determined more exactly by using the phase velocity of the cross-spectrum between two sensors aligned with the flow direction. Following that approach, ratios between convective and free stream velocity of about ${}^{U_c}/_{U_\infty} = 0.75...0.80$ were measured frequency dependent for in-flight data of the aircraft, studied in [60].

3.1.4 Efimtsov (1982/1984)

The EFIMTSOV 1 model [20] is dependent on Mach number (Ma), Reynolds number (Re) and Strouhal number (Sh), in this case defined as $Sh = \frac{\omega \delta_l}{U_\tau}$ [20]. The model is based on flight test data in the range of Mach numbers $Ma = 0.41...2.1$, and Reynolds numbers of $Re = 0.5 \cdot 10^8 ... 4.85 \cdot 10^8$. The pressure fluctuations were measured at various positions on an aircraft's fuselage, where the boundary layer was considered fully developed with zero pressure gradient. EFIMTSOV's single point wall pressure spectrum is given by:

$$\Phi(\omega) = \frac{0.01 {\tau_w}^2 \delta_l}{U_\tau \left[1.0 + 0.02 \left(\frac{\omega \delta_l}{U_\tau}\right)^{\frac{2}{3}}\right]} \ . \tag{3.7}$$

The EFIMTSOV 2 model [19] is a further development of the EFIMTSOV 1 model (Equ. (3.7)), using additional data from low and high speed TsAGI (Central Aerohydrodynamic Institute in Moscow, Russia) wind tunnels. The measurements span Mach numbers from $Ma = 0.015...4.0$ and Reynolds numbers from $Re = 6 \cdot 10^2 ... 1.5 \cdot 10^5$ [19]. According to EFIMTSOV [19], the single point wall pressure spectrum model from 1984 is

$$\Phi(\omega) = \frac{\alpha_E U_\tau^3 \rho^2 \delta \beta_E}{\left(1 + 8\alpha_E {}^3 Sh^2\right)^{\frac{1}{3}} + \alpha_E \beta_E Re_\tau \left(\frac{Sh}{Re_\tau}\ , \right)^{\frac{10}{3}}} \ , \tag{3.8}$$

with $Re_\tau = \frac{\delta_l U_\tau}{\nu_w}$, $Re_{\tau 0} = 3000$, $Sh = \frac{\omega \delta_l}{U_\tau}$, $\beta_E = \left[1 + \left(\frac{Re_{\tau 0}}{Re_\tau}\right)^3\right]^{\frac{1}{3}}$, $\alpha_E = 0.01$, $\nu_w = \nu \frac{\rho}{\rho_w} \left(\frac{T_w}{T_\infty}\right)^\gamma$, $\gamma = 0.905$, $T_w = T_\infty \left(1 + r \frac{\kappa - 1}{2} Ma^2\right)$, $r = 0.89$, $\kappa = 1.4$, $\rho_w = \rho \frac{T_\infty}{T w}$.
According to RACKL & WESTON [70], also flight measurements on a TU144 and a Russian twin engined supersonic military aircraft (TU-22) are taken into account for this model. RACKL states that the sensor positions appear to be similar to those used on a TU144 by NASA-Boeing (cf. chapter 3.1.8).

3.1.5 Chase-Howe (1998)

The single point wall pressure spectrum is given by the CHASE - HOWE model [66] as

$$\Phi(\omega) = \frac{2\left(\frac{\delta^*}{\mathrm{U}_\infty}\right)^3 (\tau_w\ \omega)^2}{\left[\left(\frac{\omega\delta^*}{\mathrm{U}_\infty}\right)^2 + 0.0144\right]^{\frac{3}{2}}}\ . \tag{3.9}$$

The CHASE - HOWE model was presented by HOWE [51] and is based on the CHASE model. It is much simpler than the model proposed by CHASE and the first time referred to as the CHASE - HOWE model by GOODY [37].
Compared to the CHASE model, the modified CHASE - HOWE model takes not as many TBL variables into account, which is evidence for the lower degree of complexity of the CHASE - HOWE model.

3.1.6 Smol'yakov (2000)

SMOL'YAKOV proposed a new model using different scaling variables for different frequency regions. He described three regions in the spectrum, a low frequency, an universal and a high frequency region. The model proposed by Smol'yakov is analogue to the three mentioned regions divided in three formulae [77]. The SMOL'YAKOV model is based on a thorough analysis of his theoretical model of the wavenumber-frequency spectrum and a diverse group of data reported in the literature [56].

a) Low frequency region at $\overline{\omega} < \overline{\omega}_0$

$$\Phi(\omega) = 1.49 \cdot 10^{-5} \cdot \mathrm{Re}_\theta^{2.74} \overline{\omega}^2 \left(1 - 0.117 \mathrm{Re}_\theta^{0.44}\ \overline{\omega}^{1/2}\right) \cdot \frac{\tau_w^2 \nu}{\mathrm{U}_\tau^2} \tag{3.10}$$

b) Universal frequency region at $\overline{\omega}_0 < \overline{\omega} < 0.2$

$$\Phi(\omega) = 2.75\ \overline{\omega}^{-1.11} \left(1 - 0.82\ exp\left[-0.51\left(\frac{\overline{\omega}}{\overline{\omega}_0} - 1\right)\right]\right) \cdot \frac{\tau_w^2 \nu}{\mathrm{U}_\tau^2} \tag{3.11}$$

c) High frequency region at $\overline{\omega} > 0.2$

$$\begin{aligned}\Phi(\omega) = &\left(38.9 e^{-8.35\ \overline{\omega}} + 18.6 e^{-3.58\ \overline{\omega}} + 0.31 e^{-2.14\ \overline{\omega}}\right) \\ &\cdot \left(1 - 0.82\ exp\left[-0.51\left(\frac{\overline{\omega}}{\overline{\omega}_0} - 1\right)\right]\right) \cdot \frac{\tau_w^2 \nu}{\mathrm{U}_\tau^2}\end{aligned} \tag{3.12}$$

Equations (3.10) - (3.12) are valid at $\mathrm{Re}_\theta > 10^3$ ($\mathrm{Re} > 5 \cdot 10^5$). Furthermore $\overline{\omega}$ and $\overline{\omega}_0$ are defined by $\overline{\omega} = \omega\ \nu/\mathrm{U}_\tau^2$ respectively $\overline{\omega}_0 = 49.35\mathrm{Re}_\theta^{-0.88}$, these values are dimensionless frequencies.
According to Smol'yakov [77], the first factors in the formulae (Equ. (3.10) - (3.12)) describe the main laws governing the behaviour of the spectra in the low frequency, universal, and high frequency ranges, respectively. The second factor (in parentheses) provide a smooth matching of the levels in the regions between these ranges.
The used momentum Reynolds number Re_θ is defined as

$$\mathrm{Re}_\theta = \frac{\mathrm{U}_\infty \cdot \theta}{\nu}\ , \tag{3.13}$$

with the boundary layer momentum loss thickness θ.

3.1.7 Goody (2004)

The single point wall pressure spectrum of the Goody model [37] is given by

$$\frac{\Phi(\omega)\mathrm{U}_e}{\tau_w^2 \delta_l} = \frac{\mathbf{a}\left(\frac{\omega\delta_l}{\mathrm{U}_e}\right)^{\mathbf{b}}}{\left[\left(\frac{\omega\delta_l}{\mathrm{U}_e}\right)^{\mathbf{c}} + \mathbf{d}\right]^{\mathbf{e}} + \left[(\mathbf{f}\ \mathrm{R}_T^{\mathbf{g}})\left(\frac{\omega\delta_l}{\mathrm{U}_e}\right)\right]^{\mathbf{h}}}\ , \tag{3.14}$$

with $\mathbf{a}$-$\mathbf{h} = 3.0,\ 2.0,\ 0.75,\ 0.5,\ 3.7,\ 1.1,\ -0.57,\ 7.0$ and $\mathrm{R}_T = \frac{\mathrm{U}_\tau^2 \delta_l}{\mathrm{U}_e \nu}$ is the ratio of the outer-layer-to-inner-layer timescale, which can better be seen after rearranging $\left(\mathrm{R}_T = \frac{\delta_l}{\mathrm{U}_e} / \frac{\nu}{\mathrm{U}_\tau^2}\right)$. The Goody model offers a high degree of confidence when extrapolated to flows with a higher Reynolds number and zero pressure gradient [37]. Goody used the Chase - Howe model as a starting point for the development of his model. He reviewed the experimental surface pressure spectra of six research groups in his dissertation [36], that cover a large Reynolds number range: $1.4 \cdot 10^3 < \mathrm{Re}_\theta < 2.34 \cdot 10^4$, $\mathrm{Re}_\theta = \frac{\mathrm{U}_e \theta}{\nu}$. This Reynolds number span is representative for most laboratory flows, that is, wind tunnels and water tunnels ($\mathrm{Re}_\theta \sim 10^3 ... 10^4$). Most practical flows, like the flow over airplanes have a larger momentum Reynolds number ($\mathrm{Re}_\theta \sim 10^5 ... 10^6$) [37].

3.1.8 Rackl & Weston (2005)

Rackl and Westons model is an adjustment of the existing Efimtsov 2 model, they published their modification in 2005 [70]. Comparisons of measured flight test data from a TU 144LL with predictions from the Efimtsov 2 model showed

two characteristics. The first was a broad band spectral peak around Strouhal number of Sh = 0.6, where the Strouhal number is calculated as $\mathrm{Sh} = \frac{2\pi f \delta^*}{\mathrm{U}_\infty}$. As the second, data showed a slightly steeper roll-off at high frequencies (above 1 kHz) than the predicted roll-off. Speculations about the reasons for the observed deviations can be found in reference [70].
Rackl and Weston used two adjustment functions, firstly

$$C_1 \ \exp\left(-\left(\ln(\mathrm{Sh}) - \ln(\mathrm{Sh}_1)\right)^2\right); \ (C_1 = 2.5), \tag{3.15}$$

$\mathrm{Sh}_1 = 0.6$ is the reference value, where the spectral peak in the measurements appeared and secondly with the factor accounting for the steeper roll-off

$$\frac{1}{4}\left(\tanh\left(\log\left(\frac{f}{1000}\right)\right) + 1\right)\left[(\mathrm{Ma} - 1.65)\log(f)\right] . \tag{3.16}$$

In Equ. (3.16), since only the high frequency slope needs adjustment, a tanh-function centered at 1000 Hz is included. The second term in parentheses accounts for the overprediction of the Efimtsov 2 model in the range below Ma = 1.65 and the underprediction for conditions above Ma = 1.65.
Finally it follows

$$\begin{aligned}\Phi(f)_{adjusted} =& \Phi(f)_{predicted} \\ &+ 2.5 \ exp\left(-\left(\ln(\frac{2\pi f \delta^*}{\mathrm{U}_\infty}) - \ln(0.6)\right)^2\right) \\ &+ \frac{1}{4}\left(\tanh\left(\log\left(\frac{f}{1000}\right)\right) + 1\right)\left[(\mathrm{Ma} - 1.65)\log(f)\right] .\end{aligned} \tag{3.17}$$

3.1.9 Model Comparison

In this section, plots with all recently introduced semi-empirical TBL models are presented for FL350 and Ma = 0.78 at front and aft Kulite positions. The models' auto-spectra for the front area are shown in Figures 3.2(a) and 3.2(b). Figures 3.2(c) and 3.2(d) present the models for front and aft region with their respective validation auto-spectra from flight test measurements. All models are calculated with the local flow parameters from CFD calculation.
Figures 3.2(a), 3.2(b) shows that the models can be divided into two major groups. On the one hand the green and blue lines, describing the Robertson / Cockburn & Robertson, respectively the Efimtsov / Rackl & Weston models. These models are based on flight test and wind tunnel data at high Mach- and Reynolds

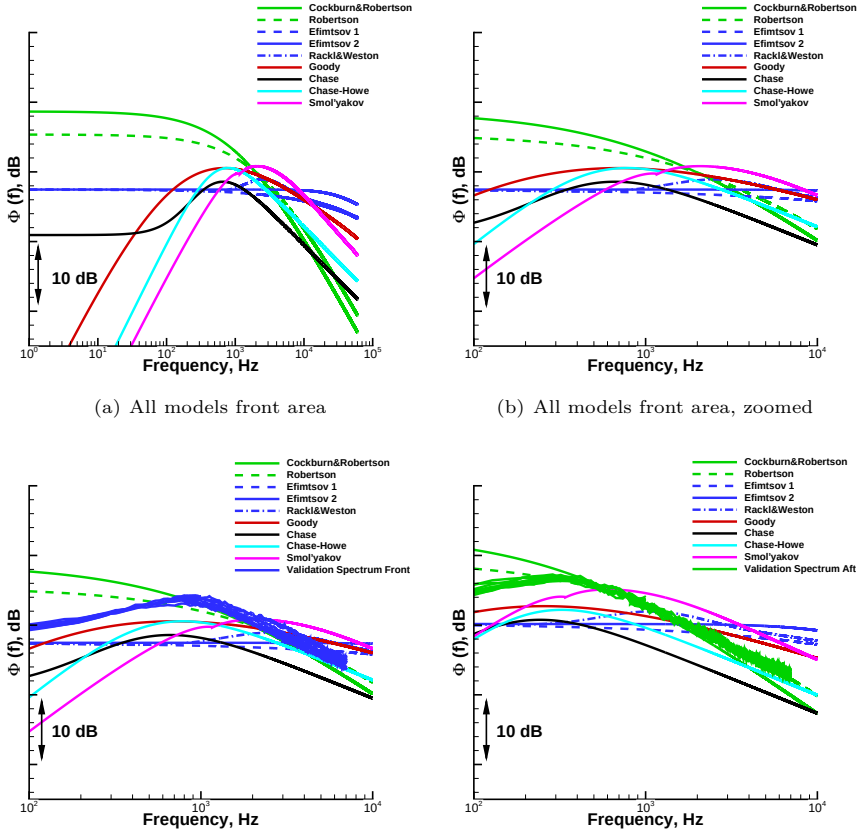

(a) All models front area

(b) All models front area, zoomed

(c) Front models with validation auto-spectra

(d) Aft models with validation auto-spectra

Figure 3.2: Comparison of predictions from all auto-spectra models with validation auto-spectra; Ma = 0.78, FL350, front and aft area [58]

numbers. Distinctive for this models is a large plateau in the low frequency range with a roll-off at higher frequencies.

On the other hand, the Goody, Chase - Howe and Smol'yakov models represent the second group. This group obviously provides spectra with different shapes, especially in the low frequency range. The absolute values of these predictions increase with increasing frequency until a maximum in the mid frequency

range is reached and then it is followed by a decreasing behaviour with increasing frequency.
The CHASE model is with regard to the shape, something in between these two mentioned groups (cf. Figure 3.2(a)). In the low frequency range a large plateau is characteristic, as it is for the ROBERTSON / COCKBURN & ROBERTSON and the EFIMTSOV / RACKL & WESTON models. For higher frequencies the predicted spectrum peaks and afterwards it is characterised by a roll-off similar to the GOODY, CHASE - HOWE and SMOL'YAKOV models. It is remarkable that each model has its own shape and slightly different characteristics. None of the models fits perfectly to the validation auto-spectra measured by DLR and Airbus. It seems as if each of the presented models is adjusted to one set of measurement data with its own drawbacks in the data quality. Therefore, in this thesis special emphasis was on the analysis of the auto-spectra from different sensor systems, to avoid the modelling of artefacts. Furthermore, it is decided to go further with the GOODY model because it is based on different measurement data bases. Beside this, the model family beginning with CHASE's model and being further developed to the GOODY model is closest to the measurement data and to the theoretical shape of an auto-spectrum, presented in Figure 3.1.

3.2 Wavenumber-Spectra

In this chapter, the relationship between auto-spectra, cross-spectra, correlation function and wavenumber-spectra is introduced. Beside this, an overview of existing wavenumber-frequency models for TBL flow is given.
In signal processing, correlation functions are usually applied to time domain data. They are derived from two signals which are observed at a time (or space) lag such that periodically recurring content is filtered and while non recurring contents are eliminated. The purpose of correlation functions is to give a measure of agreement between two signals and therefore to give information about the change of the signal. According to [23], the cross-spectral density function $R(\xi, \eta, \omega)$ can be calculated by making use of the space-time correlation function $G(\xi, \eta, \tau)$, which is defined as the ensemble average ($\langle ... \rangle$) of the wall pressure at two different points or at one point with a time lag

$$G(\xi, \eta, \tau) = \langle p(x, y, t) \cdot p(x + \xi, y + \eta, t + \tau) \rangle \ . \tag{3.18}$$

$\xi,\ \eta$ denote the separation between two points in the x, y-plane. The cross-spectral density is obtained by a Fourier transform of $G(\xi, \eta, \tau)$ with respect to time

$$R(\xi, \eta, \omega) = \frac{1}{2\pi} \int_{-\infty}^{\infty} G(\xi, \eta, \tau) e^{-i\omega\tau} d\tau \ . \tag{3.19}$$

Furthermore, for each frequency (ω), a wavenumber-frequency spectrum ($\Phi(k_x, k_y, \omega)$) can be generated by the spacial Fourier transform of the cross-spectral density $R(\xi, \eta, \omega)$

$$\Phi(k_x, k_y, \omega) = \frac{1}{(2\pi)^2} \int_{-\infty}^{\infty} \int_{-\infty}^{\infty} R(\xi, \eta, \omega) e^{-i(k_x\xi + k_y\eta)} d\eta d\xi \ . \tag{3.20}$$

Integration over k_x and k_y of $\Phi(k_x, k_y, \omega)$ yields the auto-spectrum of the wall pressure fluctuations at that specific frequency

$$\Phi(\omega) = \int_{-\infty}^{\infty} \int_{-\infty}^{\infty} \Phi(k_x, k_y, \omega) dk_x dk_y \ . \tag{3.21}$$

Beside these quantities, a measure for the power decay rate in the streamwise and cross stream direction can be determined from cross correlation analysis, by fitting an exponential distribution to the peaks in the cross correlation, taken from a reference sensor and other sensors ($x,\ i = 1,\ 2,\ 3, ...$)

$$max(G(x, x + \xi_i, t, t + \tau_i)) \cong e^{-\frac{|\xi_i|}{L}} \ . \tag{3.22}$$

The correlation length, L, is determined by the value that produces the best fit over all the correlation peaks [68].
Beside this, often the coherence (γ^2) is referred to, which is a normalised cross-spectrum between two points ($x,\ x+\xi$). It gives a measure of the degree of linear dependence between the two signals as a function of frequency and the range of the resultant values is between 0 and 1. The square root of the coherence is used throughout the thesis and referred to as coherence, for better comparability with the work of Palumbo [67] and Haxter [47]. The coherence between two points within flow direction is equivalent to the cross-spectrum magnitude normalised by the square root of the respective auto-spectra [2]

$$\gamma(x, x + \xi, \omega) = \frac{|R(x, x + \xi, \omega)|}{\sqrt{\Phi(x, \omega)\Phi(x + \xi, \omega)}} \ . \tag{3.23}$$

A value of $\gamma = 1$ denotes perfectly correlated signals and $\gamma = 0$ denotes completely uncorrelated signals. Furthermore the coherence length (L_γ) for a particular frequency is found by fitting an exponential to γ at that frequency

$$\gamma(x, x+\xi, \omega_j) \cong e^{-\frac{|\xi|}{L_{\gamma_j}}} \ , \ j = 1,\ 2,\ 3,\ \ldots \ . \tag{3.24}$$

According to Palumbo [68], the coherence length is a strongly frequency dependent quantity, reaching its maximum at frequencies corresponding to the peak in the auto-spectrum and decreasing rapidly at higher frequencies. At high frequencies, structures in the inner layer dominate the wall pressure behaviour and at low frequencies, structures in the outer layer dominate the wall pressure behaviour. However, cross correlation is a wide band analysis in that its result is a combination of these behaviours over all frequencies. At short distances the short decay lengths of the structures at the higher frequencies causes a rapid fall off in correlated power and at greater distances, the longer decay lengths of the low frequency structures sustain the correlated power. The lack of consistency in the correlation decay processes across the frequency band results in a behaviour that cannot be adequately modeled by a single exponential curve. The terminology in this thesis follows Palumbo's terminology in [68] and therefore the term *correlation length* is used to describe power decay rates, computed using the *cross correlation* and *coherence length* for rates computed using the *cross-spectrum*.
A schematical sketch of the wavenumber-frequency spectrum with all characteristic regions is given in Figure 3.3 at constant frequency. Here, k_x is the wavenumber, corresponding to the flow direction and k_y is the wavenumber corresponding to the cross flow direction. This description can e.g. be found in [5], [8] or [65]. Bull states in [8], that the general shape of the spectrum underneath TBL is driven by pressure-field components with phase velocities $\omega/k = \mathrm{U_c}$. This area is called the convective ridge of the wavenumber-spectrum (centered around $k_\omega = {}^{\omega}/_{\mathrm{U_c}}$), where most of the TBL turbulence energy is located. Furthermore, acoustic radiation is associated with components with phase velocities which are equal or greater than the speed of sound in the fluid. Therefore, detailed knowledge of the whole wavenumber-frequency spectrum is necessary. The spectrum, depicted in Fig. 3.3 is subdivided in: (1) supersonic region (not marked), $k < \omega/c\ (= k_0)$; (2) sonic or acoustic region, $k \simeq \omega/c$; (3) subconvective region, $\omega/c < k < \omega/\mathrm{U_c}$; (4) convective region, centred around $k = \omega/\mathrm{U_c}$; (5) viscous region, $k \gg \omega/\mathrm{U_c}$ [8].
Beside this, Graham [43] supposed that the subconvective region, which is important for underwater applications, is not dominant to aircraft applications. It is the convective region, where most of the energy of the TBL is positioned and is the major driver of exciting structures on aircraft. Finally, the viscous region is that region, where small scale turbulence occurs [65].

The following analysis of different models will show that the convective peak, the area with most of the energy, is much wider in cross flow direction compared to the flow direction, which is an effect of different coherence length in the respective direction.
Furthermore, Smol'yakov states in [78] that all known wavenumber-frequency models can be categorised into two models. The first group contains convertible models, which allow one to pass from the wavenumber-frequency representation of the spectrum to the cross-spectrum and back in an analytical way via Fourier transformation. According to Smol'yakov, the convertibility of the models is convenient for using different methods in calculating both structural vibrations and flow noise. The second group consists of models that do not possess this convenient property. All presented models in the following fulfil the convertibility condition.

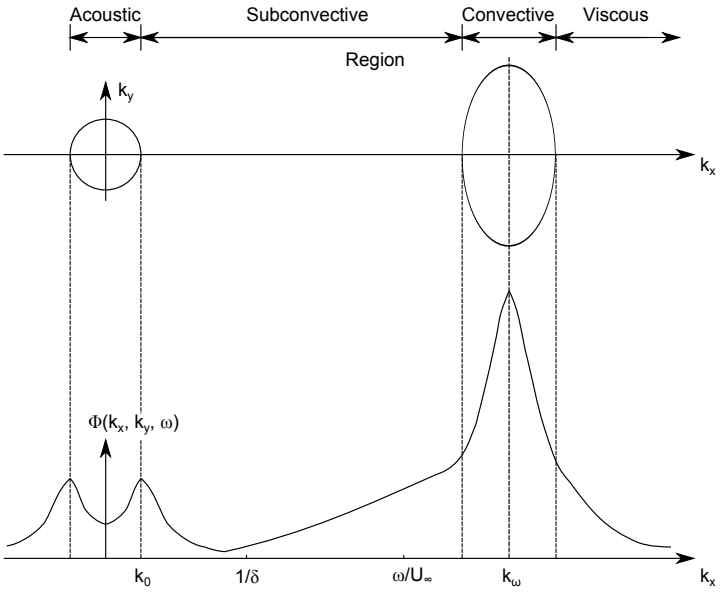

Figure 3.3: Characteristic regions of wavenumber-spectrum; according to Howe [51]

Graham [41, 43] uses the wavenumber-frequency model in a normalised form, to compare the different models among each other. The Graham normalisation

works like

$$\tilde{\Phi}(k_x, k_y, \omega) = \frac{(2\pi)^2\ \omega^2}{\mathrm{U}_c^2\ \Phi(\omega)} \cdot \Phi(k_x, k_y, \omega)\ , \tag{3.25}$$

which is valid when the wavenumber-frequency spectrum fulfills the following requirement

$$\int_{-\infty}^{\infty}\int_{-\infty}^{\infty} \Phi(k_x, k_y, \omega) dk_x dk_y = 1, \text{ on condition, that } \Phi(\omega) = 1. \tag{3.26}$$

Furthermore, the normalised wavenumber-frequency model then satisfies the integral requirement

$$\frac{1}{(2\pi)^2} \int_{-\infty}^{\infty}\int_{-\infty}^{\infty} \tilde{\Phi}(k_x, k_y, \omega) \left(\frac{\mathrm{U_c}}{\omega}\right)^2 dk_x dk_y = 1\ . \tag{3.27}$$

In the following, only models complying with this criterion are presented. The advantage of this description is the ability to combine each normalised wavenumber-frequency spectrum with each auto-spectrum model.

3.2.1 Corcos (1964)

As explained in the beforehand chapter, the wavenumber-frequency spectrum is a Fourier transformed cross-spectral density function $R(\xi, \eta, \omega)$. The Corcos formulation [17] of the pressure fluctuations in the space-frequency domain is given by the exponential function

$$R(\xi, \eta, \omega) = \Phi(\omega) e^{-|\alpha\xi|} e^{-|\beta\eta|} e^{ik_\omega \xi}\ . \tag{3.28}$$

Here, the e-functions denote the correlation function and therefore the streamwise and transversal development of the flow. Furthermore, the convective wavenumber k_ω, which defines the peak in the spectrum, is given by

$$k_\omega = \omega / \mathrm{U_c} \tag{3.29}$$

and ξ as well as η denotes the longitudinal and respectively lateral distance. The Corcos model is not taking the acoustic region, mentioned in Fig. 3.3, into account. Furthermore, the used variables α and β $(= 1/L_\gamma)$ are defined as

$$\alpha = k_\omega \alpha_x = \frac{\omega}{\mathrm{U_c}} \alpha_x \tag{3.30}$$

and

$$\beta = k_\omega \alpha_y = \frac{\omega}{\mathrm{U_c}} \alpha_y \ , \tag{3.31}$$

which are the inverse coherence length

$$L_{\gamma,Corcos} = \frac{1}{\alpha} \vee \frac{1}{\beta} = \frac{\mathrm{U_c}}{\omega\ \alpha_x} \vee \frac{\mathrm{U_c}}{\omega\ \alpha_y}. \tag{3.32}$$

The coefficients α_x and α_y are the decay coefficients in the flow and cross flow direction, respectively. GRAHAM [43] suggested values as $\alpha_x = 0.1$ and $\alpha_y = 0.77$. Other researchers like BLAKE [5] propose values like $\alpha_x = 0.32$ and $\alpha_y = 0.7$ for aircraft boundary layers. In the formulation of the coherence length one of the drawbacks of the model can be seen. In case $\omega \to 0$, the coherence length tends to infinity. However, from experiments it follows that at low frequencies, the coherence length tend to finite values. The finite thickness of the TBL prevents the unlimited growth of coherence length. BLAKE [5] has analysed data and arrived at a conclusion regarding the invalidity of the CORCOS model at low wavenumbers due to the disregard of the finite size of the TBL.
Finally, the CORCOS wavenumber-frequency model is found by Fourier transforming Equ. (3.28) and is given by

$$\Phi(k_x, k_y, \omega) = \frac{\Phi(\omega)}{\pi^2} \cdot \frac{\alpha\beta}{[\alpha^2 + (k_x - k_\omega)^2]\,[\beta^2 + k_y^2]} \ . \tag{3.33}$$

This transformation is in detail described in [65] and [12]. Equation (3.33) can be normalised by the GRAHAM formulation (Equ. 3.25), which yields the GRAHAM normalised CORCOS wavenumber-frequency model

$$\tilde{\Phi}(k_x, k_y, \omega) = \frac{4\alpha_x\alpha_y}{\left[{\alpha_y}^2 + \left(k_y \frac{\mathrm{U_c}}{\omega}\right)^2\right]\left[{\alpha_x}^2 + \left(k_x \frac{\mathrm{U_c}}{\omega} - 1\right)^2\right]} \ . \tag{3.34}$$

A sketch of the CORCOS model for typical cruise flight condition is given in Figures 3.4(a) and 3.4(b) at $f = 2000$ Hz. In Fig. 3.4(b), the classical rhombic shape is visible, caused by the separate consideration of flow and cross flow direction.

3.2.2 Jolly (1968)

JOLLYS model is an improvement of the CORCOS model, presented before. JOLLY extended the model with a formula that takes the limited thickness of the boundary layer into account, what was missing in the CORCOS model. This extension is an

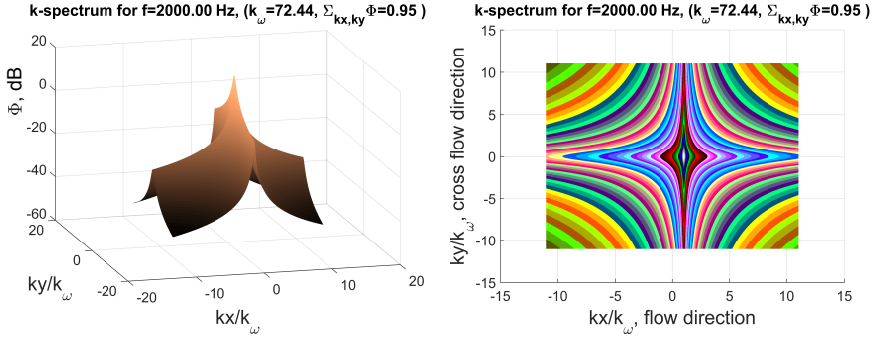

(a) Side view

(b) Top view

Figure 3.4: Corcos wavenumber-frequency model

improvement especially in the low frequency range of the coherence length. In [14], JOLLY proposed the following modification factor

$$\varepsilon_J = \sqrt{1 + (3k_\omega \delta^*)^{-2}} \ . \tag{3.35}$$

Equations (3.30) and (3.31) are multiplied by this factor and finally the following cross-spectral density function results as a modification of Equation (3.28)

$$R(\xi, \eta, \omega) = \Phi(\omega) e^{-\varepsilon_J |\alpha \xi|} e^{-\varepsilon_J |\beta \eta|} e^{i k_\omega \xi} \ . \tag{3.36}$$

Fourier transforming this equation, the wavenumber-frequency model follows as

$$\Phi(k_x, k_y, \omega) = \frac{\Phi(\omega)}{\pi^2} \cdot \frac{\alpha\beta \ \varepsilon_J^2}{\left[\alpha^2 \varepsilon_J^2 + (k_x - k_\omega)^2\right] \left[\beta^2 \varepsilon_J^2 + k_y^2\right]} \ . \tag{3.37}$$

Performing the GRAHAM normalisation yields

$$\tilde{\Phi}(k_x, k_y, \omega) = \frac{4 \alpha_x \alpha_y \varepsilon_J^2}{\left[{\alpha_y}^2 \varepsilon_J^2 + \left(k_y \frac{U_c}{\omega}\right)^2\right] \left[{\alpha_x}^2 \varepsilon_J^2 + \left(k_x \frac{U_c}{\omega} - 1\right)^2\right]} \ . \tag{3.38}$$

A sketch of the JOLLY model for typical cruise flight condition is given in Figure 3.5(a) and 3.5(b) at $f = 2000$ Hz.

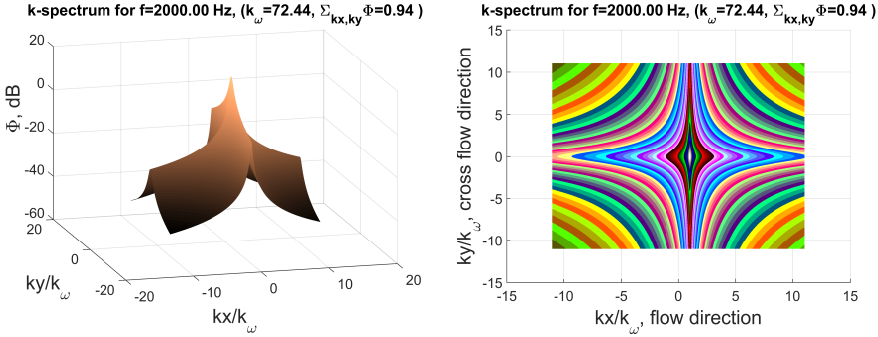

(a) Side view

(b) Top view

Figure 3.5: Jolly wavenumber-frequency model

3.2.3 Efimtsov (1982)

The Efimtsov wavenumber-frequency model [20] follows the same philosophy than the Corcos model and describes the flow- and cross flow direction separately. In contrast to the Corcos model, Efimtsov takes the TBL thickness for the calculation of the coherence length in his model into account. Efimtsov gives an estimate for the flow direction by the empirical expression

$$L_{\gamma,Efimtsov,x} = \Lambda_x = \delta_l \left[\left(\frac{a_1 \mathrm{Sh}}{\mathrm{U_c}/\mathrm{U}_\tau} \right)^2 + \frac{{a_2}^2}{\mathrm{Sh}^2 + (a_2/a_3)^2} \right]^{-1/2} \tag{3.39}$$

and for the cross flow direction by

$$L_{\gamma,Efimtsov,y} = \Lambda_y = \delta_l \left[\left(\frac{a_4 \mathrm{Sh}}{\mathrm{U_c}/\mathrm{U}_\tau} \right)^2 + \frac{{a_5}^2}{\mathrm{Sh}^2 + (a_5/a_6)^2} \right]^{-1/2}, \ \mathrm{Ma}_\infty < 0.75, \tag{3.40}$$

$$L_{\gamma,Efimtsov,y} = \Lambda_y = \delta_l \left[\left(\frac{a_4 \mathrm{Sh}}{\mathrm{U_c}/\mathrm{U}_\tau} \right)^2 + {a_7}^2 \right]^{-1/2}, \ \mathrm{Ma}_\infty > 0.9. \tag{3.41}$$

For flight speeds between Ma 0.75 and Ma 0.9 values have to be interpolated. The Strouhal number is defined as $\mathrm{Sh} = \frac{\omega \delta_l}{\mathrm{U}_\tau}$, here the friction velocity is given by $\mathrm{U}_\tau = \sqrt{\frac{\tau_w}{\rho_w}}$. Efimtsov propose a calculation of these parameters by the

procedures described by Bies in [3]. Furthermore, Efimtsov states a formula for the calculation of the ratio U_c/U_τ in [20]

$$\frac{U_c}{U_\tau} = a_8 \mathrm{Sh}^{1/5} \left[\frac{1 + (a_9 \mathrm{Sh})^2}{1 + (a_{10} \mathrm{Sh})^4} \right]^{1/10} . \tag{3.42}$$

The constants $a_1 - a_{10}$ are, respectively, 0.1, 72.8, 1.54, 0.77, 548, 13.5, 5.66, 9.55, $6.38 \cdot 10^{-4}$, $3.98 \cdot 10^{-3}$.
The wavenumber-frequency model is achieved by replacing α and β in Equation (3.33) by the reciprocal of the Efimtsov coherence lengths, $1/\Lambda_x$ and $1/\Lambda_y$ respectively. This yields

$$\Phi(k_x, k_y, \omega) = \frac{\Phi(\omega)}{\pi^2} \cdot \frac{\frac{1}{\Lambda_x} \cdot \frac{1}{\Lambda_y}}{\left[\left(\frac{1}{\Lambda_x}\right)^2 + (k_x - k_\omega)^2 \right] \left[\left(\frac{1}{\Lambda_y}\right)^2 + {k_y}^2 \right]} . \tag{3.43}$$

To achieve the normalised form of the Efimtsov wavenumber-frequency spectrum, one has to replace α_x and α_y in Equ. (3.34) by $U_c/|\omega|\Lambda_x$ and $U_c/|\omega|\Lambda_y$ respectively. A sketch of the Efimtsov model for typical cruise flight condition is given in Figure 3.6(a) and 3.6(b) at $f = 2000$ Hz.

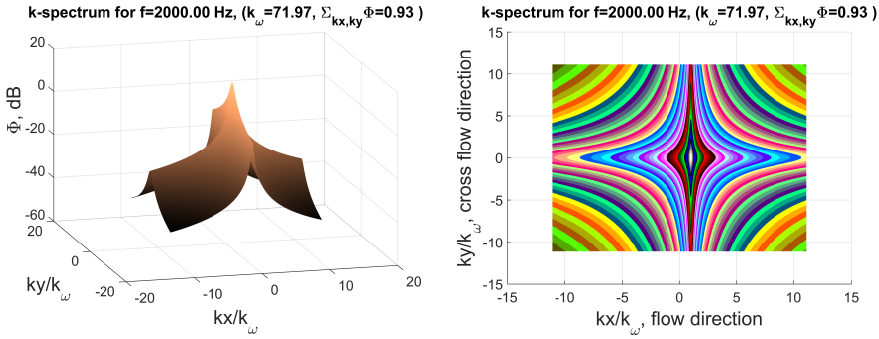

(a) Side view

(b) Top view

Figure 3.6: Efimtsov wavenumber-frequency model

3.2.4 Smol'yakov and Tkachenko (1991)

Smol'yakov and Tkachenko [79] measured spatial pressure correlations of wall pressure fluctuations in gradient-free TBL as a function of spatial separation and boundary layer thickness and fitted exponential curves to their results. Therefore, it is formulated like the Corcos model, on the basis of an approximation of the results of measurements and in a certain sense is a generalisation of the Corcos model. The proposed model includes analytical expressions for the wavenumber-frequency spectrum as well as for the cross-spectrum. Their measurements were conducted in a closed section of a wind tunnel at $\mathrm{U}_\infty = 40\ {}^{\mathrm{m}}/_{\mathrm{s}}$.
The expression, Smol'yakov and Tkachenko finally proposed for the calculation of the wavenumber-frequency spectrum is

$$\Phi(k_x, k_y, \omega) = A(\omega)\ \frac{\Phi(\omega)}{2\pi\ m_0} \left(\frac{\mathrm{U_c}}{\omega}\right)^2 h(\omega)\left[F(k_x, k_y, \omega) - \Delta F(k_x, k_y, \omega)\right]\ . \quad (3.44)$$

Applying the Graham normalisation factor on Equ. (3.44), yields

$$\tilde{\Phi}(k_x, k_y, \omega) = A(\omega)\ \frac{2\pi}{m_0} h(\omega)\left[F(k_x, k_y, \omega) - \Delta F(k_x, k_y, \omega)\right]\ . \quad (3.45)$$

All used functions in Equation (3.44) are given in the following,

$$F(k_x, k_y, \omega) = \left[A^2(\omega) + \left(1 - \frac{k_x \mathrm{U_c}}{\omega}\right)^2 + \left(\frac{k_y \mathrm{U_c}}{m_0\ \omega}\right)^2\right]^{-3/2}\ . \quad (3.46)$$

The resulting low levels at low wavenumbers are an improvement on the Corcos prediction, but are still higher than experimental values, so that a correction was added to the model to bring it into agreement without significantly affecting the convective peak levels. This correction repeats the structure of $F(k_x, k_y, \omega)$ (Equ. (3.46)) and yields

$$\Delta F(k_x, k_y, \omega) = \frac{1}{n}\left[1 + A^2(\omega) + \frac{n}{m_1}\left[\left(m_1 - \frac{k_x \mathrm{U_c}}{\omega}\right)^2 + \left(\frac{k_y \mathrm{U_c}}{\omega}\right)^2 - m_1^2\right]\right]^{-3/2}, \quad (3.47)$$

with a function $h(\omega)$ that is used to balance the energy after introducing the correction term $\Delta F(k_x, k_y, \omega)$,

$$h(\omega) = \left[1 - \frac{m_1\ A(\omega)}{m_0\ n^2\sqrt{G}}\right]^{-1}\ . \quad (3.48)$$

Here A is defined as

$$A(\omega) = 0.124\ \sqrt{1 - \frac{0.2 \cdot \mathrm{U}_\infty}{\omega\delta^*} + \left(\frac{0.2 \cdot \mathrm{U}_\infty}{\omega\delta^*}\right)^2}\ . \quad (3.49)$$

Formulae (3.46) - (3.49) can be calculated with the variables $m_0 = 6.452$, $n = 1.005$ and a function for m_1 and G_1

$$m_1 = \frac{1 + A^2}{5n - 4 + A^2} \ , \ G = 1 + A^2(\omega) - nm_1 \ . \tag{3.50}$$

This model is like all other beforehand mentioned models only valid in the range $k > k_0$ ($k_0 = \omega/c_0$), cf. Figure 3.3. A sketch of the Smol'yakov and Tkachenko model for typical cruise flight condition is given in Figure 3.7(a) and 3.7(b) at $f = 2000$ Hz. The characteristic shape of the model is different, compared with the beforehand presented models. It is the first model reproducing the convective ridge in an quasi-elliptical shape instead of rhombic, which is more realistic and observed in measurements.

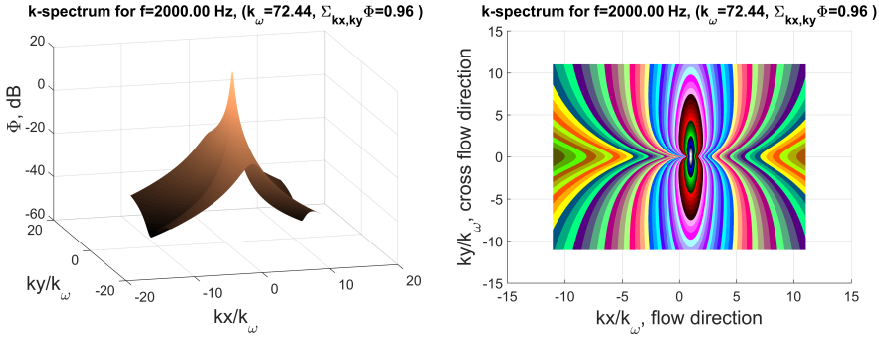

(a) Side view

(b) Top view

Figure 3.7: Smol'yakov and Tkachenko wavenumber-frequency model

3.2.5 Smol'yakov (2006)

Smol'yakov proposed a new model for wavenumber-frequency spectra calculation in [78]. This model, in contrast to all other before mentioned models, takes the viscosity of the fluid into account and therefore depends on Reynolds number. Without taking this effect into account, like in the Corcos model, the coherence length (Equ. (3.32)) decreases to 0 with increasing frequency. This is, according to Smol'yakov, not physical because the minimum vortex size is limited due to viscous forces. In isotropic turbulence for instance, the smallest vortices have the

size that is denoted by the KOLMOGOROV scale $\lambda = (\nu^3/\varepsilon)^{1/4}$, where ε is the dissipation rate of the kinetic energy of the flow. This is a rough estimate because the turbulence of a boundary layer is not isotropic [78].
The SMOL'YAKOV model is an extension of the previous model by SMOL'YAKOV & TKACHENKO, Equ. (3.44). Differences to the previous model are listed in the following:

a) An auto-spectrum, explicitly dependent on viscosity is used. Therefore, the model from SMOL'YAKOV [77] is proposed to be used.
b) The ratio of the convective velocity to the free stream velocity ($\mathrm{U_c}/\mathrm{U}_\infty$) is assumed to be non-constant, and the dependence on dimensionless frequency $\omega\delta^*/\mathrm{U}_\infty$ is taken into account.
c) Model is expressed in terms of coherence length L_γ, as calculated in Equ. (3.32).
d) Model takes the dependence of the cross-spectra on viscosity through the parameter S_m in Equ. (3.54) into account. SMOL'YAKOV says that possible variations of the parameter S_m lies within 70...150 with the most probable value $S_m = 100$.

The final analytical expression of the SMOL'YAKOV wavenumber-frequency model is given as

$$\begin{aligned}\Phi(k_x, k_y, \omega) = \frac{\Phi(\omega)}{2\pi} \Bigg[& \frac{h\Lambda_x\Lambda_y}{(1 + (\Lambda_x\omega/\mathrm{U_c} - \Lambda_x k_x)^2 + (\Lambda_y k_y)^2)^{3/2}} \\ & - \frac{(h-1)l^2}{(1 + (l\ m_1\ \omega/\mathrm{U_c} - l k_x)^2 + (l k_y)^2)^{3/2}} \Bigg] \ ,\end{aligned} \tag{3.51}$$

which is the Fourier transformed cross-spectrum

$$R(\xi, \eta, \omega) = \Phi(\omega) \left[h\gamma \exp(i\xi\omega/\mathrm{U_c}) - (h-1)\Delta\gamma \exp(i m_1 \xi\omega/\mathrm{U_c}) \right] \ . \tag{3.52}$$

The cross-spectrum model is described by the following set of analytical equations:

$$\begin{aligned}\gamma &= \exp\left[- \left((\xi/\Lambda_x)^2 + (\eta/\Lambda_y)^2 \right)^{1/2} \right] \ , \\ \Delta\gamma &= \exp\left[- \left((\xi/l)^2 + (\eta/l)^2 \right)^{1/2} \right] \ , \\ \Lambda_x &= \frac{\mathrm{U_c}}{B\omega} \ , \ \Lambda_y = \frac{\mathrm{U_c}}{m_0 B\omega} \ , \ l = \frac{\mathrm{U_c}}{\omega} \left[\frac{n}{m_1 G} \right]^{1/2} \ , \\ m_1 &= \frac{1 + B^2}{5n - 4 + B^2} \ , \ G = 1 + B^2 - n m_1 \ , \\ h &= \left[1 - \frac{m_1 B}{m_0 n^2 G^{1/2}} \right]^{-1} \ , m_0 = 6.45 \ , n = 1.005 \ ,\end{aligned} \tag{3.53}$$

here m_0 characterises the ratio of the transverse and longitudinal damping decrements in the CORCOS model. Furthermore function B acts as a damping decrement, but frequency dependent in this case and not frequency fix like it is in the CORCOS model

$$B(\omega) = \frac{A}{1 + SA(\omega\nu/\mathrm{U}_\tau^2)(\mathrm{U}_\tau/\mathrm{U}_\infty)(\mathrm{U}_\infty/\mathrm{U}_\mathrm{c})} \ , \tag{3.54}$$

$$A(\omega) = 0.124 \left(1 - \frac{0.25\mathrm{U}_\mathrm{c}}{\omega\delta^*} + \left(\frac{0.25\mathrm{U}_\mathrm{c}}{\omega\delta^*}\right)^2\right)^{1/2} \ , \tag{3.55}$$

$$\frac{\mathrm{U}_\mathrm{c}}{\mathrm{U}_\infty} = 1.6\frac{\omega\delta^*/\mathrm{U}_\infty}{1 + 16(\omega\delta^*/\mathrm{U}_\infty)^2} + 0.6 \ . \tag{3.56}$$

With the GRAHAM normalisation factor it follows for Equ. (3.51)

$$\begin{aligned}\tilde{\Phi}(k_x, k_y, \omega) = 2\pi k_\omega \Bigg[&\frac{h\Lambda_x\Lambda_y}{(1 + (\Lambda_x\omega/\mathrm{U}_\mathrm{c} - \Lambda_x k_x)^2 + (\Lambda_y k_y)^2)^{3/2}} \\ &- \frac{(h-1)l^2}{(1 + (l\ m_1\ \omega/\mathrm{U}_\mathrm{c} - lk_x)^2 + (lk_y)^2)^{3/2}}\Bigg] \ .\end{aligned} \tag{3.57}$$

The cross-spectrum is calculated in a similar way as it is done in the SMOL'YAKOV & TKACHENKO model (cf. chapter 3.2.4). It is again the difference of two terms, the first term constructed on basis of cross-spectrum measurement results and the second term as a small correction for the first one. According to SMOL'YAKOV, the correction term was introduced to provide agreement of the model with wavenumber-frequency spectra measurements.
Furthermore, the before mentioned multiplication hypothesis is modified in this model, as it is also done in the SMOL'YAKOV & TKACHENKO model (cf. chapter 3.2.4). The CORCOS model achieves equal-level lines $|\Phi(\xi, \eta, \omega)| = const$ in a rhombic shape, which is unrealistic, in SMOL'YAKOV this is replaced by an elliptical window concept, which is developed by SCHEWE in [74]. A sketch of the SMOL'YAKOV model for typical cruise flight condition is given in figure 3.8(a) and 3.8(b) at $f = 2000$ Hz.

3.2.6 Chase (1980/1987)

CHASE developed and presented two models for the wavenumber-frequency spectrum. The first model is shown in [12] and the second in [11]. It is noticeable in

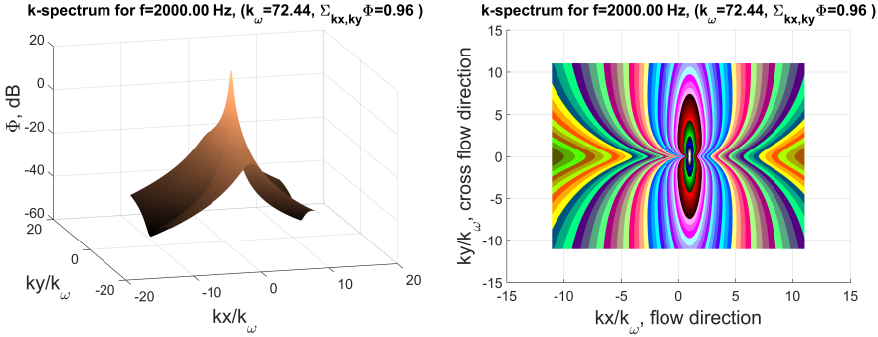

(a) Side view (b) Top view

Figure 3.8: Smol'yakov wavenumber-frequency model

the first model that it has a discontinuity at $k_x = k_y = 0$ which lowers the levels in the acoustic domain. The expression of the model is given like,

$$\Phi(k_x, k_y, \omega) = \rho^2 \mathrm{U}_\tau^3 \left[c_M k_x^2 \mathbf{k}_M^{-5} + c_T |\mathbf{k}|^2 \mathbf{k}_T^{-5} \right] \ , \tag{3.58}$$

with

$$\mathbf{k}_i^2 = \frac{(\omega - \mathrm{U_c} k_x)^2}{h_{Ch}^2 \mathrm{U}_\tau^2} + |\mathbf{k}|^2 + (b_i \delta)^{-2} \ , \ i = M, \ T \ , \tag{3.59}$$

where the coefficients are defined as $c_M = 0.0745$, $c_T = 0.0475$, $b_M = 0.756$, $b_T = 0.378$ and $h_{Ch} = 3.0$. $\mathbf{k}$ is the wavevector in plane of the wall, including k_x and k_y, like $|\mathbf{k}|^2 = k_x^2 + k_y^2$.
Applying the Graham normalisation to the model it follows

$$\tilde{\Phi}(k_x, k_y, \omega) = \frac{(2\pi)^2 \rho^2 \mathrm{U}_\tau^3 \omega^2}{\mathrm{U}_c^2 \Phi(\omega)} \left[c_M k_x^2 \mathbf{k}_M^{-5} + c_T |\mathbf{k}|^2 \mathbf{k}_T^{-5} \right] \ . \tag{3.60}$$

Where Chase defines the auto-spectrum as

$$\frac{\Phi(\omega)}{2\pi} = \frac{2\pi h_{Ch} \rho^2 \mathrm{U}_\tau^4}{3\omega(1 + \mu_{Ch}^2)} (c_M F_M + c_T F_T) \ , \tag{3.61}$$

where the coefficients are denoted as

$$F_M = \left[1 + \mu_{Ch}^2 \alpha_M^2 + \mu_{Ch}^4 (\alpha_M^2 - 1) \right] / \left[\alpha_M^2 + \mu_{Ch}^2 (\alpha_M^2 - 1) \right]^{3/2} \ , \tag{3.62}$$

$$F_T = \left[1 + \alpha_T^2 + \mu_{Ch}^2 (3\alpha_T^2 - 1) + 2\mu_{Ch}^4 (\alpha_T^2 - 1) \right] / \left[\alpha_T^2 + \mu_{Ch}^2 (\alpha_T^2 - 1) \right]^{3/2} \ , \tag{3.63}$$

$$\alpha_i^2 = 1 + \left(\frac{\mathrm{U_c}}{b_i \omega \delta}\right)^2 \ , \mu_{Ch} = \frac{h_{Ch} \mathrm{U}_\tau}{\mathrm{U_c}} \ , i = M,\ T \ . \tag{3.64}$$

A sketch of the CHASE 1 model for typical cruise flight condition is given in Figure 3.9(a) and 3.9(b) at $f = 2000$ Hz. According to the work of GRAHAM [43],

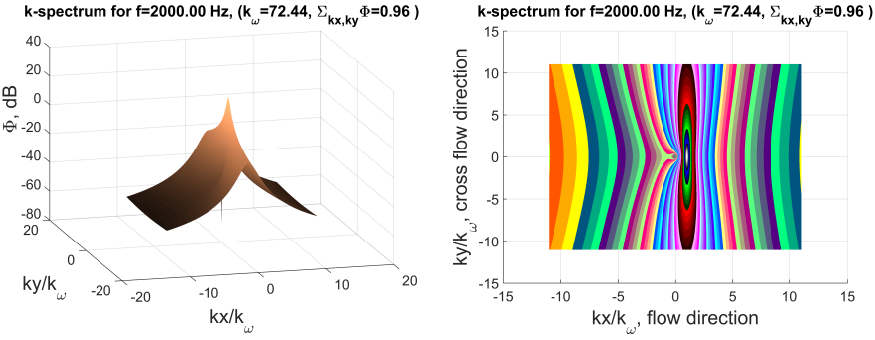

(a) Side view (b) Top view

Figure 3.9: Chase 1 wavenumber-frequency model

the Chase 1 model suffers from two deficiencies: it does not take account of the supersonic region ($|k_x| < \omega/c_0$) and it is not able to reproduce the characteristics of experimental observations in the low wavenumber region ($\omega/c_0 < k_x \ll \omega/\mathrm{U_c}$) [5]. CHASE started an attempt to eliminate these problems and relaxed the requirement for a low wavenumber dependence $\sim |\mathbf{k}|^2$ (Kraichnan-Phillips theorem) and included terms describing the acoustic region. The CHASE 2 model is defined by

$$\Phi(k_x, k_y, \omega) = \rho^2 \mathrm{U}_\tau^3 \mathbf{k}_i^{-5} \left[c_M k_x^2 + \frac{c_T |\mathbf{k}|^2 \mathbf{k}_i^{-5}}{|\mathbf{k}|^2 + (b_i \delta)^{-2}} \right] \ . \tag{3.65}$$

When applying the normalisation of GRAHAM, it follows

$$\tilde{\Phi}(k_x, k_y, \omega) = \frac{(2\pi)^3 \rho^2 \mathrm{U}_\tau^3 \omega^2 \mathbf{k}_i^{-5}}{\mathrm{U_c^2} \Phi(\omega)} \left[c_M k_x^2 + c_T |\mathbf{k}|^2 \frac{\mathbf{k}_i^2}{|\mathbf{k}|^2 + (b_i \delta)^{-2}} \right] \ , \tag{3.66}$$

here, in comparison to the CHASE 1 model, the definition of F_T is changed to

$$F_T = \frac{3}{2}(1 + \mu_{Ch}^2)(1 + \alpha^2)/\alpha^3 \ , \tag{3.67}$$

with $h = 3.0$, $C_M = 0,15533$, $C_T = 0.00466$ and $b_i = 0.75$. A sketch of the CHASE 2 model for typical cruise flight condition is given in Figure 3.10(a) and 3.10(b)

at $f = 2000$ Hz. Here, the typical shape of the CHASE models is retained, with a singularity at $k_x = k_y = 0$. However, the convective ridge seems to be expanded in x-direction, compared with the first CHASE model.

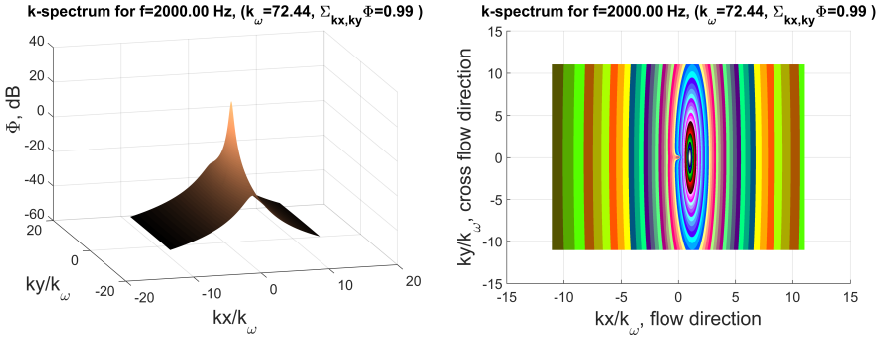

(a) Side view

(b) Top view

Figure 3.10: Chase 2 wavenumber-frequency model

3.2.7 Model Comparison

Figures 3.11(a), 3.11(b) give a comparison of the shape of the different models. The comparison is done at $k_x = k_\omega$ and $k_y = 0$ respectively, to show the convective ridge, where most of the energy is located. As can be seen in the plots, all models are strongly peaked at $k_x = \frac{\omega}{U_c}$, $k_y = 0$. If the boundary layer were a perfectly frozen eddy pattern convecting at speed U_c, all of the energy would be concentrated here [43]. The models can be split up in two major groups, the first contains the model family around the CORCOS model, where the JOLLY and EFIMTSOV models belong to. Both models are developed, based on the Corcos model and its basic concept of separation of flow and cross flow direction. Beside this, the second group contains the CHASE and SMOL'YAKOV models, which are more advanced models that try to better implement the wavenumber regions away from the convective ridge. These models are calculated by taking combined values for the wavenumbers in flow and cross flow direction. Therefore, they are ending up with the more elliptical shape, which is closer to reality. Differences of more than 7 dB are visible in the peak region and with increasing distance to the convective ridge, the differences are increasing up to more than 30 dB. Far away

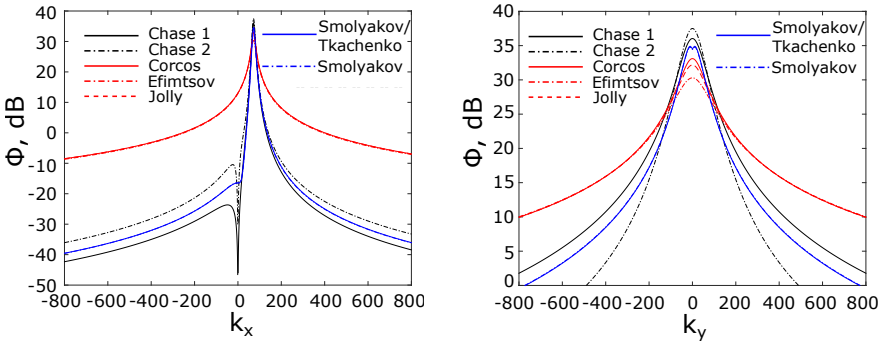

(a) Wavenumber frequency spectra, side view at $k_y = 0$

(b) Wavenumber frequency spectra, side view at $k_x = k_\omega$

Figure 3.11: Comparison of wavenumber-frequency spectra models

from the convective ridge, the elliptical models are more realistic than the rhombic models. Nevertheless, the convective ridge region and its closest surrounding is the most important for aircraft applications.

3.3 TBL - Fuselage Interaction, Graham's Method

For the calculation of the structural vibration of an e.g. aircraft's fuselage, a description of the coupling between TBL and structure is indispensable. Therefore, the method of Graham (cf. [39], [41], [42] and [43]) is chosen and the basic idea is reviewed shortly in this chapter as well as the application for simple test cases is presented. In detail, the example of a simply supported flat plate (plate is clamped to a stiff frame on all edges), fluid-loaded by a random pressure field, is chosen. Graham's idea of an excited plate by a TBL is presented in Figure 3.12. The thin elastic plate is of length a, width b, mass per unit area $M = \frac{m}{A}$, membrane tension N_x, N_y and bending stiffness $B = \frac{E\mathrm{t}^3}{12(1-\nu_p^2)}$ (with Young's modulus E, Poisson's ratio ν_p and thickness t) is excited by TBL and radiates acoustic power into the bounding fluid.
In the first model, presented by Graham in [39], the surrounding is an infinite rigid baffle, and backing it is a vacuum. In [41], Graham extended his model and substituted the vacuum by a bounded fluid. The external and internal fluids have density and speed of sound (ρ_0, c_0) and (ρ_1, c_1) respectively. According to [41], the

plate vibration induced by the turbulent boundary layer pressures will itself alter those pressures, and this back-reaction must be accounted for. Due to the fact that a formally exact approach would use the Lighthill stress tensor to describe the TBL sources, however, the exact form of the tensor is unknown and therefore this method cannot be used for the numerical prediction. Instead, GRAHAM proposed a method where the external pressures are considered as consisting of the "blocked" turbulent boundary layer pressures found on a rigid wall plus the acoustic pressures caused by the plate motion, which is called the weak coupling assumption. This approximation is valid as long as the acoustic velocities are much smaller than the turbulence velocities [41]. According to GRAHAM, the coupled fluid-plate response may then be found by expanding the plate displacement in terms of its modes of vibration in vacuo and solving for the modal velocities. Only the main equations

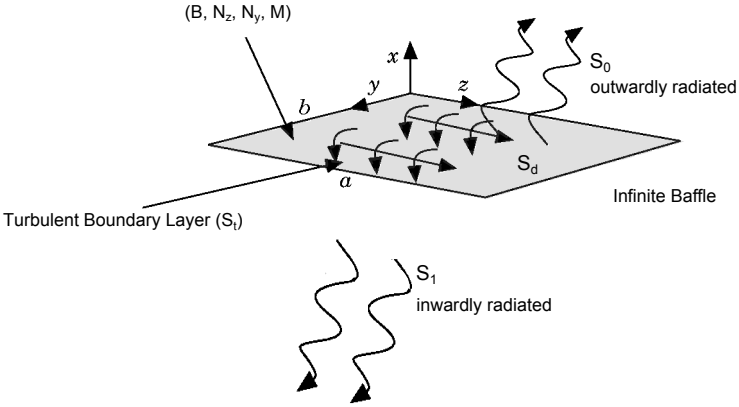

Figure 3.12: Graham's flat plate model [41]

of the methods are presented in the following. The objective which is pursued in this work is, to calculate the vibrational power of a structure, excited by a turbulent boundary layer. Assuming bounded fluids on both sides of the plate [41], the power balance equation yields

$$S_t(\omega) = S_0(\omega) + S_1(\omega) + S_d(\omega) \ , \tag{3.68}$$

with

- $S_t(\omega)$ as the vibrational power, excited by the turbulent boundary layer,
- $S_0(\omega)$ as the outwardly radiated power,

- $S_1(\omega)$ as the inwardly radiated power,
- $S_d(\omega)$ as the structurally dissipated power spectra.

The power spectra $S_i(\omega)$ are defined as modal sums, performing the following integration

$$S_i(\omega) = \sum_{m,n} S_{imn}(\omega),\ i = 0, 1, t, d\ , \tag{3.69}$$

where S_{imn} is the spectrum of the e.g. radiation from mode (m, n). The vibrational power of the plate can now be calculated as stated in Equ. (3.68), by summation of the various power spectra. Writing this equation dependent on the modal excitation term Φ_{mn} and the dimensionless impedance d_{mn}, this yields

$$S_t(\omega) = \frac{1}{\omega_{tbl}} \sum_{m,n} \mathrm{Re}(d_{mn}) \frac{\Phi_{mn}}{|d_{mn}|^2}\ , \tag{3.70}$$

with ω_{tbl} standing for the TBL spectra frequencies supposed to be the excitation. The dimensionless impedance for each eigenmode (mn) is calculated by Graham as

$$d_{mn} = i \left[\frac{B_r(k_m^2 + k_n^2)^2 + N_{zr}k_m^2 + N_{yr}k_n^2}{M\omega^2}(1 - i\varepsilon_s) - 1 \right] + \varepsilon_{f0} Z^{0f}_{mnmn} + \varepsilon_{f1} Z^{1f}_{mnmn}\ , \tag{3.71}$$

with the restoring force terms of the plate's bending stiffness (B_r) and tensions $(N_{yr},\ N_{zr})$. Beside this, ε_s is the structural damping factor. Taking Equ. (3.71) and following the mathematical approach from [7], the equation is simplified and it yields

$$d_{mn} = i \left[\frac{\omega_{EV}^2}{\omega_{tbl}^2}(1 - i\varepsilon_s) - 1 \right] + \frac{\rho_0 c_0}{\omega_{tbl}} Z^{0f}_{mnmn} + \frac{\rho_1 c_1}{\omega_{tbl}} Z^{1f}_{mnmn}\ , \tag{3.72}$$

with ω_{EV} representing the frequency of the plate's eigenvector. A distinct number of frequencies is used to represent the excitation. Beside this, the modal excitation term is defined as follows

$$\Phi_{mn} = \frac{1}{(2\pi)^2} \int_{-\infty}^{\infty} \int_{-\infty}^{\infty} \Phi(k_y, k_z, \omega_{tbl}) |S_{mn}(k_y, k_z)|^2 dk_y dk_z\ . \tag{3.73}$$

$\Phi(k_y, k_z, \omega_{tbl})$ is the wavenumber-frequency TBL model, which were introduced in chapter 3.2, including the auto-spectra as well as the correlation behaviour of

the TBL. Here, S_{mn} is the spatial Fourier transform of the mass normalised mode shape Ψ^M_{mn}

$$S_{mn}(k_y, k_z) = \int_0^a \int_0^b \Psi^M_{mn}(y, z) e^{-ik_y y} e^{-ik_z z} dy dz \ . \tag{3.74}$$

Taking $|S_{mn}(k_y, k_z)|^2$ one achieves the panel acceptance, which is used for the calculation of the modal excitation term (Equ. (3.73)). Wherein Ψ^M_{mn} denotes the in vacuo (m, n) mode shape (mass normalised) for the simply supported flat plate, the formula of the non-normalised mode shape is

$$\Psi_{mn}(y, z) = \frac{2}{\sqrt{(ab)}} sin\,(k_m z)\, sin\,(k_n y) \ , \text{ with} \tag{3.75}$$

$$k_m = \frac{m\pi}{a} \text{ and } k_n = \frac{n\pi}{b} \ . \tag{3.76}$$

Here, m and n denote the number of half waves in flow and cross flow direction of the plate's eigenmode under investigation. In summary, with this set of formulae one can calculate the power spectrum of a simply supported plate with homogeneous mass distribution. Inhomogeneities from e.g. frames and stringers will lead to coupling between the modes and this claims an expansion of the given set of formulae. As denoted in Equation 3.74, the eigenmode is used in a mass-normalised way, to take the plate's mass into account. According to [28], the modal model of a flat plate with equal mass distribution possesses important properties, the orthogonality properties which are concisely stated in matrix syntax ([...]) as

$$[\Psi]^T [M][\Psi] = [m] \ , \tag{3.77}$$

$$[\Psi]^T [K][\Psi] = [k] \ , \tag{3.78}$$

where $[m]$ and $[k]$ are referred to as the modal mass and modal stiffness diagonal matrices of the plate's eigenmodes. $[M]$ as well as $[K]$ are the physical mass and stiffness matrices of the plate. Besides, $[\Psi]$ includes all eigenvectors of the plate. The mass normalised eigenvectors $[\Psi^M]$ are calculated as

$$[\Psi^M] = [\Psi][m^{-1/2}] \tag{3.79}$$

by making use of Equ. (3.77), where the modal mass $[m]$ of each eigenmode is allocated. Consecutively, the mass-normalised eigenvector matrix satisfies the following condition

$$[\Psi^M_{mn}]^T [M][\Psi^M_{mn}] = [I] \ , \tag{3.80}$$

with the identity matrix $[I]$.
The beforehand discussed method is used to calculate the plate response, generated by different excitations from various combinations of auto-spectra and

wavenumber-frequency spectra models (cf. chapter 3.1 and 3.2). Results of this study are presented in chapter 6.2.

4 CFD Calculations and Analysis

For the prediction of the beforehand introduced auto-spectra and wavenumber-frequency spectra models, aerodynamic input is necessary. Usually, this input is calculated by theoretical formulae, whose validity is limited by drastic simplifications, when applied to a whole aircraft. Furthermore, measurement data is not always available to feed the models. Therefore, it is decided to establish a new approach by using data from CFD calculations, to have a clear picture of the aerodynamics on the whole fuselage. The following two sections provide an overview of the CFD calculations performed and the analysis methods conducted, to achieve the required aerodynamic parameters as an input for the models. Beside this, CFD data is needed as an input for CAA calculations that are performed as well and presented in chapter 5.2.
Firstly, chapter 4.1 gives an overview of the numerical setup and the performed CFD calculations. Furthermore, the quality of the CFD calculation as well as the special needs for acoustics are discussed. Secondly, in chapter 4.2 the analysis methods and the available data are presented.

4.1 Numerical Setup

CFD calculations were performed with DLR's in-house code TAU [33, 76], applying a Reynolds Stress turbulence model (RSMg) [87]. The Reynolds Stress model belongs to the Reynolds-averaged Navier-Stokes (RANS) modelling and represents the highest level of this class of models. For each component of the Reynolds stress tensor a transport equation is solved. Further, an additional equation for the length scale is used. Here, a formulation for $g(=\sqrt{\frac{1}{\omega_D}})$ is applied, with ω_D representing the specific dissipation rate. This alleviates the problem of singularity for ω_D near the wall. In regions, where appropriate near wall grid resolution is difficult to achieve, e.g. the transition of wing to fuselage, amendable grids often lower the convergence rate massively or lead to numerical errors. This can be avoided by using the g formulation for the length scale equation. CFD computations were carried out with TAU 2014.2 and 2015.2 versions. Upwind discretisation for the inviscid fluxes and Runge-Kutta time stepping scheme were applied.
In a first step, the mesh generation was performed with the grid generator SOLAR

[62], according to Airbus best practice. The advantage of SOLAR in the case of a full aircraft is that main parts of the fuselage and wing can be meshed using a suited degree of structurisation. Therefore, the generation of quite thick hexahedral and prismatic layers, to cover the complete fuselage boundary layer, is automatically possible. Here, the geometry of an Airbus A320 without engines, but including all other details, like HTP, VTP, winglets and flap tracks, was used. Figure 4.1(a) gives an impression of the detailed geometry without engines. Due to the fact, that the main focus is on the boundary layer at the fuselage, this is assumed to be a straight simplification, to increase the numerical quality and to decrease costs. During the first test it was decided to further simplify and optimise the aircraft geometry, to simplify the meshing process and therefore the to increase the quality of the mesh. Therefore, all attachments at the wing, like winglet and flap tracks, were removed to create a clean wing. This new, clean wing aircraft configuration is presented in Figure 4.1(b). The mesh for the clean wing configuration contains about 17 mio. nodes in total, thereby 13 mio. nodes belong to hexahedral elements, which mainly reproduces the near field of the fuselage and therefore the turbulent boundary layer.

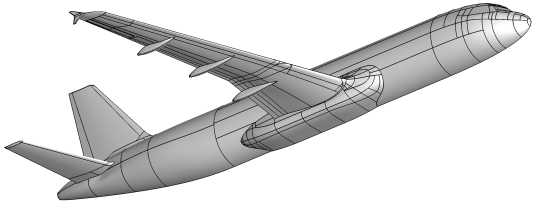

(a) A/C without engine

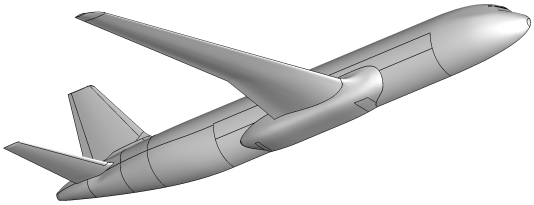

(b) A/C with clean wing

Figure 4.1: A320 CAD half model for CFD, similar to [58]

Special attention was payed to the mesh design, to create a proper resolution of

the boundary layer around the fuselage. The aim, of generating a thick hexahedral layer on the fuselage, to resolve the whole boundary layer was achieved with the clean wing configuration. A comparison between the mesh with detailed and clean wing is presented in Figures 4.2(a) - 4.2(d). Figures 4.2(a) and 4.2(b) show a slice of the half model along the wing with a sweep angle of 20°. Figures 4.2(c) and 4.2(d) show the respective zoomed areas around the second flap track. Striking is a decrease of thickness in the structured mesh layer in the flap track area on both sides (pressure- and suction side) of the wing. This is caused by the flap track itself, which constitutes a disturbance for the automated meshing process and therefore lowers the thickness of the structured layer. In the area of these intersections, so called "junction sources" are added into the mesh. Due to that, anisotropy is removed from the mesh and in the vicinity of the intersections an isotropic mesh is created, which finally lowers the thickness of the structured part of the mesh. SOLAR has an abort criterion that stops the structured meshing due to disturbances. Therefore, it is important to prohibit the abortion in a too early stage, to achieve a structured layer that resolves the whole boundary layer. These disturbances on the wing influences the hexahedral layer on the fuselage directly, which is visible in the comparison of the two cases in Figures 4.2(a) - 4.2(d), where the lower degree of disturbance in the clean wing configuration leads to a much thicker structured mesh layer on the fuselage.
On the top of the fuselage, in the front area, at roughly $x = 9$ m, the structured layer has a thickness of 0.34 m and consists of 34 points in direction normal to the fuselages surface for the mesh around the detailed geometry (OLD mesh, cf. Fig. 4.1(a)). For the clean wing version (NEW mesh, cf. Fig. 4.1(b)), a thickness of 0.58 m with 53 points was achieved. Cell thickness is increasing with increasing distance to the surface, which points out the importance of a thick structured layer, to resolve the boundary layer properly. The OLD mesh has a thickness of $1 \cdot 10^{-5}$ m for the first cell, whereas the NEW mesh has a first cell thickness of $2 \cdot 10^{-6}$ m. Beside this, a boundary layer thickness of $\delta_l = 0.30$ m is resolved with 28 points and 50 points for the OLD and the NEW mesh, respectively. This follows a thickness of the last cell of 0.072 m and 0.059 m for the OLD and NEW mesh. Especially for areas with thin boundary layers of e.g. $\delta_l = 0.06$ m, a high mesh resolution is an important factor for the extraction of the aerodynamic parameters. An example for this is shown in Figures 4.3(a) and 4.3(b). Figures 4.3 present data from the top of the fuselage at $x = 9\,\mathrm{m}$ at standard cruise flight condition. The magenta line depicts the results from the first SOLAR mesh (OLD) and blue shows the results from the clean wing SOLAR mesh configuration (NEW). Data are directly taken from the nodes of the mesh normal to the surface and no interpolation is performed. Figure 4.3(a) shows the turbulence kinetic energy (TKE) and Figure 4.3(b) the velocity parallel to the fuselage along the aircrafts

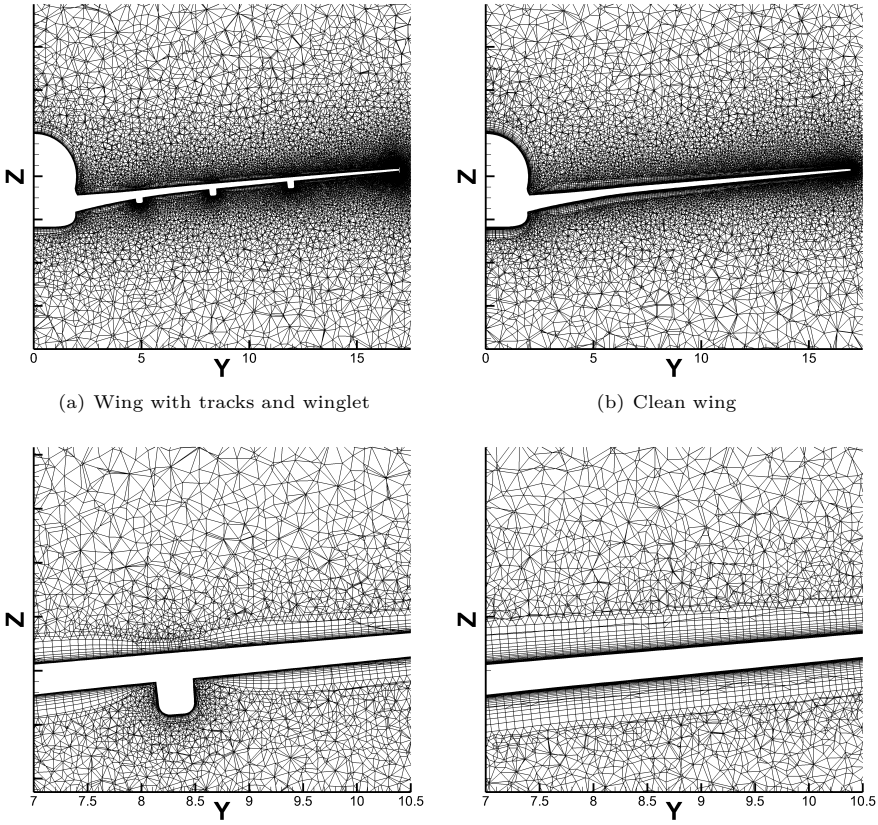

(a) Wing with tracks and winglet

(b) Clean wing

(c) Wing with tracks, zoomed

(d) Clean wing, zoomed

Figure 4.2: Mesh quality of different wing configurations without engine, similar to [58]

x-axis. Turbulence kinetic energy (TKE, k) is calculated by the turbulence model, used for the closure of the Reynolds equation in a CFD calculation [69]. In the RSMg model, the Reynolds stresses are the components of a second-order tensor and the TKE can be calculated by the diagonal components of the Reynolds stress tensor, which are the normal stresses, like

$$k = \frac{1}{2}(\overline{u_x'^2} + \overline{u_y'^2} + \overline{u_z'^2}) \ . \tag{4.1}$$

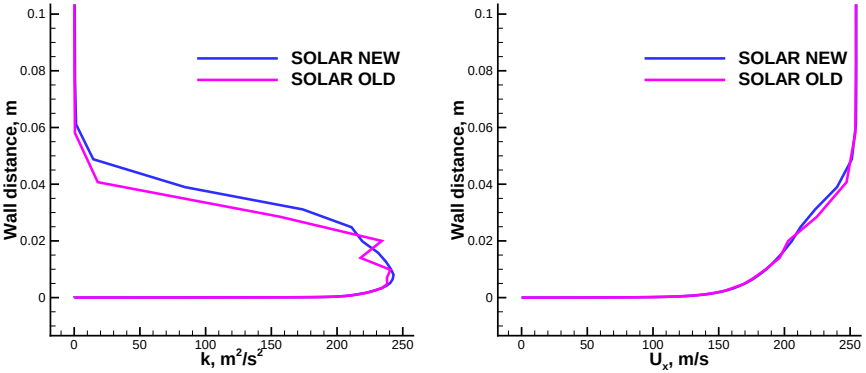

(a) Turbulence kinetic Energy

(b) Velocity profile

Figure 4.3: Grid resolution SOLAR OLD vs. NEW, influence on parameters

Especially the shape of the TKE distribution reflects the lower resolution in the OLD mesh. The shape is serrated and not smooth, like it is in the NEW mesh. An equal effect is visible in the course of the velocity profile, but not that pronounced. Beside these criteria, the dimensionless wall distance (y^+) is a measure of the grid quality. This parameter should be lower than 1 and is defined as

$$y^+ = \frac{\mathrm{U}_\tau \cdot y_w}{\nu} \ , \text{ with } y_w \text{ as the wall distance .} \tag{4.2}$$

Figures 4.4(a) and 4.4(b) depict y^+ for both meshing cases, with a colouring from 0 to 1. Huge differences are visible for the two cases. The OLD mesh, shown in Figure 4.4(a) exhibits values $y^+ > 1$ everywhere on the fuselage. Values are between $y^+ = 3...4$, which is sufficient for aerodynamic calculations but could cause first inaccuracies in the turbulent boundary layer region. In contrast, the NEW clean wing mesh (Figure 4.4(b)) comes up with values $y^+ < 0.5$ all over the fuselage and therefore complies with the y^+ criterion. Finally, several CFD calculations were performed on the A320 with the NEW SOLAR mesh and TAU 2015.2 version. The different configurations were close to be equal to the flight test configurations and in detail listed in Table 4.1 (Here, the second column gives the respective flight test (FT) configuration).

To sum up, following the Airbus best practices of mesh generation with SOLAR, the fuselage itself was not sufficiently meshed for acoustical purposes. Maintaining

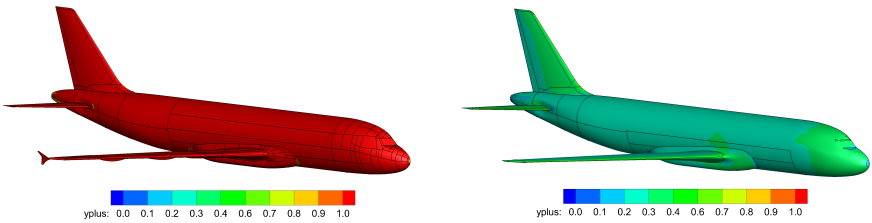

(a) Grid with flap tracks and winglets

(b) Grid with clean wings

Figure 4.4: Investigation of y^+ for different CFD grids

Table 4.1: CFD flight conditions

	FT Conf.	FL [100 ft]	Ma [-]	α_{AoA} [°]	TAS [m/s]	Δ ISA [°C]
1	E17	390	0.78	2.4	231	+1.25
2	C6	350	0.82	1.4	247	+10
3	C7	350	0.78	2.0	237	+10
4	C8	350	0.72	3.0	217	+10
5	C26	310	0.78	0.9	236	-1.3

the best practice and simplifying the aircraft in terms of neglecting details, a sufficient CFD mesh from the acoustical point of view could be generated.

4.2 Analysis of Flow Parameters

For the analysis of the required aerodynamic parameters, a Matlab script was developed that extracts flow parameters at predefined positions on the fuselage automatically. In a first step, these predefined positions correspond to the microphone and Kulite positions, presented in Figures 2.2, 2.6, 2.7. However, it is possible to analyse every position of interest, by depositing a different position data base. Furthermore, the extracted parameters are applied as source data for the auto-spectra as well as the wavenumber-frequency models. Required parameters are listed in Table 4.2 with the corresponding CFD source solution. This could be either the surface solution, for parameters directly calculated on the wall or the volume solution, for parameters not directly measured on the wall. Direct extraction from the surface solution is possible for the friction coefficient c_f and

Table 4.2: CFD parameters and corresponding solution

Parameter	Volume solution	Surface solution
U_e	x	
δ_l	x	
k	x	
c_p		x
c_f		x
dc_p/dx		x

the pressure coefficient c_p, which is used to calculate the pressure gradient as

$$\frac{dp_l}{dx} = q \cdot \frac{dc_p}{dx} \ , \text{ with } c_p = \frac{p_l - p_\infty}{q} \ , \tag{4.3}$$

with $q(= 1/2 \rho U_\infty^2)$ representing the dynamic pressure, p_l and p_∞ the local and far field static pressures, respectively. Turbulence kinetic energy (k) is determined from the volume solution in a perpendicular slice above the requested position by making use of the surface normal vector.
Only the boundary layer thickness and the respective edge velocity (U_e) are not instantly ascertainable. According to flat plate theory, the turbulent boundary layer edge is defined where the flow velocity reaches 99% of the free stream velocity U_∞ [75, 69]. Especially in areas with non-zero pressure gradient this definition is not practicable due to flow acceleration and deceleration. Hence, three different methods were tested to determine these quantities in a reliable quality as well as in a fully automated way.
Firstly, following the derivation of Eisfeld [24], it is assumed to calculate a virtual local Mach number obtained from the isentropic pressure relation [83], leading to

$$Ma_l^2 = \frac{2}{\kappa - 1} \left[\frac{1 + \frac{\kappa-1}{2} Ma_\infty^2}{\left(c_p \frac{\kappa}{2} Ma_\infty^2 + 1 \right)^{\frac{\kappa-1}{\kappa}}} - 1 \right] \ , \tag{4.4}$$

respectively

$$U_l^2 = \frac{2\kappa RT}{\kappa - 1} \left[\frac{1 + \frac{\kappa-1}{2} Ma_\infty^2}{\left(c_p \frac{\kappa}{2} Ma_\infty^2 + 1 \right)^{\frac{\kappa-1}{\kappa}}} - 1 \right] \ , \tag{4.5}$$

with the temperature T, the isentropic exponent $\kappa = 1.4$ and specific gas constant $R = 287.058 \frac{J}{kg\ K}$. At the analysed position, the boundary layer thickness is defined as the wall distance of the point in the flow where $U = 0.99 \cdot U_l$, which is

hence U_e. For this method a fully automated process is not possible because it requires corrections by hand in a multitude of cases.
Secondly, a more simple approach was tested, based on best practice procedures from DLR aerodynamics experts. This method makes use of the drop of total pressure in the vicinity of the fuselage due to a change in dynamic pressure. Finally it is assumed to find the edge of the TBL at

$$\frac{p_{t,l}}{p_{t,\infty}} = 0.98 \text{ , with } p_t = p_{dynamic} + p_{static} = \frac{\rho}{2}U^2 + p_{static} \text{ .} \tag{4.6}$$

Here, the total pressure $p_{t,\infty}$ is taken from the far field of the CFD volume solution. Beside this, $p_{t,l}$ describes the total pressure in the near wall region and p_{static} is assumed to be constant. With knowledge of the position of this specific pressure ratio, the boundary layer edge velocity as well as the thickness can be estimated. This method is fully automatable and therefore fulfills all criteria for application.
Thirdly, data for validation were taken from flight test measurements, acquired within the CENT-LSHX project in the frame of the European R&T programme JTI Clean Sky [18]. Pressure rake measurements were performed and these data were analysed with regard to the boundary layer thickness.

Figures 4.5(a) and 4.5(b) show the comparison of data from the first and second method, which show a good conformity. Figure 4.5(a) shows the deviation between method one (Equ. (4.4) and (4.5)) and two (Equ. (4.6)) in percent for the boundary layer thickness at a line along the fuselage, in the window plane and on the top of the fuselage (roof). The median of the δ_l–deviation for the window plane is 3.6% and for the roof area it is 4.9%. In Fig. 4.5(b) the deviation between the methods for U_e estimation is shown. Equally, the median of the U_e–deviation can be quantified; quantified as 1.1% for the roof area and 0.93% for the window plane, respectively. It is noticeable, that the differences between both methods are increasing in areas with accelerated and decelerated flow. Here, the first method is assumed to give better results than the second. The second method assumes the static pressure part to be constant, which is not correct in the accelerated and decelerated flow areas. This simplification falsifies the results.
Nevertheless, for the final evaluation it is decided to use the second method because it allows a fully automated analysis process without human intervention, which preserve the results from human interpretation and make them 100% reproducible. Further comparisons between method two and the measured validation data from flight tests, which are not shown here, confirm a reasonable accuracy of the second method. Measurement data (method three) and the automated analysis (method two) show a variation in the data for δ_l of 1.7% and for U_e of 0.6%, respectively. This comparison was done with data from the underpart of the

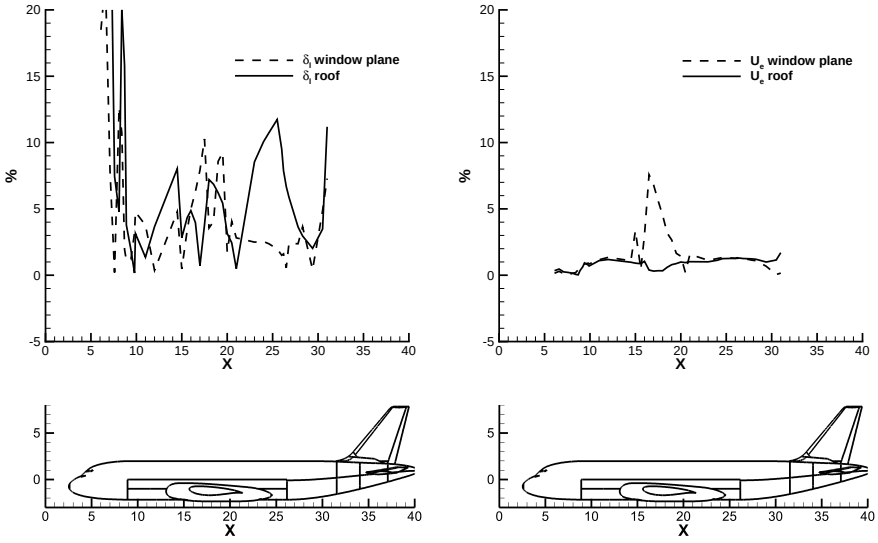

(a) Comparison of δ_l

(b) Comparison of U_e

Figure 4.5: Comparison CFD vs. virtual Mach number estimation method [58]

fuselage near the wings at FL390 and Ma = 0.82. The edge velocity was determined as $U_e \approx 248$ m/s and the thickness of the boundary layer was estimated as $\delta_l \approx 0.18$ m.

5 Prediction Models

This chapter contains all modelling activities on auto-spectra and wavenumber-frequency prediction models. It is divided in two major parts. Firstly the enhancements of the semi-empirical GOODY model for auto-spectra predictions are presented in chapter 5.1. Secondly, a full numerical approach for the prediction of auto-spectra as well as wavenumber-spectra is given in chapter 5.2.

5.1 CFD based Semi-Empirical Auto-Spectra Prediction Model

In this chapter a new model for CFD based auto-spectra prediction is presented, a rough overview of a forerunner of this new model can also be found in [58, 59]. After comparison of the available measurement data with published auto-spectra models in Figures 3.2(c)-3.2(d) it is decided to use GOODY's [37] model as a starting point for further development. Beside this, the GOODY model is part of the CHASE and CHASE–HOWE model family and is the most validated model with measurement data sets. Remarkable is the history of these models because they were developed for low speed applications. Nevertheless, the applicability seems to be better, when compared with the original high speed models, like the one of EFIMTSOV. This decision is also backed with the findings of GLOERFELT [35] and ALAOUI [1] that Mach number and compressibility effects for flows, ranging from $Ma = 0.5 \ldots 0.9$ have very low effect on the structure of turbulence.
In the following sections, firstly, a detailed overview of the GOODY model, its flexibility and adaptability is provided in chapter 5.1.1. Secondly, in chapter 5.1.2 the applicability to measurement data is discussed in detail, with a following scaling experiment. Thirdly, CFD data is analysed with regard to the model and new definitions of the original model parameters are introduced in chapter 5.1.3. Finally, some preliminary results of the new DLR auto-spectrum model are presented in chapter 5.1.4.

5.1.1 Model Parameter Study and Uncertainties

The GOODY [37] model offers a high degree of confidence when extrapolated to flows with a higher Reynolds number and zero pressure gradient. GOODY used

the Chase–Howe model (presented by Howe [51]) as a starting point for the development of his model. He reviewed the experimental surface pressure spectra of six research groups in his dissertation [36], that cover a large Reynolds number range: $1.4{\cdot}10^3 < \mathrm{Re}_\theta < 2.34{\cdot}10^4$, $\mathrm{Re}_\theta = \frac{\mathrm{U}_e\theta}{\nu}$, with U_e, θ and ν, the boundary layer edge velocity, momentum thickness and kinematic viscosity, respectively. This Reynolds number span is representative for most laboratory flows, that is, wind tunnels and water tunnels ($\mathrm{Re}_\theta \sim 10^3 - 10^4$). Most practical flows, like the flow over airplanes have a larger momentum Reynolds number ($\mathrm{Re}_\theta \sim 10^5 - 10^6$) [37]. This section gives a detailed insight into the original Goody model (Equ. (5.1)), and illustrates the sensitivity of its prediction on the introduced exponents and coefficients **a**-**h**.

$$\frac{\Phi(\omega)\mathrm{U}_e}{\tau_w^2\delta_l} = \frac{\mathbf{a}\left(\frac{\omega\delta_l}{\mathrm{U}_e}\right)^{\mathbf{b}}}{\left[\left(\frac{\omega\delta_l}{\mathrm{U}_e}\right)^{\mathbf{c}} + \mathbf{d}\right]^{\mathbf{e}} + \left[\left(\mathbf{f}R_T^{\mathbf{g}}\right)\left(\frac{\omega\delta_l}{\mathrm{U}_e}\right)\right]^{\mathbf{h}}} \tag{5.1}$$

Main aerodynamic quantities, included in the model, are the local boundary layer thickness δ_l, the boundary layer edge velocity U_e and the skin friction coefficient c_f. The wall shear stress τ_w can be expressed by c_f or the friction velocity $\mathrm{U}_\tau \left(= \sqrt{\frac{\tau_w}{\rho}}\right)$. The originally defined coefficients and exponents by Goody are presented in Tab. 5.1. Furthermore, in Fig. 5.1(a) - 5.2(c) the effect of a variation of these parameters is presented.

Table 5.1: Original Goody model coefficients and exponents

a	**b**	**c**	**d**	**e**	**f**	**g**	**h**
3.0	2.0	0.75	0.5	3.7	1.1	-0.57	7.0

The parameter sensitivity study was conducted at typical aircraft cruise flight condition, $\mathrm{U}_\mathrm{e} = 239$ m/s, FL 350, $\delta_l = 0.06$ m, $\mathrm{Re}_x \approx 5 \cdot 10^7$ $\left(\mathrm{Re}_x = \frac{\mathrm{U}_e \cdot x}{\nu}\right)$. In this Reynolds number region only the numerator (red and black) and the first bracket term of the denominator (red) of Equ. (5.1) are relevant and the blue part (second bracket term of the denominator) is negligible. The blue part, containing **f**, **g** and **h** as well as R_T, controls the very high frequency range of the spectrum and takes into account the ω^{-5} slope in the high frequency region. For the present application its influence begins far above $\mathrm{Sh} \gg 70$ $\left(\mathrm{Sh} = \frac{\omega\delta_l}{\mathrm{U}_e}\right)$ and is therefore not relevant for aircraft applications at cruise flight conditions. The ω^{-5} slope is calculated by $\mathbf{b} - \mathbf{h} = -5$ in Equ. (5.1).

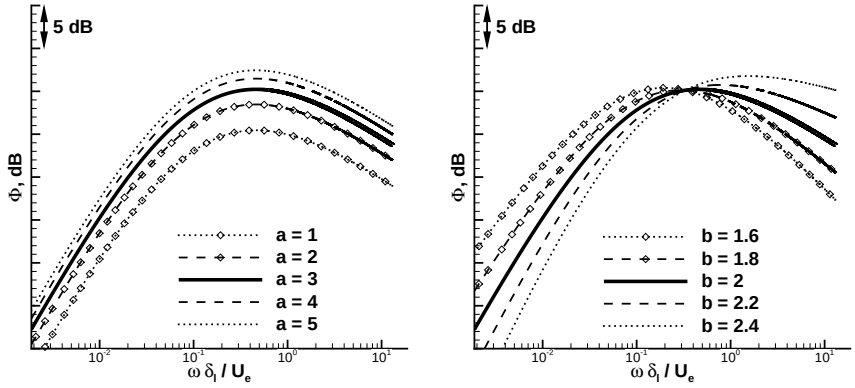

(a) Variation of coefficient **a**

(b) Variation of exponent **b**

Figure 5.1: Goody parameter variation study, part 1 [58]

The baseline in the parameter study is always plotted in bold black and incorporates the original GOODY parameters. Variations of the coefficient **a** are sketched in Fig. 5.1(a). **a** has no influence on the spectral shape of the spectrum, but controls the level by shifting the spectrum parallel up and down. Fig. 5.1(b), 5.2(a) and 5.2(c) show that the exponents **b**, **c** and **e** affect the frequency dependent shape of the spectrum. In this group, exponent **b** is the only exponent, changing the very low frequency slope of the spectrum ($\mathrm{Sh} = 2 \cdot 10^{-3}$ ... $2 \cdot 10^{-1}$), which is the outer scaling region, while significantly touching also the mid frequency region's slope ($\mathrm{Sh} = 2 \cdot 10^{-1}$ ... $2 \cdot 10^{1}$) or also called universal scaling region. Beside this, exponents **c** and **e** mainly modify the mid frequency region, in which **c** and **e** also have little influence on the position of the maximum. Exponents **b**, **c** and **e** control the slope of the universal scaling region of the spectrum, which is expected to follow a $\omega^{-0.7...-1.1}$ principle for zero pressure gradients (cf. Figure 3.1). The ω exponents are calculated by $\mathbf{b} - \mathbf{c} \cdot \mathbf{e} = -0.7... - 1.1$. Finally, the last coefficient **d**, shown in Fig. 5.2(b) also modifies the position of the maximum in terms of absolute level and frequency position but has no influence on the spectral shape. It shifts the spectrum along the mid frequency slope.

Finally, the uncertainty of the varying $\mathrm{U_e}$– and δ_l–prediction, contemplated in chapter 4.2, on the predicted spectra is also quantified. An $\mathrm{U_e}$–variation of $\pm 7.6\%$ causes a level change of the predicted spectrum of $< \pm 1$ dB, while a δ_l–variation

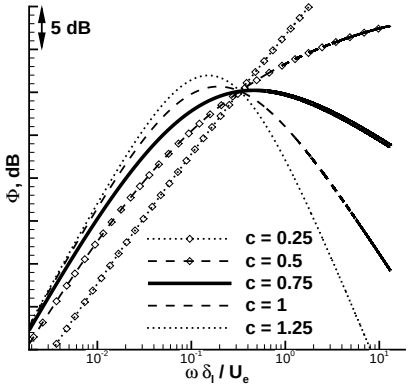

(a) Variation of exponent **c**

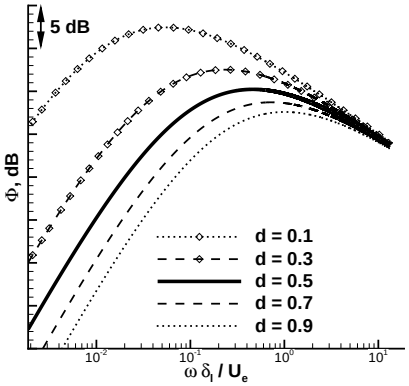

(b) Variation of coefficient **d**

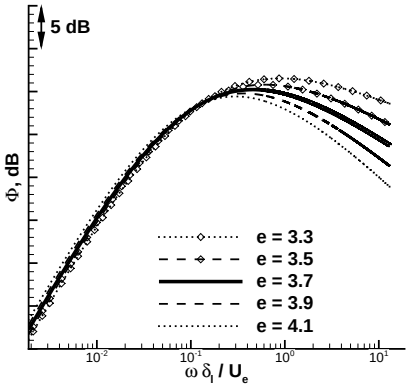

(c) Variation of exponent **e**

Figure 5.2: Goody parameter variation study, part 2 [58]

of ±12% causes a level change of $< \pm 0.5$ dB. Furthermore, a negligible frequency shift is apparent.

5.1.2 Scaling Tests

In this chapter, the GOODY auto-spectrum model is applied to different positions on the aircraft and compared with the regarding measurement results. For the model, as presented in Equ. (5.1), aerodynamic input is required. These aerodynamic parameters can, on the one hand side, be calculated by flat plate estimates, following the approaches of e.g. SCHLICHTING [75] or BLAKE [4, 5] or, on the other hand side, the parameters can be calculated based on CFD calculations. Prediction and measurement results for two different areas are presented in the following, firstly the overwing area and secondly the wing wake area are shown (For sensor positions compare Fig. 2.7).
In Figures 5.3(a) and 5.3(b) the semi-empirical model of GOODY (aerodynamics based on flat plate estimates) is presented in comparison with the measurement data for overwing and wing wake area, respectively. One can see that the GOODY model, subject to these estimates does not fit the measured data, neither in level nor in shape. The GOODY model predicts the same auto-spectrum for all positions, which is a consequence of the aerodynamic data. Both sensor groups and especially the sensors within a group have similar distance to the aircrafts nose and therefore the flat plate estimate yields similar aerodynamic parameters. The attempt to improve these results by using flow parameters from CFD calculations, which takes local phenomena (e.g. aircraft integration effects) into account is presented in Figures 5.3(c) and 5.3(d) for overwing and wing wake area, respectively. One can see that the semi-empirical models does not reproduce the measurement results either. However, differences in the predicted auto-spectra are obvious, which is an improvement compared with the prior prediction without CFD data. Indeed, the order of predicted spectra does not fit the measurements, which raises the question, if the GOODY model includes all important aerodynamic parameters. Focusing e.g. on the prediction for the most forward positioned sensor in Figure 5.3(c), the difference between measurement and prediction is about 6 dB at $f \approx 350$ Hz. Here, the black marked sensor has the highest levels compared to the two others, while it has the most forward x-position of this group. From theory the most forward sensor should have lowest levels. Taking further the analysed data from turbulence kinetic energy into account (Fig. 5.4(a), 5.4(c)), this could be one of the missing parameters in the auto-spectra prediction. For the overwing area, the most forward positioned sensor shows the highest k values above the sensor in the CFD data and the highest absolute levels for the auto-spectrum. While the sensor located far away from the wing, with the lowest k value gives the lowest absolute auto-spectrum levels. Thus, a precise quantification of the turbulence kinetic energy could improve the prediction result when taken into account. Furthermore, flow acceleration or deceleration influences the auto-spectra, as known

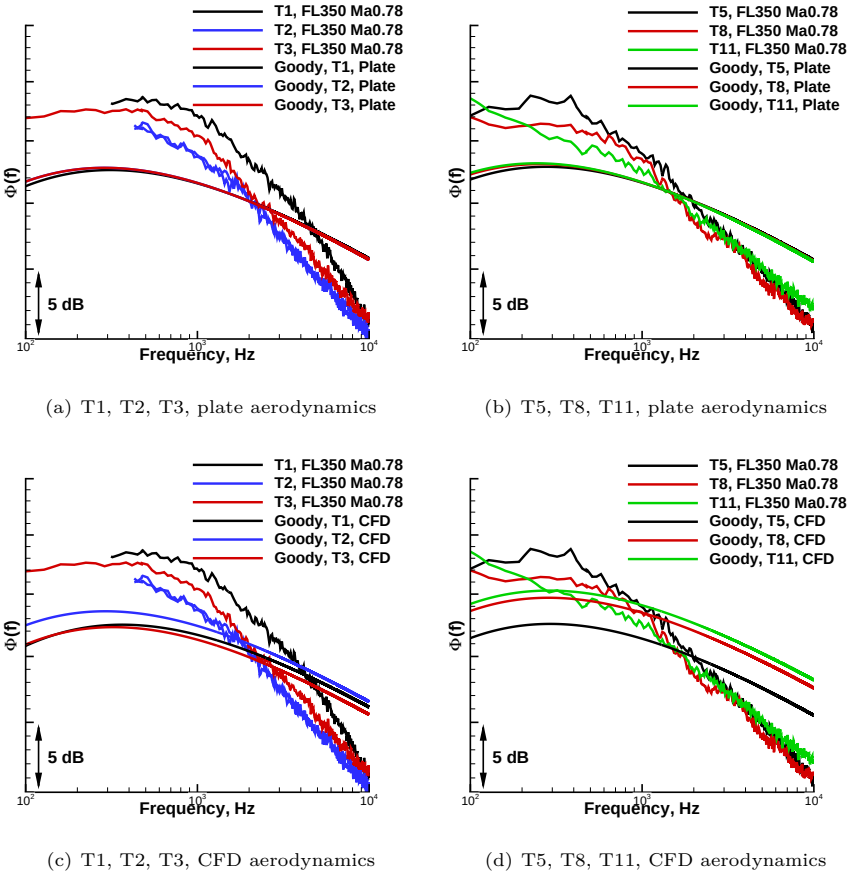

(a) T1, T2, T3, plate aerodynamics

(b) T5, T8, T11, plate aerodynamics

(c) T1, T2, T3, CFD aerodynamics

(d) T5, T8, T11, CFD aerodynamics

Figure 5.3: Measurement compared with Goody prediction from different aerodynamic inputs [57]

from wind tunnel test from e.g. Hu [53] and should also be taken into account. Pressure gradients are low for all sensors positioned slightly behind and above the wing, as shown by the c_p distribution in Fig. 5.4(b) and 5.4(d).
Beside this, the prediction for the most forward positioned sensor in the wing wake area (Fig. 5.3(d)) shows a similar behaviour as the most forward positioned one above the wing, again a difference of 5 dB is present at $f \approx 350$ Hz in comparison

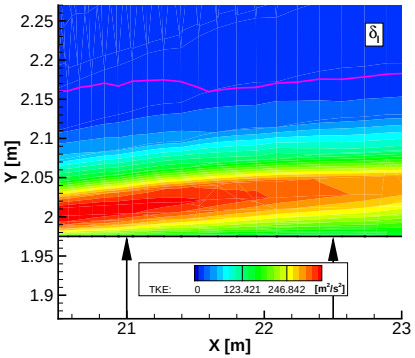

(a) TKE distribution at sensors close to the wing

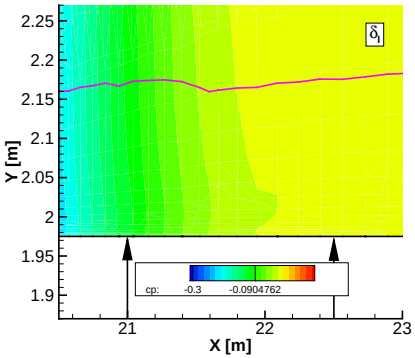

(b) c_p distribution at sensors close to the wing

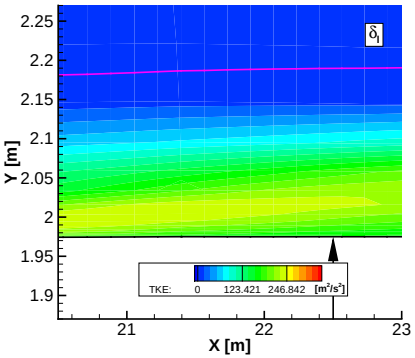

(c) TKE distribution at sensor with huge distance to the wing

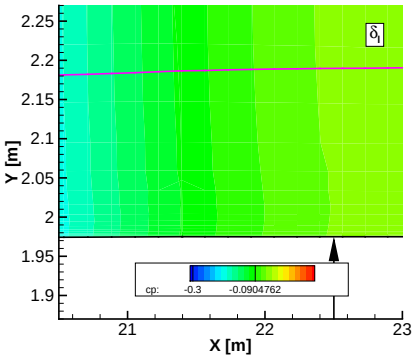

(d) c_p distribution at sensor with huge distance to the wing

Figure 5.4: TKE, c_p and δ_l comparison at overwing area, see also [57]

to the measurement. In this case, the value of kinetic energy is not as high as in the before mentioned case, but a peak value of energy exists above the sensor (Fig. 5.5(a)). Furthermore, Figure 5.5(b) shows decelerated flow over the most forward positioned sensor, which triggers a low frequency energy increase and could, in combination with the kinetic energy distribution explain the differences in the spectra. Concluding, it might be important to adapt the auto-spectra model with k and c_p distribution information, to capture the flow history and upstream flow

development and finally to predict measured auto-spectra correctly in shape and level.

Therefore, the model developed by Catlett [10], which is a model for predict-

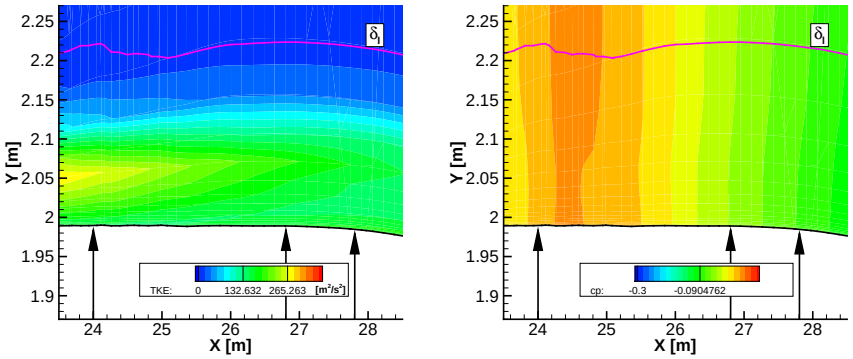

(a) TKE distribution at sensors

(b) c_p distribution at sensors

Figure 5.5: TKE, c_p and δ_l comparison at wing wake area, see also [57]

ing auto-spectra under adverse pressure gradients, was tested. The prediction results (results not shown) were not able to fit the measurement data and does not constitute an improvement of the Goody prediction results at the beforehand mentioned positions on the fuselage at cruise flight condition. Also the Catlett model does not include the turbulence kinetic energy, which is assumed to be a driving parameter in the auto-spectra prediction.

To prove this assumption, a scaling experiment is conducted and for this purpose the original normalisation, proposed by Goody [37], is applied to the data in Figures 5.6(a) and 5.6(b) , which consists of the outer variables U_e, δ_l and the inner variable τ_w, like

$$\frac{\Phi(\omega)U_e}{\tau_w^2 \delta_l} \ . \tag{5.2}$$

Beside this, the scaling is applied to measured spectra in areas without disturbances, like in the window plane far away from the wings, a good collapse of the data is achieved (Results were published by the author in [58]). In contrast data comparison for the overwing and wing wake area show a different scaling behaviour. In Figures 5.6(a) and 5.6(b), respectively, one can see the original scaling – data do not collapse, which shows that the main parameter driving the absolute level is missing. However, in Figures 5.7(a) and 5.7(b) data collapse in the peak

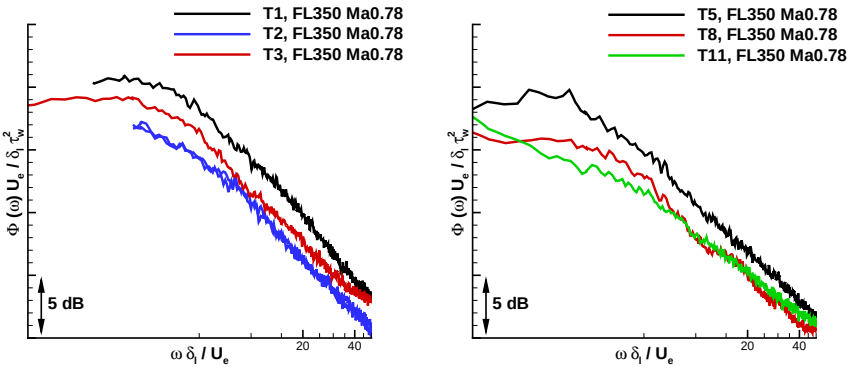

(a) T1, T2, T3, Goody scaling

(b) T5, T8, T11, Goody scaling

Figure 5.6: Measurement scaled with Goody method [58]

area, where a different scaling method is applied. Here, the maximum value of the kinetic energy, within the local turbulent boundary layer profile, is taken into account, like

$$\frac{\Phi(\omega)\mathrm{U_e}}{\delta_i(\rho k)^2} \ . \tag{5.3}$$

The presented scaling results give a strong lead that the maximum of kinetic energy above a sensor dominates the absolute level of the spectrum. Therefore, turbulence kinetic energy is taken into account as one important parameter in the proposed extension of the original Goody model, which is presented in the next chapter.

5.1.3 Parameter Description

The content of this chapter is the development of the proposed extension of the original Goody model based on Airbus A320 flight test data. For this, the original formulation of Goody (Equ. (3.14)) is not modified, however the variables as well as the constant model parameters are adapted. As learned from chapter 5.1.1, the coefficients and exponents **f**, **g** and **h** are not affecting the spectrum at present flight conditions in the frequency range of interest. Thus, the development of new formulations is not primarily focusing on them, only a supplementary adaptation

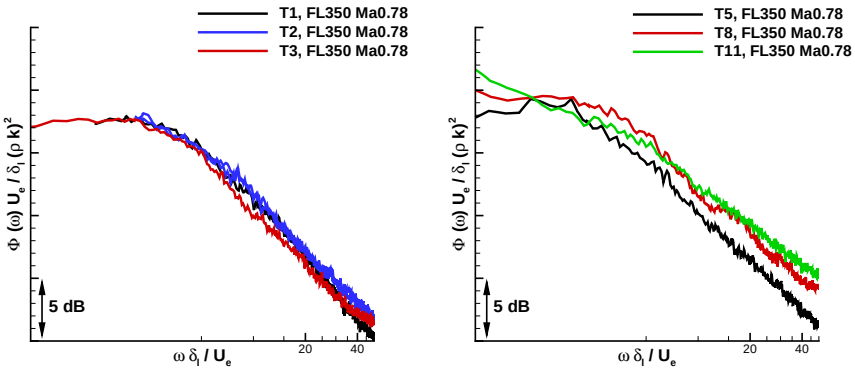

(a) T1, T2, T3, TKE scaling

(b) T5, T8, T11, TKE scaling

Figure 5.7: Measurement scaled with TKE method [58]

is performed to retain the original high frequency behaviour of the Goody model. In a first step, coefficient **b**, which was defined as $\mathbf{b} = 2$ by Goody is adapted to the low frequency slope of the data. From the literature it is known that a slope of $\omega^{0.2...0.8}$ is typical for zero pressure gradient (ZPG) flows (cf. Hu & Herr [53] and Farabee & Casarella [31]), but also ω^2 slopes are found in the literature (cf. [37] or Fig. 3.1 [56]). Furthermore, measurements by Catlett et al. [10] and Suryadi [84] showed increased slopes for adverse pressure gradient (APG) cases of $\omega^{0.6...1.0}$. An adaption of the model to

$$\mathbf{b} = 0.5 \ , \tag{5.4}$$

which correlates to a $\omega^{0.5}$ slope, give best results compared to the flight test measurements that are close to zero pressure gradients.
In a second step, coefficient **a** is expressed by evaluating the maximum of the frequency independent value of the turbulence kinetic energy ($max(k)$). This is done because the scaling method in Equ. (5.3) gave a perfect collapse of the spectral peak values as seen from the scaling experiment. Beside this, only parameter **a** shifts the spectra up and down without changing the spectral shape and is therefore able to reflect this effect. Thus,

$$\mathbf{a} = \left(\frac{k_i}{k_0}\right)^{\gamma_{DG}} \ , \ k_0 = 10^{m^2/s^2} \ , \ k_i = max(k) \ . \tag{5.5}$$

Here, k_i is nondimensionalised by k_0 and γ_{DG} was determined by least square fits of measured to predicted maxima of the auto-spectra. In total, 79 sensors for each of the five analysed flight test configurations were included in the analysis. γ_{DG} was found to be a function of the friction coefficient c_f, like

$$\gamma_{DG} = \gamma_m \cdot c_f + \gamma_c \ , \tag{5.6}$$

dependent on flight level and Mach number, which is presented in Figure 5.8. An

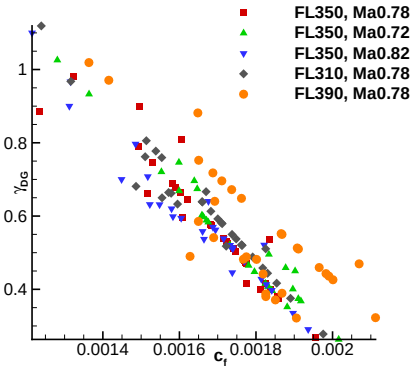

Figure 5.8: γ_{DG} over c_f for all flight configurations

optimised linear fit through all γ_{DG} values in Fig. 5.8 gives different slopes and intercepts for each flight case, which are listed in Table 5.2. From these results a

Table 5.2: γ_{DG} functions; slopes and intercepts

FL	Ma	γ_m	γ_c
350	0.78	-1008.7	2.2712
350	0.72	-1038.0	2.3413
350	0.82	-978.52	2.2010
310	0.78	-1016.1	2.3063
390	0.78	-857.69	2.0920

Mach number and flight level dependency can be directly calculated and yields

$$\gamma_m = 2661.7 \cdot \mathrm{Ma}^2 - 3504.2 \cdot \mathrm{Ma} + 3622.4 + 3.6 \cdot 10^{-2} \cdot \mathrm{FL}^2 - 22.5 \cdot \mathrm{FL}, \tag{5.7}$$

and

$$\gamma_c = -1.3845 \cdot \mathrm{Ma} - 0.7182 - 4.5031 \cdot 10^{-5} \cdot \mathrm{FL}^2 + 2.7361 \cdot 10^{-2} \cdot \mathrm{FL}. \quad (5.8)$$

Combining Equ. (5.6) with Equ. (5.7), (5.8) and inserting into Equ. (5.5), the calculation of **a** is possible for all measurement positions on the aircraft.
In a next step, after the absolute level calibration of the model was performed as described before, the shape of the model is adapted to the measurement data. To adapt the shape, a least squares method is applied to minimise the difference between prediction and measurement by varying the exponents **c** and **e** as well as the coefficient **d**. All these variables influence the frequency dependent position of the spectral peak. Furthermore, exponents **c** and **e** change the whole shape of the auto-spectrum, while shifting the peak value frequency dependently. The frequency dependent shift of the spectral peak is inter alia a consequence of a changing Reynolds number, which is observable in the measurement data in e.g. Figure 2.14. Furthermore, it is known from other measurements (e.g. Hu & Herr [53], Catlett et al. [10]) that the pressure gradient has a strong influence on the shape as well as on the position of the peak value of an auto-spectrum.
For exponent **c**, a dependence on Clauser's [13] parameter, which is often used in the analysis of boundary layer flows and especially in APG flows,

$$\beta_{\delta_l} = \frac{\delta_l}{q}\frac{\mathrm{d}p}{\mathrm{d}x} \text{ or normalised } \beta_{\delta_l} = \delta_l \frac{\mathrm{d}c_p}{\mathrm{d}x} \quad (5.9)$$

was found, with a correction term based on Reynolds number for the high and low Reynolds number cases, like

$$\mathbf{c} = 2.7 + (3 \cdot \beta_{\delta_l}) - \left[6 \cdot 10^{-10} \cdot (0.7 \cdot \mathrm{Re}_{\delta_l}^{0.6} - 2700)^3 + 0.02\right] , \quad (5.10)$$

with

$$\mathrm{Re}_{\delta_l} = \frac{\delta_l \cdot \mathrm{U}_e}{\nu} . \quad (5.11)$$

Beside this, exponent **e** showed a dependency on similar parameters. This time a Clauser parameter, based on a slightly modified Rotta-Clauser length scale, is adopted. The original Rotta-Clauser length scale was introduced by Rotta [72] and Clauser [13] and was defined as

$$\Delta = \delta^* \sqrt{\frac{2}{c_f}} , \quad (5.12)$$

with the displacement thickness δ^*. In this work, the Rotta-Clauser length scale is slightly modified and the displacement thickness is replaced by the local boundary layer thickness δ_l due to reasons of consistency and yields

$$\Delta_{\delta_l} = \delta_l \sqrt{\frac{2}{c_f}} . \quad (5.13)$$

According to FERNHOLZ and FINLEY [32], the length scale Δ is a more appropriate quantity for scaling turbulence, than only using δ_l. Furthermore, by making use of Δ or in this case Δ_{δ_l}, this work follows the philosophy of the work of CATLETT et al. [10], who already presented an adapted GOODY model dedicated to adverse pressure gradients. Finally, the definition of exponent **e** was found to be

$$\mathbf{e} = 0.675 + 0.11428 \cdot \beta_{\Delta_{\delta_l}} + \left[7 \cdot 10^{-11} \cdot \left(\mathrm{Re}_{\delta_l}^{0.6} - 3750\right)^3 - 0.01\right] \ , \tag{5.14}$$

again with a correction term for the low and high Reynolds numbers.
Furthermore, the least squares analysis results for coefficient **d** could be approximated by applying the CLAUSER parameter from Equ. (5.9) and the Reynolds number from Equ. (5.11) like

$$\mathbf{d} = 12 + 2.39 \cdot log\left({\mathrm{Re}_{\delta_l}}^{0.53} \cdot \beta_{\delta_l}^2\right) \ . \tag{5.15}$$

The newly defined exponents and coefficients as well as their dependencies are summed up in Tab. 5.3. Furthermore, the group of parameters, responsible for the very high frequency range, that has up to now not been considered has to be slightly modified. Due to the adaptation of coefficient **b**, from **b** = 2 to **b** = 0.5, exponent **h** in the denominator of Equ. (5.1) has to be adapted from **h** = 7 to **h** = 5.5, to hold the high frequency slope of ω^{-5}. This measure is only based on theoretical deliberation because the measured auto-spectra from the flight test validation data base does not show any ω^{-5} slopes in the high frequency range. The main reason for that is the measurement equipment, which is not able to record data at frequencies above $f = 10$ kHz, where the ω^{-5} slope is expected at the existent high Reynolds numbers of the flight tests. Beside this, results of the calculated parameters **a**, **c**, **d** and **e** for different flight cases are presented in Figures 5.9(a)- 5.9(d). For this purpose, sensors were grouped and the results were randomly allocated to a number, which is used as the x-axis in the plots. The results show that the parameters are varying, dependent on the aerodynamics, and that it is not possible to calculate the auto-spectra with constant values as it is done by the original model of GOODY. The scatter of parameter values at a given sensor shows its sensitivity on the flight condition, while its dependency on the sensor position shows the importance of the local flow. Parameter **a** (Fig. 5.9(a)) shows the strongest scatter among the various flight conditions and positions because of the scatter of kinetic energy and the changing friction coefficient. Beside this, also parameter **d** (Fig. 5.9(c)) shows varying values due to the Reynolds number and pressure gradient dependency. Whereas parameters **c** and **e** (Fig. 5.9(b) and 5.9(d)) are nearly constant values.

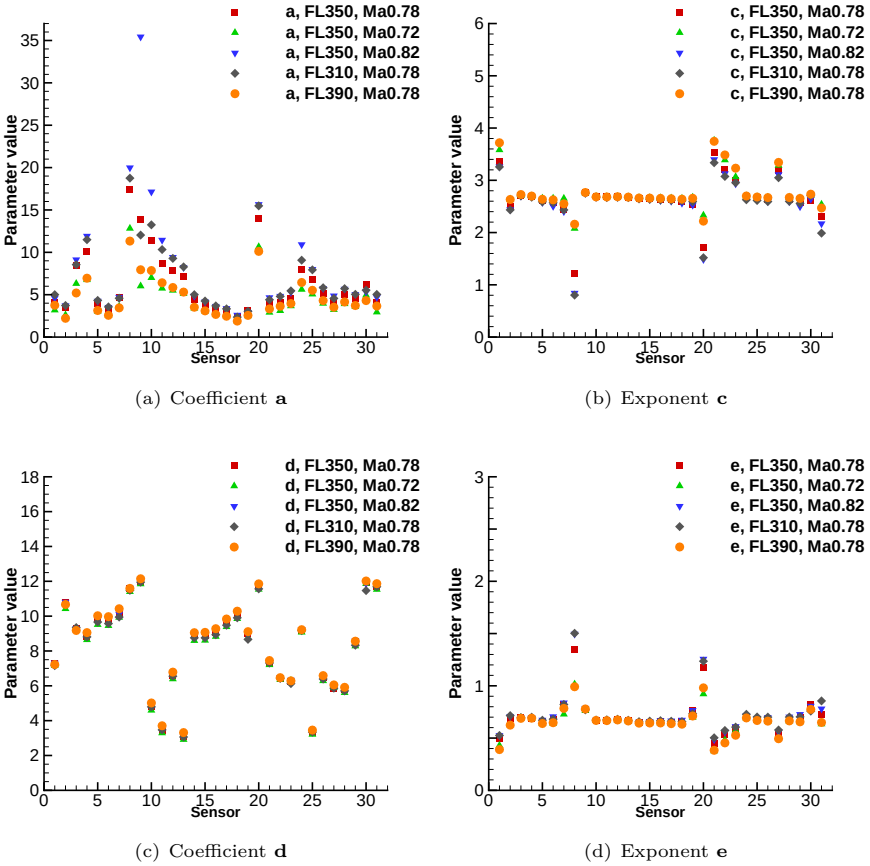

(a) Coefficient **a**

(b) Exponent **c**

(c) Coefficient **d**

(d) Exponent **e**

Figure 5.9: Parameter range of new defined exponents and coefficients for different flight cases

For the presented adaptation of the GOODY model, the validity of the method has been proven within the aerodynamic limits for the ATRA flight test campaign, presented in Table 5.4. Finally, the parameter range depicted in Tab. 5.4 is large and covers most of the important areas on an short to medium-haul range aircraft for standard flight missions.

Table 5.3: New coefficients and exponents

a =	$f(k, c_f, \mathrm{Ma}, \mathrm{FL})$	**b** =	0.5
c =	$f(\beta_{\delta_l}, Re_{\delta_l})$	**f** =	1.1
d =	$f(\beta_{\delta_l}, Re_{\delta_l})$	**g** =	-0.57
e =	$f(\beta_{\Delta_{\delta_l}}, Re_{\delta_l})$	**h** =	5.5

Table 5.4: Aerodynamic limits of the new model

	min	max	unit
U_e	201.7	259.0	m/s
δ_l	0.0603	0.3172	m
c_f	$1.215 \cdot 10^{-3}$	$2.112 \cdot 10^{-3}$	[−]
k_{max}	138.9	454.2	m^2/s^2
dc_p/dx	-0.0858	0.1801	$1/m$
Ma_l	0.679	0.872	[−]
Ma_∞	0.720	0.820	[−]
Re_{δ_l}	350637.8	1961865.8	[−]
FL	310	390	$100ft$

5.1.4 Model Results

In this chapter first results of the further developed Goody model in comparison with the already presented measurement data from Figures 5.3(a)- 5.3(d) are shown in Figures 5.10(a)- 5.10(f). Comparing the results with the new model, one can see a model precision of ±1dB and a good collapse of the measurement and model results. Furthermore, it is an improvement of the original Goody model, whose results were shown in Figures 5.3(a)- 5.3(d) and gave an offset of > 5dB to the measurements. Beside this, the original model was not able to fit the shape of the measured auto-spectra. More results, for more positions and flight conditions, of the new model are presented in chapter 6.1.

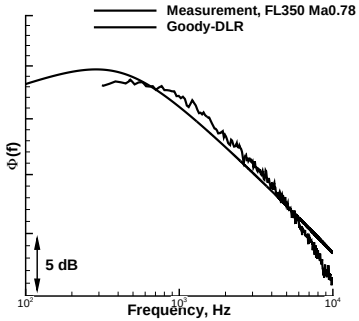

(a) Overwing position close to the wing

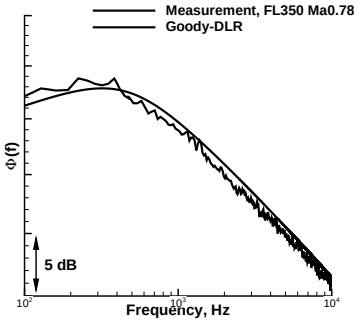

(b) Wing wake position close to the trailing edge

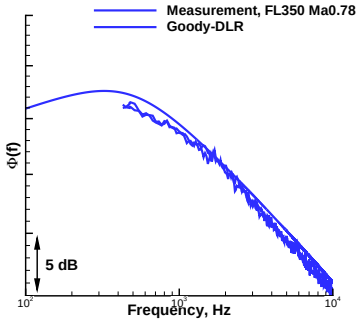

(c) Overwing position far above the trailing edge

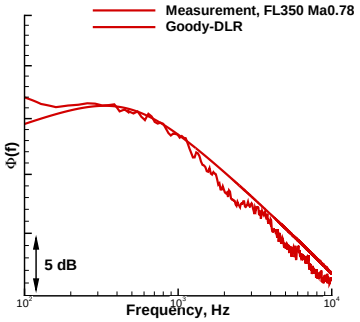

(d) Wing wake position behind the Belly fairing

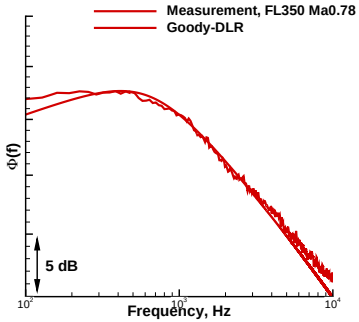

(e) Overwing position close to the trailing edge

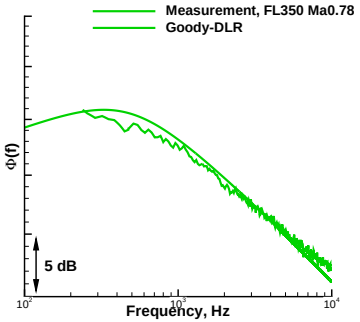

(f) Wing wake position far away from the Belly fairing

Figure 5.10: Measurements compared with adapted Goody-DLR auto-spectrum model, also compare [58]

5.2 CFD / CAA based Prediction

Containing the full numerical prediction approach, this Chapter constitutes, beside the semi-empirical modelling approach in the beforehand Chapter, the second part of the prediction model activities within this thesis.
For the numerical prediction of wall pressure fluctuations, the method of Hu et al. [52, 54] is applied. Therefore, a turbulent boundary layer flow on an aircraft is simulated, using synthetic turbulence, generated by the Fast Random Particle-Mesh Method (FRPM) of Ewert [26, 27]. The stochastic realisation is based on time averaged turbulence statistics calculated from full aircraft RANS computations as described in Chapter 4. According to Hu [54], for incompressible quasi-parallel flow, the fluctuating pressure at the fuselage surface is determined by solving a Poisson equation with an unsteady right-hand side source term derived from the synthetic turbulence realisation, like

$$\Delta p' = -\rho_0 \left(\underbrace{2\frac{\partial \mathrm{U}_1}{\partial x_2}\frac{\partial u_2'}{\partial x_1}}_{mean-shear} + \underbrace{\frac{\partial^2}{\partial x_i \partial x_j}(u_i'u_j' - \overline{u_i'u_j'})}_{turb.-turb.} \right) \tag{5.16}$$

Here, U_1 denotes the mean-flow velocity component in the wall tangential x_1-direction and $u'_{i,j}$ indicates velocity fluctuations. Beside this, ρ_0 is the mean air density and p' the fluctuating pressure. u_2' denotes the velocity fluctuations in wall normal direction.
One methodology to calculate the fluctuating pressures p' within the volume (V_∞) is, to calculate the convolution of the free-space Green function (G) and the right-hand side source term of Equ. (5.16) (Q) over the volume and a mirrored volume ($-\mathrm{V}_\infty$), which yields

$$p'(\mathbf{x},t) = \int_{-\mathrm{V}_\infty}^{\mathrm{V}_\infty} Q(\boldsymbol{\xi},t)\cdot G(\mathbf{x}-\boldsymbol{\xi})\mathrm{d}^3\boldsymbol{\xi} = Q * G \ , \ G = -\frac{1}{4\pi r} \text{ (in 3D)} \ , \tag{5.17}$$

with $r = |x-\xi|$, where ξ denotes the location of the source. The convolution is solved via spatial fast Fourier transform using Hockney's method [49], like $\mathcal{F}\{Q*G\} = \hat{Q}(\boldsymbol{k},\boldsymbol{t})\cdot\hat{G}(\boldsymbol{k})$. Which finally results in the spatial pressure fluctuations by back transformation as $p'(\mathbf{x},t) = \mathcal{F}^{-1}\{\hat{Q}(\boldsymbol{k},\boldsymbol{t})\cdot\hat{G}(\boldsymbol{k})\}$. In the full Poisson equation (Equ. (5.16)), both, mean-shear turbulence interaction and turbulence-turbulence interaction terms are considered.
To prescribe the right-hand side source term in Equ. (5.16), synthetic turbulent velocity fluctuations, calculated by FRPM are used. The main idea in FRPM is

to generate a fluctuating potential ψ_i' with three components from a convolution of convective spatial white noise $\mathcal{U}_i$ with a spatial Gaussian filter kernel $\mathcal{G}$ [52],

$$\psi_i'(\mathbf{x},t) = \int_{\mathbf{V}_s} \hat{A}(\mathbf{x})\mathcal{G}(\mathbf{x}-\boldsymbol{\xi})\mathcal{U}_i(\boldsymbol{\xi},t)\mathrm{d}^3\boldsymbol{\xi} \ , \tag{5.18}$$

with

$$\mathcal{G}(\mathbf{x}-\boldsymbol{\xi}) = \exp\left(-\frac{\pi}{2}\frac{|\mathbf{x}-\boldsymbol{\xi}|}{l_s^2}\right) \ , \tag{5.19}$$

where $\hat{A}$ denotes an amplitude function taken from RANS statistics, whose appropriate scaling yields the desired variance of ψ_i'. $\mathbf{x}$ defines the field coordinates of the vector potential and $\boldsymbol{\xi}$ defines the white noise field coordinates. Furthermore, l_s is an integral turbulence length scale determined from RANS calculations. Finally, the fluctuating velocities, used as an input for the Poisson equation (Equ. (5.16)), can be obtained by taking the curl of the fluctuating potential field $\boldsymbol{\psi'}$,

$$\mathbf{u}' = \nabla \times \boldsymbol{\psi}' \ . \tag{5.20}$$

Calculation of the fluctuating velocities and therefore of the pressure fluctuations are necessary to calculate the auto-spectra and to analyse the two-point statistics, thus to obtain the correlation behaviour as well as the wavenumber-frequency spectra. Due to the used spatial Fourier transform in the method of Hu, this method is limited to Cartesian patches consisting of equidistant cell size for each spatial direction. In the case of an aircraft, input data from CFD is not available in this specific format. Therefore, CFD data in the computation domain has to be further processed to be usable for Hu's method. This process is described in detail in Chapter 5.2.1 together with the selection of appropriate areas for numerical calculations. Beside this, data analysis and first results for the analysed auto-spectra and wavenumber-frequency spectra are presented in Chapter 5.2.2 and 5.2.3, respectively.

5.2.1 Data Preparation Method

In spite of the development of high performance computing (HPC), the CAA method of Hu described in the beforehand Chapter is still a time and resources consuming numerical method compared to CFD calculations. Today, CFD calculations can be easily applied to full aircraft models and results are, thanks to HPC, available within several days. Due to the much higher computational cost of Hu's method, the calculation domain has to be reduced compared to the CFD domain and is therefore limited to small areas. These areas correlate to the areas

on the aircraft, where Kulite windows were installed; their global positions are shown in Figure 2.2. Furthermore, data has to be transferred to Cartesian meshes with equidistant cell size that are not directly available in the CFD solution. To do so, a new mesh adapted to the CAD geometry of the aircraft is generated with ICEM[2]. Afterwards, data from the full CFD calculation are interpolated to the new meshes. Tests were performed in the three Kulite window areas of the aircraft and the new meshes for these areas are visible in Figure 5.11 for the front, mid and aft region in blue, red and green, respectively. Grey meshes above and below the coloured meshes are also used for testing but not treated in detail here. A front view of the bended new mesh is presented in Figure 5.12(a).

In a next step this mesh is rolled off and data is reorganised on a Cartesian

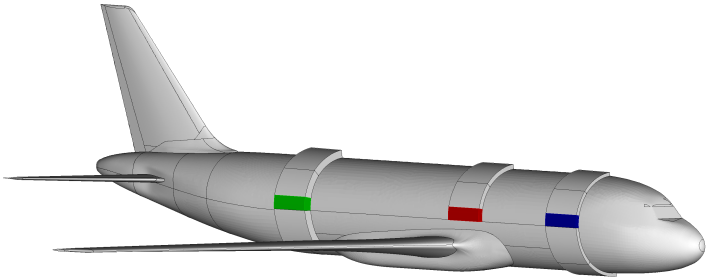

Figure 5.11: Aircraft – Meshes for CAA Patches

mesh. Data structure is kept due to the i, j, k organisation in Tecplot[3] and the reorganisation is automated in a Matlab[4] script. Due to the transformation of the coordinate system, the x-, y-, z-mean flow velocities must be converted to the new system at every node.

Data conversion is depicted in Figure 5.12(b) for the velocity vector. The chosen patch position on the cylindrical part of the fuselage simplifies the conversion to a recalculation of the y- and z-parts of the velocity because the x-part of the coordinate system stays unchanged. As depicted, the 2D velocity vector **u** in Fig. 5.12(b) consists of a u_y and u_z component. These components are converted to a wall tangential that becomes the wall parallel velocity in the Cartesian mesh (u_p) and a wall normal velocity component (u_n) for each node in the mesh. This conversion is realised by means of the wall normal vector of the CAD geometry,

[2]Commercial mesh generator – ANSYS ICEM CFD, Version 14.5
[3]Commercial CFD data visualisation tool – Tecplot 360, Version 2012R1
[4]Commercial technical computing and model-based design software – Matlab, Version R2013b

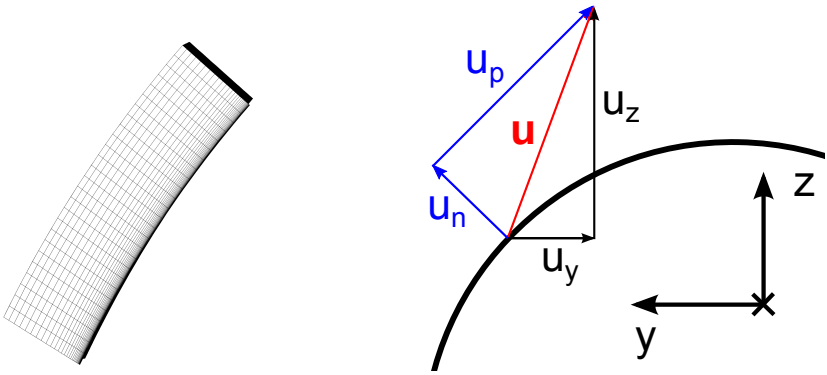

(a) Front Window CFD Patch (b) Coordinate Systems

Figure 5.12: From bended CFD- to Cartesian FRPM mesh

which consists of a N_y and N_z part and yields

$$\mathrm{u}_n = \mathrm{u}_y \cdot N_y + \mathrm{u}_z \cdot N_z \ , \tag{5.21}$$

$$\mathrm{u}_p = \mathrm{u}_y \cdot N_z + \mathrm{u}_z \cdot (-N_y) \ . \tag{5.22}$$

Finally, a Cartesian patch with equidistant cell size is calculated, which is used for the main calculation with Hu's method. To reduce computational costs, it is considered to keep the patch as small as possible and the mesh as coarse as possible. The minima for a calculation are as presented in Figure 5.13, the thickness should be $\approx 1.1{\cdot}\delta_l$, the width as well as the length $\approx 2{\cdot}\delta_l$ and $\approx 4{\cdot}\delta_l$, respectively. Analysis studies showed that the analysable area is somewhat smaller, a constant distance of $\approx 0.5{\cdot}\delta_l$ has to be held to the lateral borders of the patch. In longitudinal direction, a distance of $\approx 1 \cdot \delta_l$ to the borders has to be met. Finally the green marked area in Fig. 5.13 gives satisfactory results for auto-spectra and wavenumber-frequency spectra, whose results are presented in the following two Chapters.

5.2.2 Auto-Spectra Prediction

CAA calculations, with the beforehand described method, were performed for the coloured marked areas in Figure 5.11. In this Chapter, results for the numerical estimated auto-spectra are presented for the front and aft regions. Auto-spectra are calculated at several locations at the bottom surface of the different patches

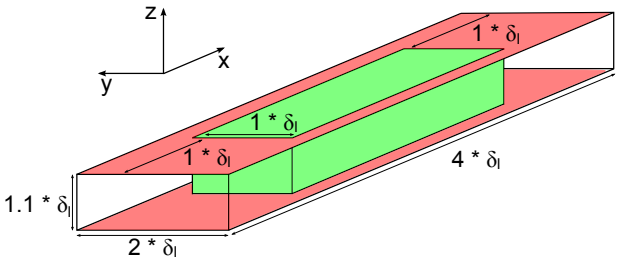

Figure 5.13: Cartesian CAA Patch and minimal dimensions

– measurement positions are represented by virtual microphones. These virtual microphones record time dependent pressure fluctuations, similar to microphone recordings on a real aircraft. The time signals length are $t = 0.4$ s for both cases and the calculation time 11 days and 25 days on 5 CPU's of a standard state of the art LINUX workstation for the front and aft patch, respectively. Time data are equally analysed and the frequency dependent auto-spectra are compared in Figure 5.14. Validation auto-spectra, already presented in Figure 2.13 are used for comparison and plotted in blue for the front region (Fig. 5.14(a)) as well as in green for the aft region (Fig. 5.14(b)). Numerically calculated auto-spectra are plotted in pink and red for the front and aft region, respectively. A row of virtual microphones located in the middle of each patch is analysed and plotted as thin lines, the mean value is shown as a thick line. The presented numerical predictions reflect the measurements quite well. Absolute levels fit over a large frequency band and the position of the maximum is well represented. Especially in the low and high frequency range, measurement and prediction diverge. Explanations for this behaviour are manifold, however, the two main influencing factors are discussed in the following.

Firstly, following the approach of Hu et al. in [52], the turbulence-turbulence term in the Poisson equation (Equ. (5.16)) was neglected in the calculations to minimise computational costs (neglect reduces computational costs by 50 %). According to Hu et al., the turbulence-turbulence term contributes mainly to the low frequency range of the auto-spectra. It causes a maximum error of 3 dB at 100 Hz, decreasing to zero at $\approx$ 900 Hz, shown for an auto-spectrum having its maximum at $\approx$ 1 kHz (cf. [52]). Taking into account the turbulence-turbulence term of the Poisson equation should therefore solve the low frequency deviation of both results and increase the spectral levels.

Secondly, the mismatch of results in the high frequency region is caused by a

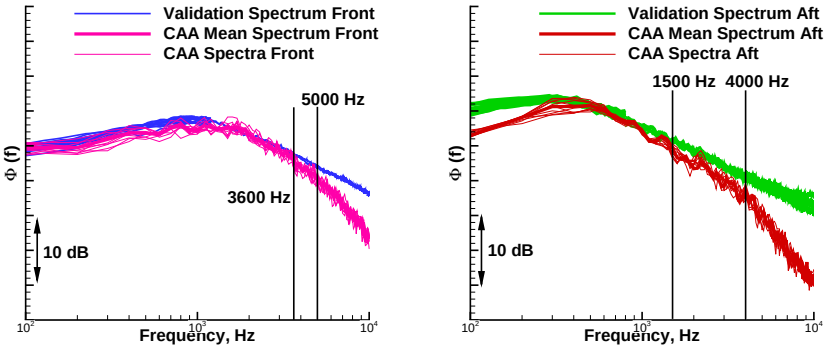

(a) Front area

(b) Aft area

Figure 5.14: Validation auto-spectra: CAA vs. Measurements

lack in reconstructed turbulence kinetic energy in the numerical calculation. A comparison between the input kinetic energy from RANS computation and the reconstruction by FRPM is shown in Figure 5.15(a) and 5.15(b) for the front and aft patch, respectively. It is particularly noticeable that the reconstruction in especially the region close to the wall ($< 0.3\ \delta_l$) yields too low values. This effect is also observed by Hu [52] and the reason for erroneous energy reconstruction is explained as follows. On the one hand side, in the inner region the kinetic energy and the length scale change fast. This is not the optimal condition for FRPM kinetic energy realisation, which assumes slowly changing turbulent intensities. On the other hand side, the grid resolution is too coarse to resolve the small turbulence structures. The grid resolution is always a compromise between frequency resolution and computational cost because of the equidistant mesh. FRPM uses a spatial Gaussian filter to generate fluctuating turbulence velocities, which is highly dependent on grid resolution. Hu observed in [54] that the realised Gaussian turbulence velocity spectrum is attenuated in the high frequency region compared to the analytical formulation. Therefore, the roll-off frequency of the realised auto-spectrum is shifted to lower frequencies compared to the analytical spectrum. Again, this is probably caused by the too coarse grid to resolve the fine turbulence structures. More details about this analysis, can be found in [52, 54].
To sum up, the presented method is able to predict auto-spectra within a limited frequency range. For the front area example (cf. Fig. 5.14(a)), results are within

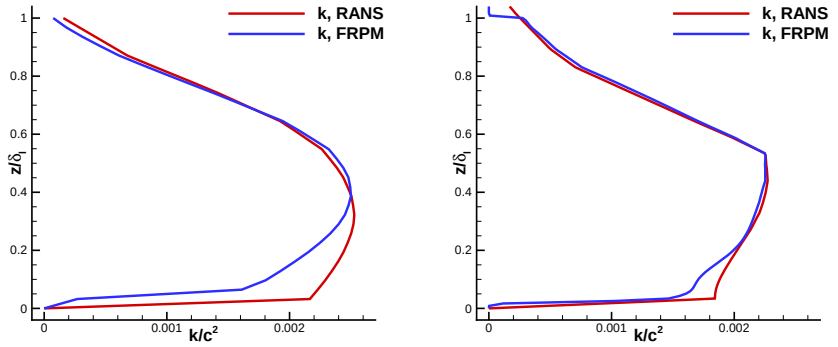

(a) Front area

(b) Aft area

Figure 5.15: Comparison of turbulence kinetic energy – CFD input vs. FRPM reconstruction

an uncertainty of ±1 dB up to 3600 Hz. Above, the deviation of the numerical prediction increases to 1.7 dB at 5000 Hz and increases further with increasing frequency. In the aft region example (cf. Fig. 5.14(b)), a similar behaviour is on hand, from 200 Hz ... 1500 Hz the numerical prediction reproduces the measurement with a maximum deviation of ±1 dB, above the error increases slowly to 1.7 dB at 4000 Hz. Further across, the deviation increases dramatically.

5.2.3 Wavenumber-Spectra Prediction

Beside the auto-spectrum, which represents the energy level at a point, also the two-point statistics can be analysed, to gain information about the time and spacial development of turbulence. In this Chapter, results for calculated wavenumber-frequency spectra ($\Phi(k_x, k_y, \omega)$) are presented for the front aircraft region (cf. Fig. 5.11 (blue)). The calculation is done by taking the spatial Fourier transform of the cross-spectral density, as described in Equ. (3.20). For this analysis, an FRPM calculation with a larger dimensioned patch, compared to the auto-spectra calculations, was performed. Patch dimensions are increased to gain a higher resolution in the wavenumber domain. The final resolution in longitudinal and lateral direction is defined by the length (L_x = 1.22 m) and width

($L_y = 0.306$ m) of the patch as follows

$$\Delta k_x = \frac{2\pi}{L_x} = \frac{2\pi}{1.22 \text{ m}} = 5.15 \text{ m}^{-1} , \tag{5.23}$$

$$\Delta k_y = \frac{2\pi}{L_y} = \frac{2\pi}{0.306 \text{ m}} = 20.53 \text{ m}^{-1} . \tag{5.24}$$

An additional increase of resolution is possible by zero padding, to avoid resolution problems in the analysis. Therefore, the calculation domain was extended by zero padding to spatial extensions of $L_x = 10.98$ m and $L_y = 2.754$ m which yields $\Delta k_x \approx 0.57$ m^{-1} and $\Delta k_y \approx 2.28$ m^{-1}.
During the numerical calculation data were recorded with an array of $77 \cdot 18 = 1386$ virtual microphones and a final recording length of $t = 0.98$ s was achieved. This equals a computation time of 23 days on 8 CPU's. A microphone distance of ≈ 2.4 mm could be realised by the microphone array. Requiring a sampling of 3 microphones per wavelength, frequencies up to ≈ 34.6 kHz can be analysed ($f = \frac{U_c}{\lambda} = \frac{0.7 \cdot 237 \text{m/s}}{2 \cdot 0.0024 \text{m}} = 34562.5$Hz). Beside this, the size of each cell in the FRPM mesh was slightly increased, in comparison to the mesh for auto-spectra calculations, to optimise computation time for the huge mesh. This potentially lowers the quality of the high frequency energy reconstruction, compared to the auto-spectrum calculation in Fig. 5.14(a). Results with high quality are expected to be achievable up to $f \lesssim 3000$ Hz. An analysis of the calculated wavenumber-frequency spectra is presented in Figures 5.16(a) - 5.17(b). Figure 5.16 gives a comparison of wavenumber-frequency spectra for different frequencies from 500 Hz ... 5500 Hz in slices at $k_y = 0$. For this purpose, $\Phi(k_x, k_y, f)$ is normalised to $\int\int \Phi(k_x, k_y, f) = 1$ and the slices at $k_y = 0$ are plotted to represent the maximum of the convective ridge best (located at $k_x = k_\omega = \omega/U_c$). The comparison up to 3000 Hz shows quite satisfying results (cf. Fig. 5.16(a)) when compared to theoretical estimations from literature, like depicted in Fig. 3.3. Especially up to 2000 Hz, the shape of the convective ridge looks physical with a steady slope at the flanks around the convective peak. However for higher frequencies the ridge starts slowly to broaden and the slopes around the peak become unsteady and rough. Consulting data from higher frequencies $f > 3000$ Hz (Fig. 5.16(b)), the shape of the convective ridge looks not physical any more, when compared to theoretical expectations (cf. Fig. 3.3), and the clear peak at k_ω vanishes with increasing frequency. One explanation for this is the erroneous reconstruction of kinetic energy close to the wall, as already discussed in connection with Fig. 5.15(a). Missing small turbulence reconstruction influences the high frequency range and therefore lowers the coherence the higher frequency range, which finally stretches the convective ridge in k_x direction. Beside this, the isotropic turbulence reconstruction, used in FRPM influences the results as well. In real flows,

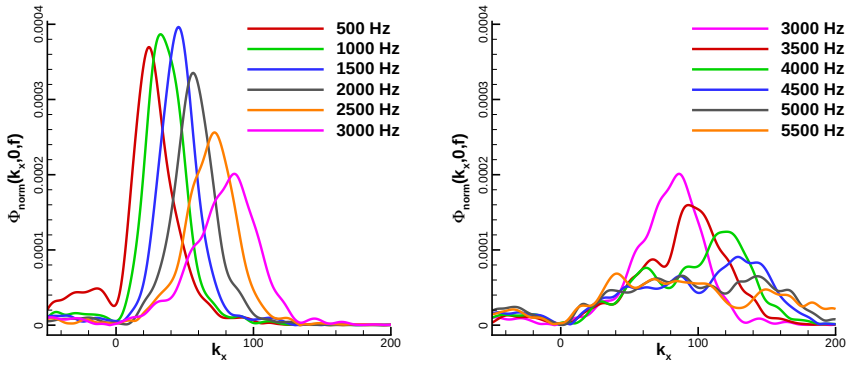

(a) 500 ... 3000 Hz

(b) 3000 ... 5500 Hz

Figure 5.16: Comparison of FRPM wavenumber-frequency spectra – $k_y = 0$, similar to [64]

spatial turbulence stretching in streamwise direction occurs and lowers the width of the convective ridge in k_x direction. Additional, this stretching in flow direction triggers a broadening in k_y direction due to lower coherence. Comparing the convective ridge in slices along $k_x = k_\omega$ in Figures 5.17(a) and 5.17(b), this broadening does not occur. Finally, the turbulence decay in the FRPM calculation influences the shape of the convective ridge in k_x direction as well and could be an additional issue.

To sum up, challenges in the wavenumber-frequency spectra computation have been identified and a quantitative comparison of the spectra is given. A conclusion about the quality of the presented spectra is not possible by direct comparison with measurement data because no comparable data is available. Therefore, a comparison of the structural vibration, calculated with the FRPM wavenumber input is done with SEA and compared with measured vibrations in Chapter 6.

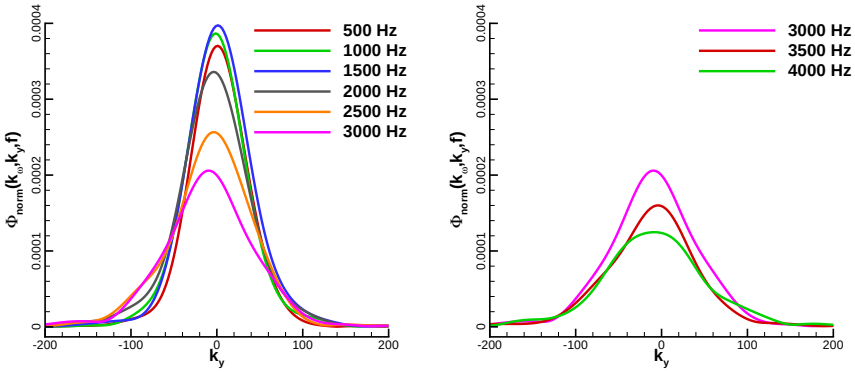

(a) 500 ... 3000 Hz

(b) 3000 ... 4000 Hz

Figure 5.17: Comparison of FRPM wavenumber-frequency spectra – $k_x = k_\omega$, similar to [64]

6 Results and Discussion

This chapter gives a summary and a discussion of the results of this thesis. It is divided in two main parts, on the one hand side with a focus on the TBL excitation in terms of auto-spectra. And on the other hand side, focusing on structural response, at which the influence of different excitation models in terms of auto-spectra as well as wavenumber-frequency spectra on the power input from TBL and the resulting structural vibration (acceleration) is studied. Therefore, this chapter is organised as follows.
Firstly, results of the new auto-spectrum model (cf. Ch. 5.1), are presented in detail and compared with flight test data in chapter 6.1. Secondly, the influence of different auto-spectra models as well as wavenumber-frequency models on the excitation is tested, by coupling to a flat aluminium plate. This calculation is performed in Matlab by following the approach of Graham (compare Ch. 3.3) and by using a commercial software package (VA One) as well. Results are presented in chapter 6.2 and the quantity of comparison is the power input into the excited plate. Thirdly, comparisons of numerically estimated and measured vibrations of a real A320 aircraft structure are performed with the presented excitation models. These results are created by using VA One and industrial SEA models of the A320 from Airbus and their presentation is given in Ch. 6.3.

6.1 CFD based Semi-Empirical Auto-Spectra Prediction Model

In this chapter, results of the new auto-spectrum model, which was presented in Ch. 5.1, are presented in more detail than in the development chapter. The influence of position variation on the whole aircraft, on predicted and measured auto-spectra is done. Beside this, the influence of varying flight level and Mach number is studied, as it was done in the flight test data analysis chapter (Ch. 2.2) for the measurement data only. Predictions are always compared with measurement data. The positions of microphones, used in this chapter, are given in Figures 2.6 and 2.7.

Varying measurement position

In this section, the comparison of data with varying positions on the aircraft is done, similar to the measurement data analysis in chapter 2.2.3. Figures 6.1(a)

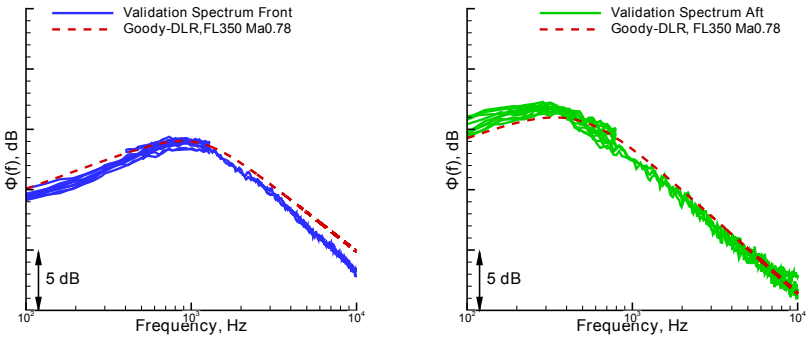

(a) Front area (b) Aft area

Figure 6.1: Goody-DLR auto-spectrum model – Results compared with measured validation auto-spectra in the Kulite window region, similar to [58]

and 6.1(b) show the measured validation auto-spectra for the front and aft aircraft region, as already known from Ch. 2.2.2. In dashed red lines, the respective predictions, made by the Goody-DLR auto-spectrum model are plotted. An accurate collapse of the auto-spectra is achieved with a maximum deviation of ±1 dB for the front area between $f = 100...8000$ Hz; above, the deviation increases slightly up to 1.7 dB at $f = 10$ kHz. For the aft region, the prediction is within the mean variation of the measurement for the complete frequency range $f = 100...10000$ Hz. Therefore, the shape and the absolute levels as well as the position of the frequency maximum is precisely represented by the new model.
Beside this, Figures 6.2(a) and 6.2(b) depict the prediction results in the aft roof fuselage region compared to the measurements on the example of two sensors. Measurement data is partly shown for a limited frequency range, which was discussed in Ch. 2.2.1. Within the plotted frequency range, both predictions, for both sensors fulfill an accuracy of ±1 dB compared to the measurements.
Furthermore, Figures 6.3(a) - 6.3(d) give an overview of the predicted auto-spectra in the aircraft's front region around the Kulite window area (cf. Fig. 2.6(a)) for four positions. Again, the auto-spectrum model is able to reproduce the measurement data within a precision of ±1 dB. However, the very high frequency region

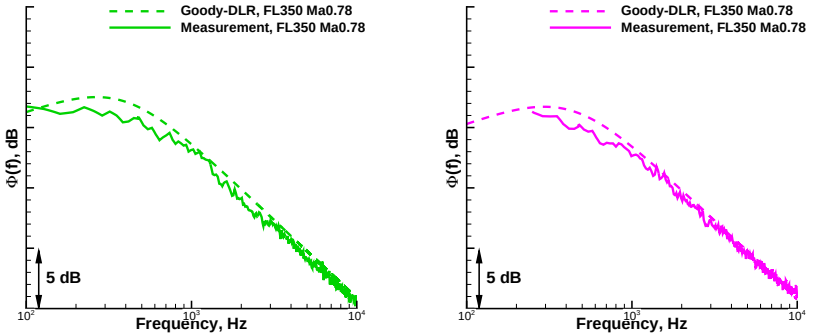

(a) Above of the last Kulite window, FL350 Ma0.78

(b) Above and behind the last Kulite window, FL350 Ma0.78

Figure 6.2: Goody-DLR auto-spectrum model – Comparison of results in A/C aft roof region, similar to [58]

between $f = 8...10$ kHz exhibits a slightly higher deviation of 1.7 dB for the data in Figure 6.3(a).

In addition, data from the aircrafts wing wake region is compared in Figures 6.4(a) - 6.4(d). The model reproduces the measurements again with a precision of ± 1 dB for the presented positions.

Varying flight level and Mach number

Finally, a data comparison for configurations of varying flight level and varying Mach number is performed. For Mach number variation at constant flight level, measurement and prediction results for one front and one aft position are presented in Fig. 6.5(a) and Fig 6.5(b), respectively. The variation of Mach number is Ma = 0.72, 0.78, 0.82. In the front region case, prediction results collapse with the measurements. Therefore, the trends in level variation of increasing auto-spectra levels with increasing Mach number are correctly reproduced. This is also applicable to the aft region example, shown in Figure 6.5(b). However, in the Ma = 0.78 and Ma = 0.82 cases the model overpredicts the measured results by $\approx 1...1.5$ dB in the frequency range $f < 750$ Hz. Nevertheless, deltas between the three flight-cases are correctly reproduced.

A similar behaviour is observable for the flight level variation cases, presented in Figures 6.6(a) and 6.6(b). For the front area, the results of the prediction model

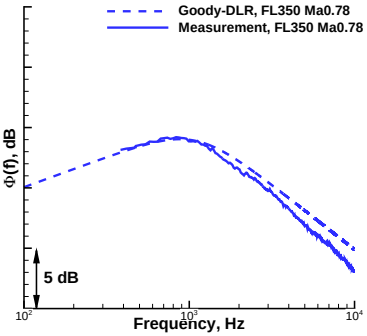

(a) Window plane first position, FL350 Ma0.78

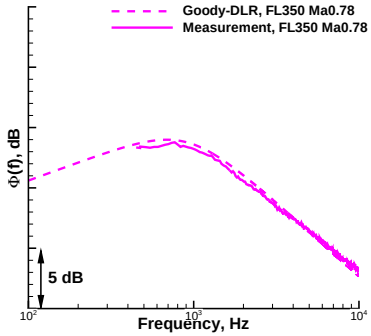

(b) Window plane second position, FL350 Ma0.78

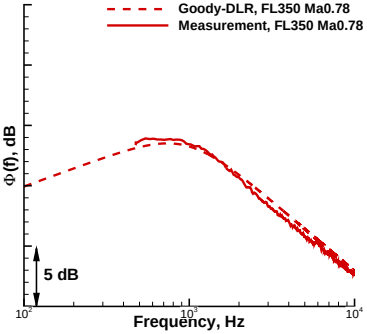

(c) First position below the windows, FL350 Ma0.78

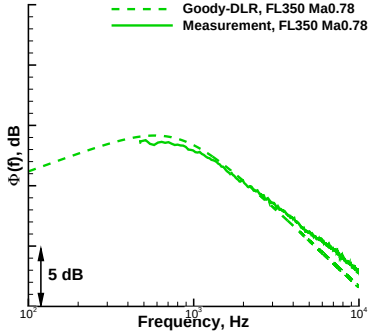

(d) Window plane third position, FL350 Ma0.78

Figure 6.3: Goody-DLR auto-spectrum model – Comparison of results in front A/C area, similar to [58]

and the measurement results collapse. Again, for the aft region, the prediction model overpredicts the levels by 1...1.5 dB in the frequency range $f < 750$ Hz. Above, $f > 750$ Hz, the prediction and measurements collapse. Nevertheless, spectral trends and deltas between the different cases are correctly represented. To sum up, the new GOODY-DLR auto-spectrum model has proven a good reliability within an uncertainty of at most ± 1.5 dB. It is able to reproduce the spectral shape and absolute levels of the measured data. Furthermore, it represents the

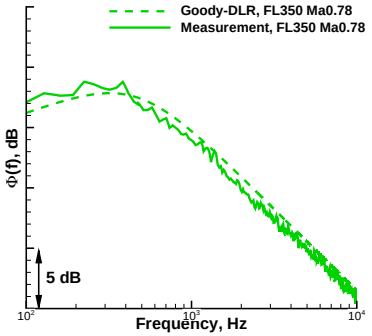

(a) First sensor behind the wing's trailing edge, FL350 Ma0.78

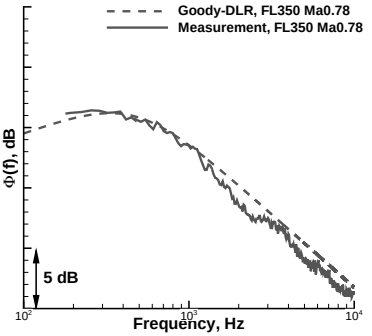

(b) Second sensor behind the wing's trailing edge, FL350 Ma0.78

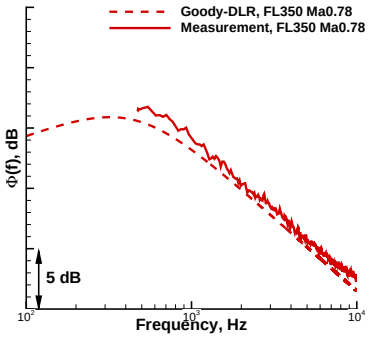

(c) Sensor directly behind Belly fairing, FL350 Ma0.78

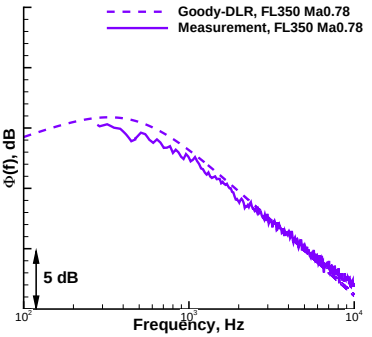

(d) Third sensor behind the wing's trailing edge, FL350 Ma0.78

Figure 6.4: Goody-DLR auto-spectrum model – Comparison of results in the wing wake area, similar to [58]

spectral trends for different flight conditions correctly. The model is limited due to aerodynamic limitations within the flight tests as listed in Table 5.4.

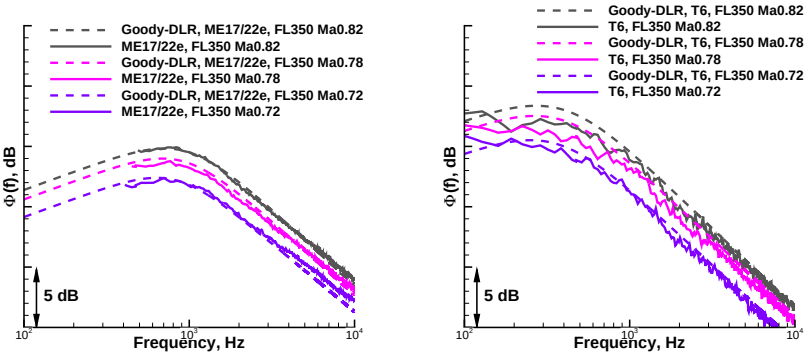

(a) Front area (b) Aft area

Figure 6.5: Goody-DLR auto-spectrum model – Variation of Mach number

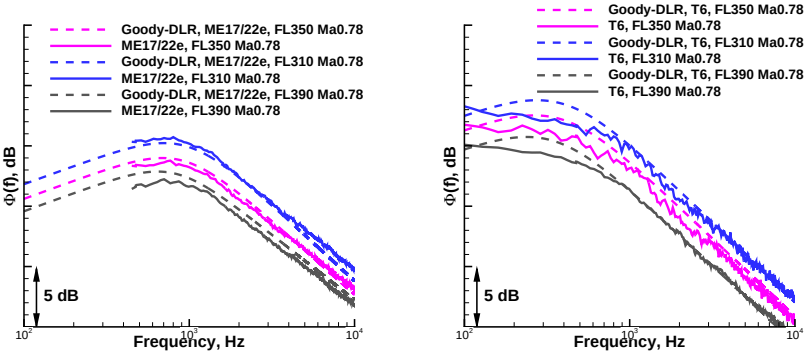

(a) Front area (b) Aft area

Figure 6.6: Goody-DLR auto-spectrum model – Variation of flight level

6.2 Coupling – Flat Plate

In the final application, the TBL excitation models are used to calculate the energy input from TBL into an aircraft structure. From the resulting structural vibration, the interiour cabin noise is calculated. Therefore, knowledge about the importance of the auto-spectrum as well as the wavenumber-frequency spectrum on structural vibration is indispensable. To gain this knowledge, a study with different excitation models applied to a flat aluminium plate with homogeneous mass distribution is performed. This simplification is made instead of applying the excitation models to curved and stiffened aircraft structures. The advantage of this testing is the simplicity of the structural component and therefore the reduction of potential errors due to uncertainties in the complex numerical description of complex real aircraft structures. The influence of changing auto-spectra models by keeping the wavenumber-frequency spectrum constant is analysed in chapter 6.2.1. Beside this, in chapter 6.2.2 the influence of different wavenumber-frequency spectra is studied. Within these chapters, the influence of different aerodynamic input into the models is discussed as well. A sketch of the used SEA model from VA One is shown in Figure 6.7, with the TBL coupling symbol included. The plate consists of aircraft like length and width (cf. Table 6.1), but thicker than standard fuselage skinfields to be sub- and supercoincident with the TBL and plates wavelength.

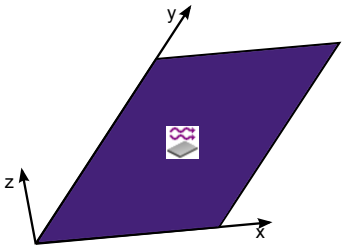

Figure 6.7: Sketch of plate model for excitation testing

Table 6.1: SEA plate dimensions

L_x	0.6 m
L_y	1.6 m
t	5 mm
m	12 kg

6.2.1 Varying Auto-Spectra

In this variation test, the flat plate model is excited with different auto-spectra models at typical aircraft cruise flight conditions. The wavenumber-frequency

spectrum remains the same for each of the tests, in which the model of JOLLY is chosen (cf. Equ (3.38)). Varying auto-spectra models are taken from the pool of models presented in chapter 3.1. In detail, the models from COCKBURN & ROBERTSON (Ch. 3.1.2), EFIMTSOV 1 (Ch. 3.1.4), GOODY (Ch. 3.1.7) and KLABES (presented in Ch. 5.1 and until now named as the DLR-GOODY model) are compared, to cover the huge variety of different auto-spectra shapes. Ambient conditions are set to FL350 and $U_e = 239.4$ m/s at an x-position of $x = 7.4$ m, yielding a TBL thickness of $\delta_l = 6.1$ cm.
Figure 6.8(a) shows the auto-spectra, used as exciting forces on the flat plate in this test. Calculated results of the plate's response are plotted in Figure 6.8(b) in terms of excitation power input. The excitation power S_t (Equ. (3.70)) is the power, the system (plate) is able to receive from the TBL due to its physical properties. Comparing the auto-spectra and the respective plate responses, it is obvious that huge differences in the auto-spectra are directly visible in the plate response. For example, a difference of $\Delta\Phi = 10$ dB at $f = 200$ Hz (Fig. 6.8(a)) between the auto-spectrum of COCKBURN & ROBERTSON and EFIMTSOV 1 is visible as a factor of 10 between the calculated power inputs (Fig. 6.8(b)) of these two cases in the 1/3-octave band of $f = 200$ Hz.

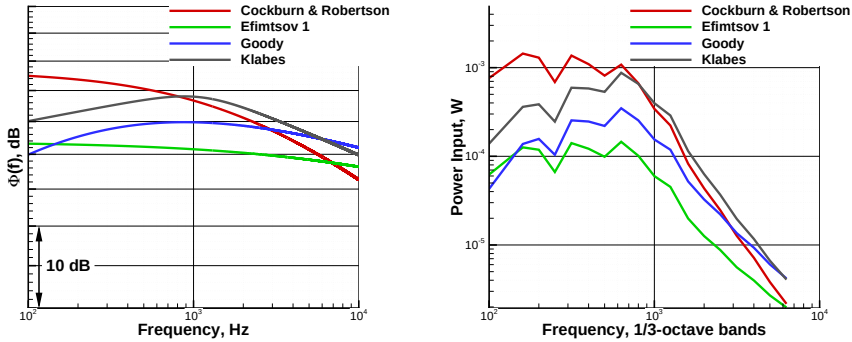

(a) Auto-Spectra (b) Power Inputs

Figure 6.8: Power Inputs due to different auto-spectra

6.2.2 Varying Wavenumber-Frequency Spectra

In a next step, the importance and the influence of different wavenumber-frequency spectra on the plate response is studied, using the models of Corcos (Ch. 3.2.1), Jolly (Ch. 3.2.2), Efimtsov (Ch. 3.2.3), Smol'yakov & Tkachenko (Ch. 3.2.4), Smol'yakov (Ch. 3.2.5) and Chase (Ch. 3.2.6). Whereupon, the Corcos model can be stated as the origin of models and the Jolly as well as the Efimtsov are modifications, including more information of the turbulent boundary layer, e.g. the boundary layer thickness. However, these three models are following the same strategy of describing the flow, by dividing it in a streamwise and a cross stream component. Due to that, the characteristic rhombic shape of the spectra follows, as already discussed in chapter 3.2. Finally, calculations with the Smol'yakov and Chase models are performed, as representatives of the elliptical shaped wavenumber-frequency models. The Klabes auto-spectrum model (Fig. 6.8(a)) is used as the point excitation for all wavenumber-frequency models. Results of the applied Corcos, Jolly and Efimtsov wavenumber models are presented in Figure 6.9(a). The power input into the plate, calculated with the Cor-

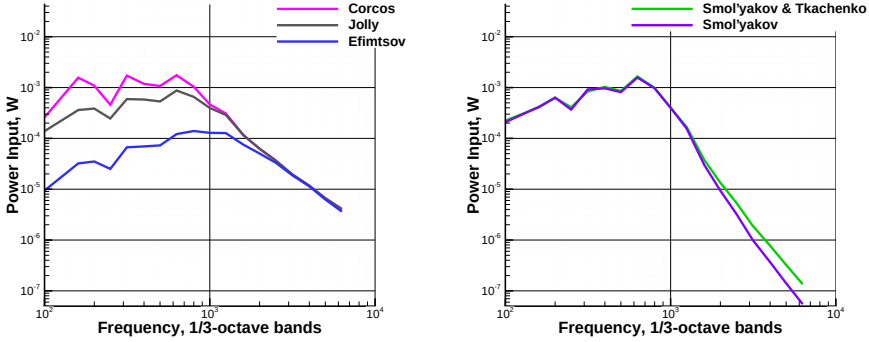

(a) Rhombic models

(b) Smol'yakov elliptical models

Figure 6.9: Power Inputs due to different wavenumber-frequency spectra

cos and Jolly model look similar in shape, only the levels for the 100...1000 Hz 1/3-octave bands are higher for the Corcos model excitation. The maximum of power input is centered around the 630 Hz 1/3-octave band. The higher values below $f < 1000$ Hz for the Corcos excitation can be explained with the different absolute levels of the convective ridge between the Corcos and Jolly models, by

being nearly unchanged already at small distances away from the convective peak. This can be seen in Fig. 3.11(b). Furthermore, differences between the two models are negligible above $f > 1000$ Hz. Beside this, the power input calculated with the EFIMTSOV model is much lower, compared to the two before mentioned models. This behaviour can be explained by the level of the convective peak again, which is lower than in all other models (cf. Fig. 3.11(b)).
Differences in the frequency dependent power input can be explained by looking into GRAHAM's method. The power input level is dependent on the overlap of the TBL wavenumber-frequency model and the eigenmodes of the structure. The better the overlap, the higher the value of the modal excitation term (Φ_{mn}, cf. Equ. (3.73)), which follows in a higher power input ($S_t(\omega)$, cf. Equ. (3.70)). A sketch of this principle, according to GRAHAM, is given in Figure 6.10. Within the band of $f = 630$ Hz, the TBL wavenumber is $k_\omega = \frac{\omega}{U_c} = \frac{2\pi \cdot 630\ Hz}{0.8 \cdot 237 m/s} = 20.88\ m^{-1}$. In that frequency band, four eigenmodes are existent with $m = 4$ at $k_m = \frac{m \cdot \pi}{L_x} = \frac{4 \cdot \pi}{0.6\ m} = 20.94\ m^{-1}$, being slightly shifted in the k_y direction, by a maximum of $n = 5$. The frequency of coincidence is achieved at $f = 630$ Hz, which is also confirmed by the results of VA One. In the higher frequency range ($f > 1500$ Hz) the overlap of TBL and eigenmodes (Fig. 6.10) is lowered and therefore the energy input as well. Data about the eigenmodes of the plate are extracted from VA One for this analysis. Figure 6.9(b) gives a comparison of the two SMOL'YAKOV

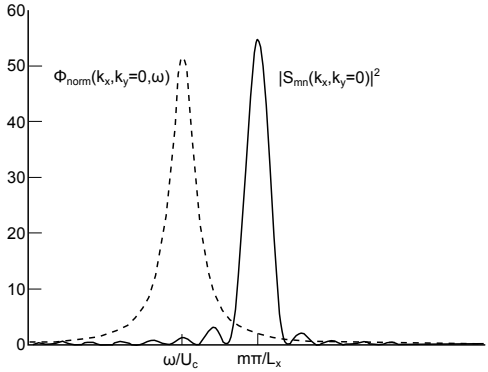

Figure 6.10: Overlap of TBL and eigenmode in longitudinal (k_x) direction

models and the impact on the power input. No tremendous differences are visible, however, small variations are visible above $f > 2000$ Hz. This is according to expectation, because there are no significant differences in the models in Figure 3.11. Furthermore, the comparison of the CHASE models in Fig. 6.11(a) show a parallel

shift of the power inputs to higher levels, when changing from the CHASE 1 to the CHASE 2 model. One reason is again the higher level of the convective peak

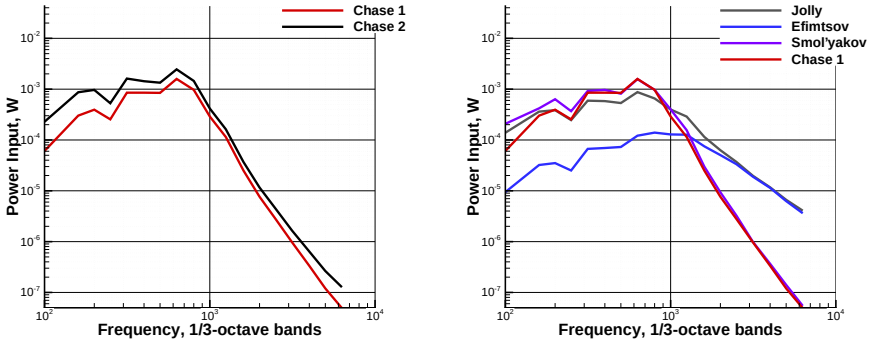

(a) Chase elliptical models

(b) All model families

Figure 6.11: Power Inputs due to different wavenumber-frequency spectra

(cf. Fig. 3.11(b)), and a second reason could be the broader extension of the wavenumber spectrum in k_x direction (cf. Fig. 3.11(a)). Contrary is the shape in k_y direction, here the CHASE 2 model is tapered, compared to the CHASE 1 model. Finally, a comparison of all model families is given in Figure 6.11(b), which shows a large variation between the calculated power inputs. At low frequencies, $f = 100$ Hz, results differ by a factor of 3.5 (CHASE 1 vs. SMOL'YAKOV). This deviation decreases and is low between $f = 250...1500$ Hz for all models, except for the EFIMTSOV model, which still differs and stays different up to $f = 2000$ Hz. Above frequencies of $f > 1500$ Hz differences are increasing, dependent on the model family. The rhombic models deliver higher power input levels, while the elliptical models provide lower levels. These differences are increasing up to a factor of 55 between the estimations of JOLLY and CHASE 1 at the 1/3-octave band of $f = 5000$ Hz. Nevertheless, all models show a consistent trend of low coupling of energy for TBL at high frequencies ($f > 2000$ Hz). This shows that the modal approach of calculating the power input, is highly sensitive on the chosen wavenumber-frequency model. Here, the absolute levels of the peak values as well as the shape in streamwise and cross stream direction are essential. As a last test, the influence of errors in the determination of the convection velocity U_c is studied on the example of the JOLLY model with a variation of ± 10 m/s. Results are presented in Figure 6.12. The influence is up to $\Delta_{max} = \pm 1.3$ dB

for the $f = 1250$ 1/3-octave band. Below and above differences decrease and below $f < 400$ Hz no differences are visible. This leads to the conclusion that the

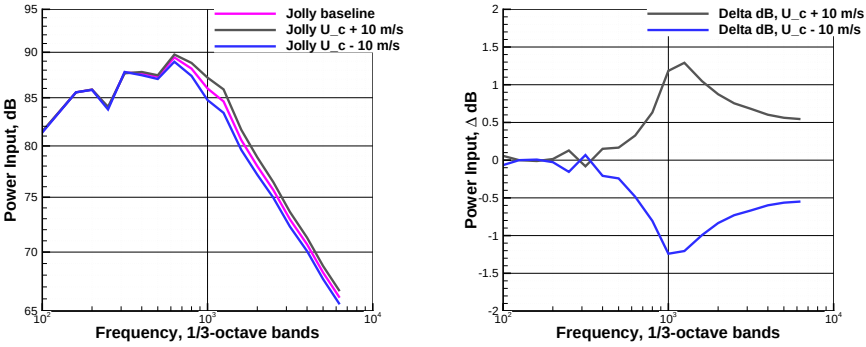

(a) (b)

Figure 6.12: Power Inputs due to variation in U_c applied to the Jolly model

wavenumber-frequency spectra and the aerodynamic input parameter are as important as the auto-spectra for the correct estimation of the power input into a structure and finally the plate's vibration. The wavenumber-frequency models are not further investigated within this thesis.

6.3 Coupling – Aircraft

Finally, the application of the new auto-spectrum model as well as semi-empirical and numerical wavenumber-frequency spectra to real aircraft structures is presented in this chapter. According to the Kulite window measurement regions (cf. Fig. 6.13), SEA models are developed for the respective regions, mainly by Callsen[5] and supported by the work of Teschner [85] and Klabes [60]. The SEA models always stretch across four frame bays and are sketched in Fig. 6.13 together with the Kulite windows and their global position on the aircraft. Furthermore, the different naming of the SEA subsystem regions is presented. During the collaboration with Airbus, detailed analysis were performed for all aircraft models. In this thesis, only results for the front model from floor to floor are

[5] Airbus Acoustic Engineer

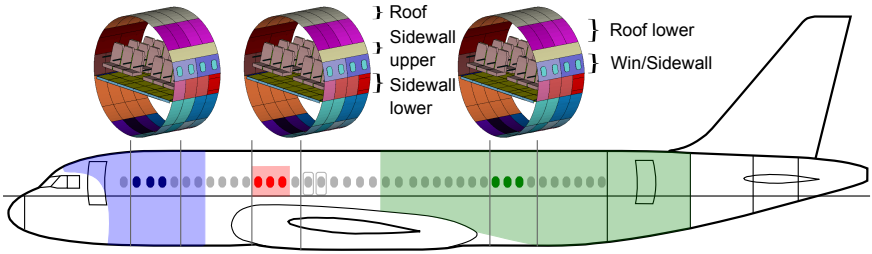

Figure 6.13: Sketch of ATRA with SEA model and Kulite positions, similar to [64]

presented in the following.
First of all, it is important to have a rough overview of the frequency limitations of SEA, when applied to aircraft structures. The level of confidence is high between $f = 400...5000$ Hz, especially below $f < 400$ Hz, the confidence is lower due to global modes, until the modes are becoming more local and therefore appropriate for the SEA subsystems. Therefore, normally Finite Element methods (FEM) are employed in the lower frequency range, delivering results of high confidence level. However, a coupling of TBL models with FEM is not yet possible. Beside this, the structure modelling of reduced ribbed panels for the fuselage in SEA could cause indefinite inaccuracies. Nevertheless, the modelling was done by Airbus best practice.
In a first step, an analysis similar to the analysis in the beforehand section is done. Therefore, the influence of different wavenumber-frequency models is analysed on the structural vibration of the *Roof* subsystem. This analysis is presented in Figures 6.14(a) ... 6.16(b). In all plots, 0 dB is the median value of the measured acceleration, while all other data is plotted in Δ dB to this value. The grey line gives the scatter band of the flight test data. Furthermore, all wavenumber-frequency models are calculated with the actual aerodynamic parameters from CFD and the auto-spectrum input is calculated with the KLABES model (cf. Ch. 5.1). Therefore, errors due to the auto-spectrum model are negligible. The procedure for the comparison of the models is that the rhombic models are tested first. Secondly, the best performing rhombic model is retained and compared with the results from elliptical models. Thirdly, the best models of both families are compared with results from FRPM and with an adapted Efimtsov model.
Figure 6.14(a) shows the results for the applied JOLLY, CORCOS and EFIMTSOV original models. Results are plotted for the $^1/_3$-octave bands from $f = 100...5000$ Hz. From $f = 100...400$ Hz, the EFIMTSOV model shows the lowest deviation from flight test data. Whereas the JOLLY and CORCOS models show huge differences to the

measurements. In the mid frequency range from $f = 500...1600$ Hz, this effect is inverted and the Efimtsov model gives results outside the measured scatter band. The Corcos model shows slightly higher levels than the Jolly model, which is according to expectation (cf. Fig. 6.9(a)). Finally, in the high frequency range $f = 2000...5000$ Hz all three models deliver similar results, which is also expected from the study in the beforehand section (Ch. 6.2). A further comparison

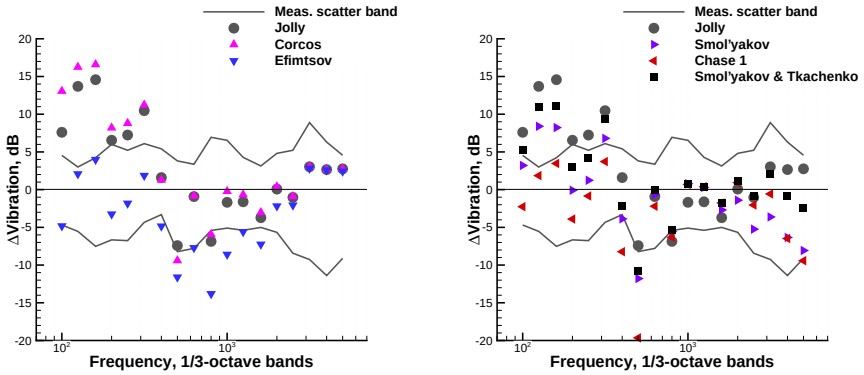

(a) Jolly vs. Corcos vs. Efimtsov

(b) Jolly vs. Smol'yakov vs. Chase 1 vs. Smol'yakov & Tkachenko

Figure 6.14: Comparison of structural vibration due to different wavenumber-frequency models – Roof

with the Jolly, Smol'yakov, Chase 1 and Smol'yakov & Tkachenko models is presented in Fig. 6.14(b) for the *Roof* subsystem as well. The Smol'yakov and Chase 1 models produce equal results in the mid to high frequency range, $f = 500...5000$ Hz. While they differ in the low frequency range. Also the Smol'yakov & Tkachenko model results are plotted and give satisfying results, by generating the lowest offset from the measurements for the whole mid to high frequency range. Only in the low frequency range below $f < 400$ Hz the Smol'yakov & Tkachenko model results are outside the measured scatter band. Finally, the Jolly as well as the Smol'yakov & Tkachenko models create best results as representatives of the rhombic and elliptical models, respectively. Therefore, further comparisons are only performed with these two models.
Furthermore, a wavenumber-frequency spectrum, fully numerical calculated with FRPM (cf. Ch. 5.2) is applied to the SEA model as well and presented in Fig. 6.15(a). The results, calculated with the FRPM model give satisfying re-

sults within their validity range, which was estimated to be up to $f < 3000$ Hz, in chapter 5.2.3. This assumption can be confirmed by the predicted vibration results with FRPM wavenumber-frequency input, because the vibration levels increase above $f > 2500$ Hz abnormally. Beside this, an adapted Efimtsov

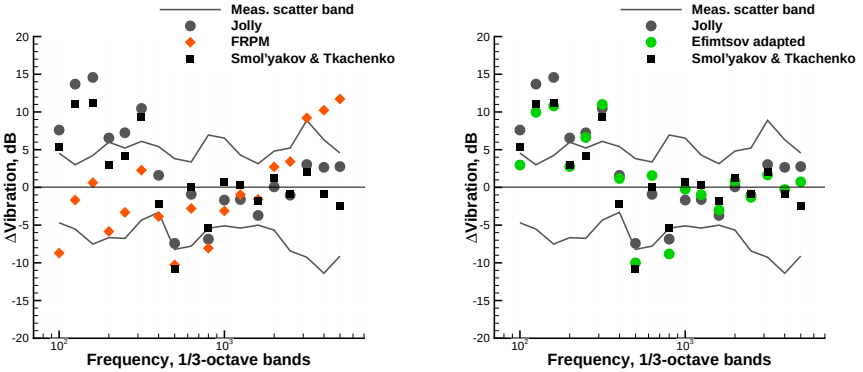

(a) Jolly vs. Smol'yakov & Tkachenko vs. FRPM

(b) Jolly vs. Smol'yakov & Tkachenko vs. Efimtsov adapted

Figure 6.15: Comparison of structural vibration due to different wavenumber-frequency models – Roof

wavenumber-frequency model is also applied to the SEA model. This model is modified according to the work of Haxter [45], who fitted the model parameters ($a_1 ... a_7$) in a way that the model coherence length collapse with the measured coherence length from flight test data. A comparison of the structural vibrations shows a good reproduction of the measured vibrations from $f = 400...5000$ Hz in Figure 6.15(b) with some exceptions at $f = 500$ Hz and 800 Hz. In the frequency range below, estimated vibration data deviate from the measurements, like the results from all other semi-empirical wavenumber-frequency models do, except the original Efimtsov model in Figure 6.14(a). Comparing both models, the FRPM and the adapted Efimtsov, in Figure 6.16(a), both models give a good estimate within different frequency ranges. The FRPM model is satisfactory between $f = 100...2500$ Hz and the adapted Efimtsov between $f = 400...5000$ Hz. Also the plotted results from the Smol'yakov & Tkachenko model are satisfactory between $f = 200...5000$ Hz, predictions lie inside the measured scatter band. Haxter showed in [45] that the coherence length of the Smol'yakov & Tkachenko model collapse with the measured coherence length. Including as well

the Jolly model in this group in Fig. 6.16(b), the model behaviour is comparable with the other models (except FRPM) between $f = 400...5000$ Hz. Again, the predicted levels are too high below $f < 400$ Hz, while this phenomenon cannot be observed with the FRPM model. This leads to the assumption that especially the rhombic wavenumber-frequency models (Corcos, Jolly, Efimtsov) have drawbacks in the low frequency range ($f = 100...400$ Hz).

In the next Figures 6.17(a) ... 6.18(b), the measured vibrations of all other subsys-

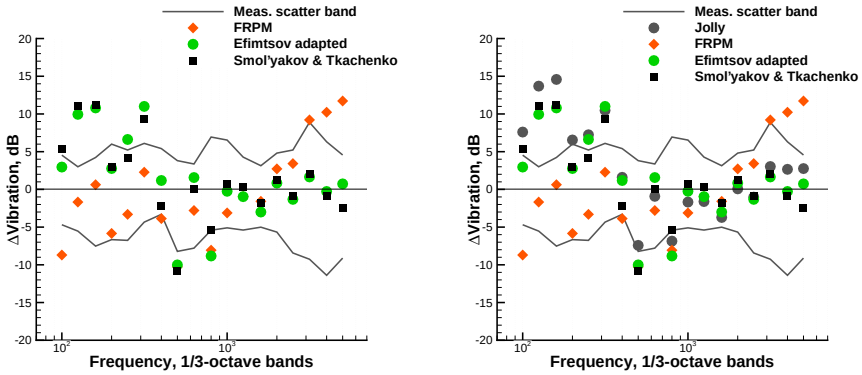

(a) Efimtsov adapted vs. Smol'yakov & Tkachenko vs. FRPM

(b) Jolly vs. Smol'yakov & Tkachenko vs. Efimtsov adapted vs. FRPM

Figure 6.16: Comparison of structural vibration due to different wavenumber-frequency models – Roof

tems are compared to the predictions of the Jolly, FRPM, adapted Efimtsov and Smol'yakov & Tkachenko models. The results for the *Roof lower* subsystem (Fig. 6.17(a)) show similar behaviour than the *Roof* subsystem. Different models are valid within different frequency ranges. FRPM: $f = 125...2500$ Hz, Efimtsov adapted: $f = 400...4000$ Hz, Smol'yakov & Tkachenko: $f = 400...5000$ Hz and Jolly: $f = 400...3150$ Hz (compare also Tab. 6.2). This model validity range is similar for the next subsystem (*Sidewall upper*), shown in Fig. 6.17(b). Beside this, in the two firstly shown subsystem results (*Roof*, *Roof lower*), huge deviations in the 1/3-octave bands of $f = 400$ Hz and $f = 800$ Hz are visible. This behaviour is assumed to be an artefact of the ribbed panel subsystem modelling, the frame distance and therefore the dimensions of the subsystem in SEA. The subsystem *Sidewall upper* does not show this effect, however, it is modelled differently in size in SEA. Nonetheless it may be noted, that the FRPM results show least scatter

Lastly, the *Window / Sidewall* as well as the *Sidewall lower* subsystems are com-

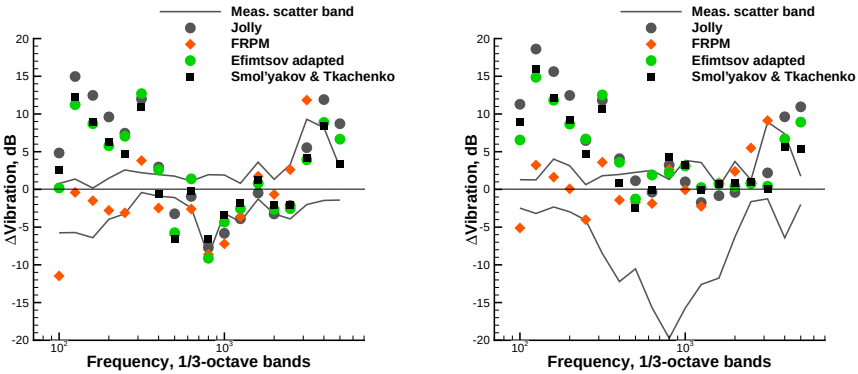

(a) Roof lower

(b) Sidewall upper, similar to [64]

Figure 6.17: Comparison of structural vibration – Jolly vs. Smol'yakov & Tkachenko vs. Efimtsov adapted vs. FRPM

pared in Figures 6.18(a) and 6.18(b). The *Sidewall lower* subsystem in Fig. 6.18(b), shows again similar results than the subsystems before. Figure 6.18(a) gives a slightly different picture. All wavenumber-frequency models calculate vibration levels within the measured scatter band from $f = 160...1000$ Hz (FRPM: $f = 100...1000$ Hz). Above, all models overpredict the measurements except the FRPM model, which again indicates least scattering among all models. The *Window / Sidewall* subsystem is the most complex fuselage area because of the integration of passenger windows. Therefore, it is not just an aluminium structure, stiffened uniformly with frames and stringers. The observed behaviour leads to the assumption that the modelling of the subsystem in SEA causes the observed deviation in the results and the different behaviour as observed for the other subsystems.

To sum up, in this chapter, a comparison of numerically estimated and measured structural vibrations was given for an Airbus A320 fuselage in the front region. The calculation is done with the SEA software VA One, applying the auto-spectrum model developed in this thesis and several wavenumber-frequency spectra. All subsystems were reviewed separately and a clear picture of the applicability of different models is obtained. Their validity range is summed up in Table 6.2.

Both rhombic models, the adapted Efimtsov and Jolly, show gaps below

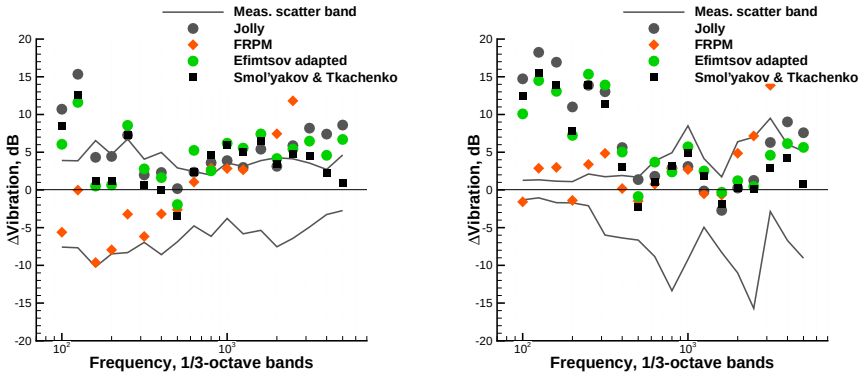

(a) Window / Sidewall, similar to [64]

(b) Sidewall lower

Figure 6.18: Comparison of structural vibration – Jolly vs. Smol'yakov & Tkachenko vs. Efimtsov adapted vs. FRPM

Table 6.2: Frequency limits of different wavenumber-frequency models

Model	f_{min}, Hz	f_{max}, Hz
Jolly	400	3150
Smol'yakov & Tkachenko	400	5000
Efimtsov adapted	400	5000
FRPM (depending on num. resolution)	100	2500

$f < 400$ Hz. This is remarkable because the adapted Efimtsov model is fitted to measurement data, which may indicate that there are general inaccuracies in the rhombic modelling approach. Contrary to this, the Smol'yakov & Tkachenko model, which is an elliptical model performs slightly better in the low frequency range and is able to estimate better results than the two before mentioned models. This assists the assumption of the drawbacks in the low frequency range of the rhombic models. Furthermore, the Smol'yakov & Tkachenko model performs accurate above $f > 400$ Hz. It is remarkable for this model because it is not especially fitted to some flight test measurement data, but the original model from literature is used with aerodynamic input from CFD. As the last model, the full numeric approach with FRPM was presented, which delivers satisfying results for a wide frequency range. It is assumed that this model, by solving the already

discussed numerical challenges, has the potential to increase its validity for the whole frequency range.

7 Conclusion and Outlook

Summary

This thesis was performed in the context of aircraft cabin interiour noise and in detail focusing on the fuselage structural excitation by turbulent boundary layer (TBL) flows at typical cruise flight conditions. Aircraft at cruise flight are flying at high Mach numbers, typically between Ma = 0.78 ... 0.85, dependent on the type and mission of the aircraft. At these flight conditions, the flow around the aircraft's fuselage is a turbulent flow with high turbulence intensity. The eddies within the TBL cause pressure fluctuations on the fuselage and therefore the fuselage receives energy and starts to vibrate. This vibration is inter alia dependent on the flow velocity and thus the strength of the turbulent boundary layer as a source for cabin acoustics. For today's state of the art aircraft the TBL is the dominating source, due to advanced low-noise technologies of modern engines. Because of this development, for aircraft manufacturers like Airbus, it is important to understand the TBL as a source for cabin acoustics and being able to estimate the structural excitation of the whole fuselage. Especially in an early design stage it is important to be able to estimate the noise level of the design and optimise e.g. the shape of an aircraft from the acoustical point of view. TBL estimations in areas on the aircraft subjected to disturbed flows, by integration effects like the junction of wing and fuselage or changing fuselage diameter were not possible with today's semi-empirical methods. For the prediction, knowledge about the strength of the TBL and the development over space and time is necessary, which is described by the auto-spectrum and the wavenumber-frequency spectrum, respectively.
Therefore, the objective of this thesis was to close this gap. Today's available auto-spectra prediction model are not sufficient enough to do so and therefore, an existing semi-empirical model was further developed to tackle these challenges after reviewing available models in the literature. The main technological innovation of the new auto-spectrum model is, taking aerodynamic parameters of the flow from computational fluid dynamics (CFD) calculations instead of calculating it with formulae, mostly developed from measurements on flat plates. Besides, it was found that the turbulence kinetic energy (TKE) is a main quantity, driving the auto-spectrum and thus it was included in the new model. This new model

is validated with measured auto-spectra from flight tests, performed on the Advanced Technology Research Aircraft (ATRA) of the German Aerospace Centre (DLR), an Airbus A320. Therefore it is valid in a rather large parameter space, covering the operational range of a short- to medium-haul aircraft. The analysis of the validation data base was also performed within this work.
In parallel, a full numerical approach to estimate the auto-spectrum as well as the wavenumber-frequency spectrum was executed by making use of the Fast Random Particle-Mesh Method (FRPM) of the DLR. This approach is based on the synthetic reconstruction of turbulence over space and time, using CFD data input. The FRPM approach showed being able to estimate auto-spectra as well as wavenumber-frequency spectra in selected areas of high quality. Currently, the only drawback is a frequency limitation to high frequencies, especially visible in the wavenumber spectra over $f > 2500$ Hz.
Beside these modelling activities, rhombic and elliptical wavenumber-frequency models from literature were reviewed and the effect on a flat plate's vibrational response was studied. This study was conducted by using the method of Graham [41], implemented in Matlab and by a commercial implementation in a Statistical Energy Analysis (SEA) software package. Both approaches showed equal results for the flat plate test.
Finally, the developed auto-spectrum model as well as the different reviewed wavenumber spectrum models, also the FRPM wavenumber spectrum and a model fitted to analysed flight test data were applied to the real aircraft, by using SEA. For the SEA computations the commercial software VA One was employed with Airbus A320 SEA models used for research and development at Airbus. Fuselage vibration data, estimated with these models was finally compared with measured structural vibrations from flight tests in different areas of the aircraft. Estimated structural vibrations gave a good collapse with the measured accelerations, but also showed challenges for different wavenumber-frequency models in distinct frequency ranges. Especially in the low frequency range semi-empirical models tend to deviate from measurements. In the mid and high frequency range reliable models could be identified. However, SEA modelling of fuselage components also has its limits and the confidence in the structural modelling has to be independently analysed.

Outlook

Suggested tasks for future work are manifold.
Firstly, the enhanced auto-spectrum model should be further developed and its validity range should be further extended by verifying it with additional available

flight test data. This extension refers to flight speed and altitude on the one hand side and on the other hand side to pressure gradients. The limits of the model should be further shifted into areas with high favorable as well as adverse pressure gradients as they occur on the cockpit of an aircraft.
Secondly, the field of semi-empirical wavenumber-frequency spectra should be further studied and an approach, similar to the auto-spectrum modelling in this thesis should be followed. This means, that an enhancement of the wavenumber-frequency models, based on CFD input data should be followed. It is suggested to move on with the elliptical Smol'yakov & Tkachenko model [79] because this model performed well during the tests. However, this model is very complex in its description and difficult to access. Therefore, it is also possible to start with a more handy model of the rhombic model family and it is suggested to use the Efimtsov model [20]. The Efimtsov model showed a good adaptability to flight test data and produced satisfactory results as well.
Thirdly, it is suggested to put some effort on the numerical tools as well. The FRPM method showed a great potential and the illustrated high-frequency issues in the test cases are assumed to be solvable. This can be done by increasing the computational mesh resolution, which directly addresses the necessity of parallel computing for the method to decrease computation time. Furthermore, considering the anisotropy of the flow could improve the accuracy of the method, which is already under investigation. The same is true for computational speed by means of parallelisation of the FRPM. Finally, the great advantage of this method is its applicability in nearly every region on an aircraft.

Bibliography

[1] Alaoui, M.; Gloerfelt, X.; Collery, O.; Etchessahar, M. *Effect of pressure gradients on turbulent boundary layer vortical structures and wall-pressure fluctuations.* AIAA paper 2015-3116, June 2015.

[2] Bendat, J.S.; Piersol, A.G. *Measurement and Analysis of Random Data.* John Wiley & Sons, Inc., 1966.

[3] Bies, David Alan. *A review of Flight and Wind Tunnel measurements of Boundary Layer Pressure Fluctuations and induced Structural Response.* NASA Langley Research Center, CR 626, 1966.

[4] Blake, William K. *Mechanics of Flow-Induced Sound and Vibration, Volume I, General Concepts and Elementary Sources.* 1986.

[5] Blake, William K. *Mechanics of Flow-Induced Sound and Vibration, Volume II, Complex Flow-Structure Interactions.* 1986.

[6] Borello, Gérard; Nguyen Van Lan, Rémi. *Transfer Path Analysis, Experimental and Virtual SEA on fuselage panel.* InterAC, Technical Engineering & Research in Acousitcs, RT10B145B-Airbus-ESEA-VSEA-V1, 2011.

[7] Bruehl, Stephan. *TL-Tool User Manual (Transmission Loss Calculation from FE Models).* EADS Corporate Research Centre Germany, 2006.

[8] Bull, M.K. *Wall-Pressure Fluctuations beneath Turbulent Boundary Layers: Some Reflections on Forty Years of Research.* Journal of Sound and Vibration, 1996.

[9] Callsen, Sören. *Zum Einsatz der Statistischen Energieanalyse bei Schalldämmmaßberechnungen im Flugzeugbau, PhD Thesis.* Institut für Modellierung und Berechnung, TU Hamburg-Harburg, 2010.

[10] Catlett, M.R.; Forest, J.B.; Anderson, J.M.; Stewart, D.O. *Empirical Spectral Model of Surface Pressure Fluctuations beneath Adverse Pressure Gradients.* AIAA paper 2014–2910, 20th AIAA/CEAS Aeroacoustics Conference, 16-20 June 2014, Atlanta, GA, June.

[11] Chase, D.M. *The character of the turbulent wall pressure spectrum at subconvective wavenumbers and a suggested comprehensive model*, volume 112. Journal of Sound and Vibration, 1987.

[12] Chase, D.M. *Modeling the wavevector-frequency spectrum of turbulent boundary layer wall pressure*, volume 70. Journal of Sound and Vibration, May 1980.

[13] Clauser, F.H. *Turbulent Boundary Layers in Adverse Pressure Gradients*, volume 21. Journal of the Aeronautical Sciences, 1954.

[14] Cockburn, J.A.; Jolly, A.C. *Structural-acoustic response, noise transmission losses and interior noise levels of an aircraft fuselage excited by random pressure fields.* Air Force Flight Dynamics Laboratory, Air Force Systems Command, AFFDL-TR; 68-2. WR, 1968.

[15] Cockburn, J.A.; Robertson J.E. *Vibration response of spacecraft shrouds to in-flight fluctuating pressures.* Journal of Sound and Vibration, 1974.

[16] Corcos, G.M. *Resolution of Pressure in Turbulence.* The Journal of the Acoustical Society of America, 1963.

[17] Corcos, G.M. *The structure of the turbulent pressure field in boundary-layer flows.* Journal of Fluid Mechanics, 1964.

[18] Dannhauer, Axel. Cent - lshx flugversuche. Technical Report IB-224-2016 A119, German Aerospace Center, Institute of Aerodynamics and Flow Technology, 2016.

[19] Efimtsov, B.M. *Similarity criteria for the spectra of wall pressure fluctuations in a turbulent boundary layer.* Soviet Physics - Acoustics, January - February 1984.

[20] Efimtsov, B.M. *Characteristics of the field of turbulent wall pressure fluctuations at large Reynolds numbers.* Soviet Physics - Acoustics, July - August 1982.

[21] Efimtsov, B.M.; Kozlov, N.M.; Kravchenko, S.V.; Andersson, A.O. *Wall Pressure-Fluctuation Spectra at Small Forward-Facing Steps.* AIAA paper 1999–1964, 1999.

[22] Efimtsov, B.M.; Rizzi, S.A.; Andersson, A.O.; Andrianov, E.V. *Influence of Small Steps on Wall Pressure Fluctuation Spectra Measured on TU-144LL Flying Laboratory.* AIAA paper 2002-2605, 2002.

[23] Ehrenfried, Klaus; Koop, Lars. *Experimental study of pressure fluctuations beneath a compressible turbulent boundary layer.* AIAA paper 2008–2800, 2008.

[24] Eisfeld, Bernhard. Implementation and validation of the hellsten k-omega earsm. Technical Report IB-2003/33, German Aerospace Center, Institute of Aerodynamics and Flow Technology, 2003.

[25] Ewert, R. *RPM - the fast Random Particle-Mesh method to realize unsteady turbulent sound sources and velocity fields for CAA applications.* AIAA paper 2007-3506, 2007.

[26] Ewert, R. *Broadband slat noise prediction based on CAA and stochastic sound sources from a fast random particle-mesh (RPM) method*, volume 37. Computers & Fluids, 2008.

[27] Ewert, R; Dierke, J.; Neifeld, A.; Appel, C.; Siefert, M.; Kornow, O. *CAA Broadband Noise Prediction for Aeroacoustic Design*, volume 330. Journal of Sound and Vibration, 2011.

[28] Ewins, D.J. *Modal Testing Theory, Practice and Applications, Second Edition.* Research Studies Press Ltd., 2000.

[29] Fahy, Frank. *SEANET, Statistic Energy Analysis: A Guide for Potential Users.*

[30] Fahy, Frank; Gardonio, Paolo. *Sound and Structural Vibration. Radiation, Transmission and Response.* Academic Press, 2007.

[31] Farabee, T.M.; Casarella, M. J. *Spectral Features of Wall Pressure Fluctuations Beneath Turbulent Boundary Layers*, volume 3. American Institute of Physics, 1991.

[32] Fernholz, H.H.; Finley, P.J. *The incompressible zero-pressure-gradient turbulent boundary layer: An assessment of the data*, volume 32. Progress in Aerospace Sciences, 1996.

[33] Gerhold, T.; Friedrich, O.; Evans, J.; Galle, M. *Calculation of complex three-dimensional configurations employing DLR-TAU-Code.* 35th Aerospace Sciences Meeting & Exhibit, January 1997.

[34] Gloerfelt, X.; Berland, J. *Direct computation of turbulent boundary layer noise.* AIAA paper 2009-3401, May, 11-13 2009.

[35] Gloerfelt, X.; Margnat, F. *Effect of Mach number on boundary layer noise.* AIAA paper 2014–3291, 2014.

[36] Goody, M. *An Experimental Investigation of Pressure Fluctuations in Three-Dimensional Turbulent Boundary Layers.* Ph.D. Dissertation, Dept. of Aerospace and Ocean Engineering, Virginia Polytechnic Inst. and State Univ., Blacksburg, VA, Sept. 1999.

[37] Goody, Michael. *Empirical Spectral Model of Surface Pressure Fluctuations*, volume 42. AIAA Journal, September September 2004.

[38] Graham, W.R. *Evaluation of a model for boundary-layer induced noise in aircraft.* Noise-Con, 1993.

[39] Graham, W.R. *High-frequency vibration and acoustic radiation of fluid-loaded plates.* Philosophical Transactions of The Royal Society A, 1995.

[40] Graham, W.R. *The influence of curvature on the sound radiated by vibrating panels.* Acoustical Society of America, 1995.

[41] Graham, W.R. *Boundary Layer Induced Noise in Aircraft, Part I: The Flat Plate Model.* Journal of Sound and Vibration, 1996.

[42] Graham, W.R. *Boundary Layer Induced Noise in Aircraft, Part II: The Trimmed Flat Plate Model.* Journal of Sound and Vibration, 1996.

[43] Graham, W.R. *A Comparison of Models for the Wavenumber Frequency Spectrum of Turbulent Boundary Layer Pressures.* Journal of Sound and Vibration, 1997.

[44] Hao, Jin; Wang, Meng. *Flow Noise from Swept Steps in Turbulent Boundary Layers.* AIAA paper 2013–2248, 27-29 May 2013.

[45] Haxter, S.; Spehr, C. *Comparison of model predictions for coherence length to in-flight measurements at cruise conditions*, volume 390. Journal of Sound and Vibration, 2016.

[46] Haxter, Stefan; Spehr, Carsten. *Examination of the Influence of Flight Altitude and Speed on the Efimtsov Model Parameters.* AIAA paper 2013–2028, 19th AIAA/CEAS Aeroacoustics Conference May 27-29, 2013, Berlin, Germany.

[47] Haxter, Stefan; Spehr, Carsten. *Listening to Turbulence: Measuring Coherence Decay at Different Positions on an Aircraft at Cruise Flight.* AIAA paper 2014–3064, 20th AIAA/CEAS Aeroacoustics Conference, Atlanta, Georgia, USA, 16. - 20. June 2014.

[48] Haxter, Stefan; Spehr, Carsten. *Two-Dimensional Evaluation of Turbulent Boundary Layer Pressure Fluctuations at Cruise Flight Conditions.* AIAA paper 2012–2139, 18th AIAA/CEAS Aeroacoustics Conference, Colorado Springs, CO, USA, June 04-06, 2012.

[49] Hockney, R.W.; Eastwood, J.W. *Computer simulation using particles.* Taylor & Francis Inc., 1988.

[50] Howe, M.S. *A note on the Kraichnan-Phillips theorem*, volume 234. Journal of Fluid Mechanics, 1992.

[51] Howe, M.S. *Acoustics of Fluid-Structure Interactions.* Cambridge University Press, 2008.

[52] Hu, N.; Appel, C.; Herr, M.; Reiche, N.; Ewert, R.; . *Numerical Study of Wall Pressure Fluctuations for Zero and Non-Zero Pressure Gradient Turbulent Boundary Layers.* AIAA paper 2016-2911, 2016.

[53] Hu, N.; Herr, M. *Characteristics of wall pressure fluctuations for a flat plate turbulent boundary layer with pressure gradients.* AIAA paper 2016-2749, 2016.

[54] Hu, N.; Reiche, N.; Ewert, R. *Simulation of Turbulent Boundary Layer Wall Pressure Fluctuations via Poisson Equation and Synthetic Turbulence.* Journal of Fluid Mechanics, 2016.

[55] Hu, Nan. *Contributions of Different Aeroacoustic Sources to Aircraft Cabin Noise.* AIAA paper 2013–2030, 19th AIAA/CEAS Aeroacoustics Conference, Berlin, Deutschland, May 27-29, 2013.

[56] Hwang, Y.F. *Comparison of semi-empirical models for turbulent boundary layer wall pressure spectra.* Journal of Sound and Vibration, 2009.

[57] Klabes, A.; Appel, C.; Herr, M.; Bouhaj, M. *Fuselage Excitation During Cruise Flight Conditions: Measurement and Prediction of Pressure Point Spectra.* AIAA paper 2015–3115, June 2015.

[58] Klabes, A.; Appel, C.; Herr, M.; Callsen, S. *Fuselage Excitation During Cruise Flight Conditions: A New CFD Based Pressure Point Spectra Model.* Inter-Noise (Paper 140), 2016.

[59] Klabes, A.; Appel, C.; Herr, M.; Callsen, S. *Fuselage excitation during cruise flight conditions: CFD based prediction of pressure point spectra; Aeroacoustics research in Europe: The CEAS-ASC report on 2015 highlights.* Number 381. Journal of Sound and Vibration, 2016.

[60] Klabes, Alexander. *Validation of a simulation model for the "Statistic Energy Analysis" (SEA) of the Airbus A320 for different flight parameters.* Airbus Operations GmbH & German Aerospace Center (DLR), 2012.

[61] Kraichnan, R.H. *Pressure Fluctuations in Turbulent Flow over a Flat Plate*, volume 28. The Journal of the Acoustical Society of America, May 1956.

[62] Leatham, M.; Stokes, S.; Shaw, J.A.; Cooper, J.; Appa, J.; Blaylock, T.A. *Automatic Mesh Generation for Rapid-Response Navier-Srokes Calculations.* FLUIDS 2000 Conference and Exhibit, AIAA 2000-2247, June 2000.

[63] Lowson, M.V. *Prediction of Boundary Layer Pressure Fluctuations.* U.S. Air Force Flight Dynamics Laboratory Technical Report AFFDL-TR 67-167s, April 1968.

[64] Medeiros, A.A.; Alimonti, L.; Gardner, B.; Callsen, S.; Klabes, A. *An SEA Modeling of General Surface Pressure Excitation Based on their Wavenumber-frequency Spectrum.* Inter-Noise (Paper 1013), 2016.

[65] Miller, Teresa S. *Turbulent Boundary Layer Models for Acoustic Analysis, Doctoral Thesis.* Department of Aerospace Engineering and the faculty of Graduate School of Wichita State University, 2011.

[66] Miller, T.S.; Gallman, J.M.; Moeller, M.J. *Review of Turbulent Boundary Layer Models for Acoustic Analysis.* AIAA paper 2011–1083, 49th AIAA Aerospace Sciences Meeting including the New Horizons Forum and Aerospace Exposition 4 - 7 January 2011, Orlando, Florida.

[67] Palumbo, Dan. *Determining correlation and coherence lengths in turbulent boundary layer flight data.* NASA Langley Research Center, 24 April 2012.

[68] Palumbo, Dan. *Measurement of the Correlation and Coherence Lengths in Boundary Layer Flight Data*, volume TM-2011-217060. NASA Langley Research Center, February 2011.

[69] Pope, Stephen B. *Turbulent Flows.* Cambridge University Press, 2000 (13th printing 2015).

[70] Rackl, Robert; Weston, Adam. *Modeling of Turbulent Boundary Layer Surface Pressure Fluctuation Auto and Cross Spectra-Verification and Adjustments Based on TU-144LL Data.* NASA/CR-2005-213938, The Boeing Company, 2005.

[71] Robertson, J.E. *Prediction of In-flight Fluctuating Pressure Environments Including Protuberance Induced Flow.* NASA, CR-119947, March 1971.

[72] Rotta, Julius C. *Ueber die Theorie der turbulente Grenzschichten.* Max-Planck-Institut fuer Stroemungsforschung, 1950.

[73] Rozenberg, Yannick; Robert, Gilles; Moreau, Stephane. *Wall-Pressure Spectral Model Including the Adverse Pressure Gradient Effects.* AIAA Journal, 2012.

[74] Schewe, G. *On the structure and resolution of wall-pressure fluctuations associated with turbulent boundary-layer flow*, volume 134. Journal of Fluid Mechanics, 1983.

[75] Hermann Schlichting. *Grenzschicht-Theorie*, volume 5. Verlag G. Braun, Karlsruhe, 1964.

[76] Schwamborn, D.; Gerhold, T.; Heinrich, R. *The DLR TAU-Code: Recent Applications in Research and Industry.* ECCOMAS CFD 2006 Conference, August 2006.

[77] Smol'yakov, A.V. *Calculation of the Spectra of Pseudosound Wall-Pressure Fluctuations in Turbulent Boundary Layers*, volume 46. Acoustical Physics, 2000.

[78] Smol'yakov, A.V. *A New Model for the Cross Spectrum and Wavenumber Frequency Spectrum of Turbulent Pressure Fluctuations in a Boundary Layer*, volume 52. Acoustical Physics, 2006.

[79] Smol'yakov, A.V.; Tkachenko, V.M. *Model of a field of pseudosonic turbulent wall pressures and experimental data*, volume 37. Akusticheski Zhurnal, 1991.

[80] Spalart, P.R. *Direct Simulation of a Turbulent Boundary Layer up to R=1410.* NASA Technical Memorandum 89407, 1986.

[81] Speaker, W.V.; Ailman, C.M. *Spectra and Space- Time Correlation of the Fluctuating Pressures at a Wall Beneath a Supersonic Turbulent Boundary Layer Pertubed by Steps and Shock Waves.* NASA CR 486, 1966.

[82] Spehr, Carsten; Hennings, Holger; Buchholz, Heino; Bouhaj, Mohamed; Haxter, Stefan; Hebler, Anne. *In-flight Sound Measurements: A First Overview.* AIAA paper 2012–2208, 18th AIAA/CEAS Aeroacoustics Conference, Colorado Springs, CO, USA, June 04-06, 2012.

[83] Ames Research Staff. *Equations, Tables, and Charts for Compressible Flow.* NASA, NACA Report 1135, Moffett Field, California, 1954.

[84] Suryadi, Alexandre; Herr, Michaela. *Wall pressure spectra on a DU96-W-180 profile from low to pre-stall angles of attack.* AIAA paper 2015-2688, 2015.

[85] Teschner, Mark. *Validierung eines vibroakustischen Berechnungsmodells fuer einen Flugzeugrumpf in unterschiedlichen Flugzustaenden.* Airbus Operations GmbH & Hamburg University of Applied Sciences, 2013.

[86] Tkachenko, V.M.; Smol'yakov, A.V. *Wave Number-Frequency Spectrum of Turbulent Pressure Fluctuations: Methods of Measurement and Results.* Akusticheski Zhurnal, 2008, Vol. 54, No. 1.

[87] Togiti, Vamshi; Eisfeld, Bernhard. *Assessment of g-Equation Formulation for a Second-Moment Reynolds Stress Turbulence Model.* AIAA paper 2015–2925, June June 2015.